Aspects of power reduction in the chlor-alkali membrane electrolysis

Please check the document version of this publication:

• A submitted manuscript is the version of the article upon submission and before peer-review. There can be important differences between the submitted version and the official published version of record. People interested in the research are advised to contact the author for the final version of the publication, or visit the DOI to the publisher's website.
• The final author version and the galley proof are versions of the publication after peer review.
• The final published version features the final layout of the paper including the volume, issue and page numbers.

[Link to publication](#)

ASPECTS OF POWER REDUCTION
IN THE
CHLOR-ALKALI MEMBRANE ELECTROLYSIS

J. M. CHIN KWIE JOE

ASPECTS OF POWER REDUCTION
IN THE
CHLOR-ALKALI MEMBRANE ELECTROLYSIS

PROEFSCHRIFT

TER VERKRIJGING VAN DE GRAAD VAN DOCTOR
AAN DE TECHNISCHE UNIVERSITEIT EINDHOVEN,
OP GEZAG VAN DE RECTOR MAGNIFICUS,
PROF. IR. M. TELS, VOOR EEN COMMISSIE
AANGEWEZEN DOOR HET COLLEGE VAN
DEKANEN IN HET OPENBAAR TE VERDEDIGEN
OP VRIJDAG 27 OKTOBER 1989 TE 14.00 UUR

DOOR

DRS. JOEK MIEN CHIN KWIE JOE

GEBOREN TE PARAMARIBO

Dit proefschrift is goedgekeurd door

de promotoren: **PROF. E. BARENDRECHT**

en

PROF. DR. A. K. CHESTERS

Aan Petra en de kinderen

Contents   1

Chapter 1

Introduction

1.1 Scope of this study

The main purpose of this study is to investigate the electrochemical and design factors, governing the power consumption for the industrial chlor-alkali membrane cell electrolysis. To achieve this goal, the impact of various parameters on the cell voltage have been investigated.

A fundamental understanding of this should finally result in a substantial reduction of the cell voltage, and so in production costs.

In general, the presence of gas bubbles in both electrolytes and at both electrodes and the membrane surface increases the cell voltage. Therefore, means to minimize gas bubbles effects on the cell voltage have been given special attention.

Cell voltage and bubble characteristics are affected by the following parameters:

- electrode material and its surface morphology;
- concentration, pH and possible contamination of the sodium chloride and sodium hydroxide solutions;
- membrane properties (finite and zero gap membrane);
- current density;
- gas void fraction;
- operating temperature, pressure and electrolyte velocity along the electrode surface;
- electrode and cell configuration, distance between electrode and membrane.

The bubble characteristics are determined by means of high speed motion pictures and the gas void fraction is determined by a new technique in a semi-industrial cell (50 cm high). A novel technique is developed to measure the membrane resistance.

Substantial efforts are spent to determine the optimum configuration of both electrodes and the properties of various available and commercially applied membranes. Knowledge concerning the relation between the cell voltage and the different process parameters is necessary to predict the best settings of these process parameters, required to minimize the energy consumption at a given chlorine production.

Also, in this investigation a number of tests is performed under semi-industrial conditions.

1.2 Outline of this dissertation

In chapter 2, the history and some background information are presented, including a pertinent literature review.

Chapter 3 presents experimental results on the effects of current density and solution flow velocity on the attached-bubble parameters for a chlorine-evolving vertical transparent platinum electrode. In this and subsequent chapters, the results we discussed at the close of the chapter.

Chapter 4 describes a technique for measuring the supersaturation of dissolved gas in the solution at the electrode surface and the results obtained using wire-electrodes.

Chapter 5 presents the effects of current density, solution flow velocity and temperature on the detached-bubble parameters for a gas-evolving wire electrode.

Chapter 6 describes the behaviour of the gas void fraction and the ohmic resistance in an electrolysis cell under different operating conditions.

Chapter 7 describes the properties of the different types of membranes and the developed resistance measuring technique.

Chapter 8 shows the dependence of the cell voltage of the electrolysis parameters.

In Chapter 9, the effects of different electrode configurations on cell voltage are discussed.

Chapter 10 gives the conclusions, important for cost saving. Finally, some suggestions for further research are made.

Chapter 2

Some historical and recent background information

2.1 Introduction

In 1800 Cruikshank observed the evolution of chlorine by passing an
electric current through a solution of sodium chloride. The first
commercially successful electrolysis plant was built in 1890 [1].
The electrolysis of sodium chloride solution, or brine, prepared directly
from natural salt deposits to yield chlorine, caustic soda and hydrogen,
is now a major electrochemical industry.
In the USA, the annual production of chlorine in the eighties is
approximately 10^7 tons, while in The Netherlands it amounts to about 3 x
10^5 tons [2].
During the last twenty-eight years marked progress has been made in the
chlor-alkali process, resulting from scientific innovation and economic
and social pressures for energy conservation, pollution control and
higher safety standards.

2.2 The effects of gas bubbles on the electrolytic process

Evolved gas bubbles between two flat-plate electrodes affect an
electrochemical process in both a negative and a positive way.
The negative effects are:
● gas bubbles increase the resistance of the electrolyte [3-7];
● gas bubbles attached to the electrode surface force the current
   through smaller areas of the electrode; consequently, the current
   density increases and so the activation overpotential of the reaction;
● gas bubbles attached to the membrane surface block current passage.
The positive effect is:
● rising gas bubbles disturb the electrolyte layer close to the
   electrode and thereby enhance mass transfer of any diffusion
   controlled species to the electrode surface; hence, mass transfer
   overpotential decreases.

The performance of an electrolysis cell can be expressed in many ways.
The most commonly used quantities for cell performance are [8]:

- the current efficiency, η_i, is defined by:

$$\eta_i = \frac{w'}{w} \times 100\%$$

where w = the amount of product formed according to Faraday's law, and w' = the amount of product actually obtained;

- the energy consumption is normally quoted in kilowatt hours per kilogram product ($kWh\ kg^{-1}$) and is given by the equation:

$$energy\ consumption = \frac{nFU}{3.6\ 10^4 \eta_i M}$$

where U = the operating cell voltage and M = the molecular weight in kilograms per kmol;

- the energy efficiency is given by:

$$energy\ efficiency = \frac{W_r}{W} \times 100\%$$

$$= \frac{U_r}{U} \times \eta_i\%$$

where W_r = the electric energy for unit amount production based on thermodynamics, W = the actual electric energy for unit amount production; U_r = the reversible cell voltage and U = the cell voltage.

2.3 The chlor-alkali processes

At present, three types of chlor-alkali electrolysis processes exist: the mercury, diaphragm and membrane process. The main anode reaction is the same for all three types:

$$2Cl^- \rightarrow Cl_2 + 2e^- \quad (E^\circ = +1.36\ V) \tag{2.1}$$
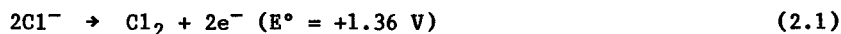
The main cathode reaction for both diaphragm and membrane cells is:

$$2H_2O + 2e^- \rightarrow H_2 + 2\ OH^- \quad (E^\circ = -0.84\ V) \tag{2.2}$$
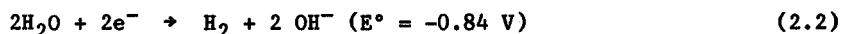
For the mercury cell the cathode reaction is:

$$Na^+ + e^- + Hg \rightarrow NaHg \quad (E° = -1.89 \text{ V}) \tag{2.3}$$
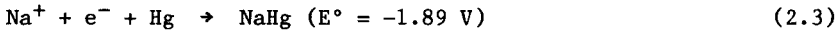
The sodium amalgam is decomposed in a separate reactor to give sodium hydroxide and hydrogen:

$$2NaHg + 2H_2O \rightarrow 2Hg + 2Na^+ + 2 OH^- + H_2 \tag{2.4}$$
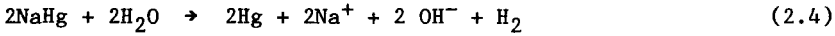
The net reaction is for all three processes the same:

$$2NaCl + 2H_2O \rightarrow Cl_2 + 2NaOH + H_2 \tag{2.5}$$
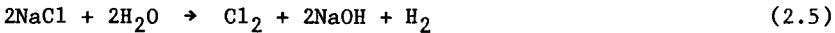
The reversible cell voltage, U_r, the theoretical minimum voltage which is required for reaction (2.5) is determined by the Gibbs' free enthalpy change, ΔG [9]:

$$U_r = \frac{-\Delta G}{nF} \tag{2.6}$$

where n = the number of electrons transferred in the reaction and F = the Faraday constant.

The relation between the Gibbs' free enthalpy change and the enthalpy and entropy change for a reaction at constant temperature and pressure is given by:

$$\Delta G = \Delta H - T\Delta S \tag{2.7}$$

where ΔH = the enthalpy change of this reaction, ΔS = the entropy change and T = temperature.

The reversible cell voltage, U_r, can be reduced by increasing the cell temperature, because ΔS is positive for the chlor-alkali process (cf. Eqs. 2.5, 2.6 and 2.7). For cell operation, the actual cell voltage, U, has to exceed U_r, to overcome the overpotentials at the electrodes and the ohmic resistance in the cell. The total actual cell voltage is therefore given by [2,9]:

$$U = E_{eq}^C - E_{eq}^A - |\eta_D^C| - |\eta_D^A| - |\eta_r^C| - |\eta_r^A| - |\eta_d^C| - |\eta_d^A| - IR_c \tag{2.8}$$

E_{eq}^{C} and E_{eq}^{A} are the equilibrium potentials for the cathode and anode reactions, respectively, so that $(E_{eq}^{C} - E_{eq}^{A}) = U_r$ can be calculated from the Gibbs' free enthalpy change for the overall reaction by Eq. 2.6.

The overpotential, η, is defined as the deviation of electrode potential, E, from the electrode equilibrium potential, E_{eq}, i.e.:

$$\eta = E - E_{eq} \qquad\qquad (2.9)$$

η_D^C and η_D^A are the cathode and anode charge transfer overpotentials, respectively. η_r^C and η_r^A are the overpotentials associated with chemical reactions at the cathode and anode, respectively. The sum of the overpotentials of η_D^C, η_D^A, η_r^C and η_r^A is often called the activation overpotentials and is denoted as η_a; η_d^C, η_d^A are the cathode and anode mass transfer overpotentials, respectively.

In electrolytic processes the overpotentials and the IR_c term represent energy losses and, hence, will make the operating cell voltage more negative.

For a simple electron transfer reaction, the total overpotential, η, determines, according to the Butler-Volmer equation [9], the current denstity, i:

$$i = i_o \ [\exp \ (1-\alpha) \ nF\eta/RT - \exp - \alpha nF\eta/RT] \qquad\qquad (2.10)$$

where i_o = the exchange current density and α = the charge transfer coefficient. So, the major factors, determining the magnitude of the overpotential, are the current density and the exchange current density, i.e. the kinetics and catalysis of the electrode process. The exchange current density depends on the electrolysis conditions such as composition of the electrolyte, its pH and temperature, electrode configuration, morphology of the electrode surface, and particularly the electrode material. The electrode material must only catalyse the reaction of interest; for example, the anode in the chlor-alkali cell must catalyse chlorine but not oxygen evolution. The mass transfer overpotential, η_d, is caused by diffusion of electro-active species to the electrode surface: η_d can be reduced, according to Fick's first law, by applying a more concentrated electrolyte, a higher temperature and

forced solution flow. The ohmic potential drop, IR_c, is the product of cell current, I, and the electrical cell resistance, R_c. This R_c is the sum of the electrical resistance of the bubble–electrolyte mixture, the separator (membrane or diaphragm), the current feeders and the electric circuit resistances.

The cell resistance, R_c, can be decreased, for example, by making the interelectrode gap smaller and using more concentrated electrolyte. The resistance of the bubble–electrolyte mixture is higher than the resistance of the pure electrolyte.

So, the gas void fraction and its distribution in a flat–plate electrodes cell must have a great impact on the cell resistance [3-7].

In general, the membranes will cause a substantial increase in cell resistance, although they are essential for product purity and safety reasons. At present, most of the chlor–alkali cell anodes have been replaced by dimensionally stable anodes (DSA). These materials are titanium–based with a coating of ruthenium dioxide and/or other transition metal oxides, e.g. Co_3O_4. They show excellent catalytic activity so that the chlorine overpotential is as low as 70 mV [13] at $i = 4$ kAm.$^{-2}$. Compare the graphite anode overpotential under the same conditions: about 500 mV [2]. This change alone has reduced the energy requirement significantly. However, DSA electrodes need to be applied under carefully controlled conditions. For example, decreasing the temperature, or carrying out the electrolysis with sulphate ions in solution can lead to oxygen contamination of the chlorine.

The cathode in diaphragm and membrane cells is made of steel with a hydrogen overpotential of about 400 mV, at $i = 4$ kAm^{-2}. Activated cathodes, with coatings of nickel alloys or transition metal oxides, are now available, decreasing this overpotential to 150-200 mV [10]. At this low hydrogen overpotential, however, traces of iron of the cathode housing dissolve out can thereafter also precipitate onto the cathode and so plug the perforated plate cathode, resulting in cell voltage increase. To eliminate this problem, mild steel construction had to be replaced by a more corrosion resistant material. The geometric structure of electrodes, at which gas is evolved, is very important. The design of electrodes must permit rapid bubble release to minimize the gas bubble effect and so to reduce the overpotential. Hence, it is common to apply expanded metal, perforated plate, lamellar with rounded flat profile,

plate with louvres, electrodes, consisting of fine wires and spacing from each other [11], electrodes with vertical oblong opening [12], etc., to release gas in the desired direction.

The caustic soda produced in a diaphragm cell is always contaminated with chloride ion, because the diaphragm is porous and cannot discriminate between ions. Diffusion occurs because of concentration differences.

In a cation-selective membrane cell, however, a catholyte with about 22 weight % NaOH and a minimum amount of impurities can be obtained. The many improvements, introduced in the chlor-alkali process, have reduced the energy consumption drastically. A further decrease remains desirable. This can be accomplished by improvement of the shape of and the materials used for both electrodes, and the membrane qualities.

2.4 References

1   C.L. Mantell, Electrochemical Engineering, McGraw-Hill Book Company, New York (1960)

2   D. Pletcher, Industrial Electrochemistry, Chapman and Hall, New York (1981)

3   C.W. Tobias, J. Electrochem. Soc. 106 (1959) 833

4   L. Segrist, O. Dossenbach and N. Ibl., J. Appl. Electrochem. 10 (1980) 223

5   F. Hine and K. Murakami, J. Electrochem. Soc. 127 (1980) 292

6   G. Kreysa and H.J. Külps, J. Electrochem. Soc. 128 (1981) 979

7   L.J.J. Janssen, J.J.M. Geraets, E. Barendrecht and S.J.D. van Stralen, Electrochim. Acta. 27 (1982) 1207

8   F. Hine, Electrode Processes and Electrochemical Engineering Plenum Press, New York (1985)

9   C.H. Hamann/W. Vielstich, Elektrochemie II, Elektroden-prozesse, Angewandte Elektrochemie, Verslag Chemie, Physik. Verslag, Bonn (1980)

10 M. Seko, A. Yomiyama, S. Ogawa, H. One, Development of Asahi Chemical Chlor-Alkali Technology, Society of Chemical Industry, Electrochemistry Technology Group, International Chlorine Symposium, London, 2-4.6. (1982) 24

11 E.L. Littauer, Method for reducing (pseudo-) ohmic overpotential at gas-evolving electrodes, United States Patent, 3, 880, 721, 1975

12 U. Giacopelli, Electrode für Erzeugung eines Gases in einer Zelle mit einer Membran, Deutsches Patentamt, Offenlegungsschrift 2709093, 1977

13 G. Faita and G. Fiori, J. Applied Electrochem. $\underline{2}$ (1972) 31

Chapter 3

Attached-bubble behaviour for a chlorine-evolving
transparent platinum electrode

3.1 Introduction

Many electrochemical processes produce gas bubbles during electrolysis. It is well known that bubbles evolved between two flat plate electrodes significantly increase the energy comsumption of the process (cf. Chapter 2, Section 2.2); this fact is especially important for industrial processes. In the last 25 years, bubble behaviour and the effect of bubbles on the ohmic resistance in the electrolytic cell have been intensively studied: see the survey of Vogt [1] on gas-evolving electrochemical processes.

The behaviour of attached oxygen and hydrogen bubbles on relatively small transparent nickel electrodes in KOH solution was thoroughly investigated [2-4]. Similar experiments were performed by Bongenaar [5] with a large, "transparent" gold electrode (50×2 cm^2). So far, no literature data for chlorine bubbles attached to transparent electrodes are available. In this chapter, a short literature review concerning nucleation, growth, departure and rise of gas bubbles is presented in Section 3.2.

In Section 3.3, the experimental set-up of the determination of attached-bubble parameters is described.

The results obtained are presented in Section 3.4. The relevant results are discussed and explained in Section 3.5.

3.2 Literature review

3.2.1 Nucleation and growth

At the start of the electrolysis process, ions are discharged and form adsorbed atoms or molecules at the electrode. Desorbing molecules then dissolve and diffuse into the bulk solution. Both the limited rate of diffusion and the low solubility of the dissolved gas in the electrolyte cause the solution near the electrode to become supersaturated, so that nucleation of gas bubbles can take place on the electrode surface. In a situation in which there is no convection and no gas bubble

formation, the supersaturation concentration Δc_x, at a distance x perpendicular to the electrode surface, and Δc^{σ}, at the electrode surface (x = 0), can be expressed as a function of time, t_1, after starting the electrolysis process, by [6]:

$$\Delta c_x = \frac{i}{nF(\pi D)^{1/2}} \int_0^{t_1} (t)^{-1/2} \exp.(- \frac{x^2}{4Dt})dt \qquad (3.1)$$

and

$$\Delta c^{\sigma} = \frac{2i}{nF(\pi D)^{1/2}} (t_1)^{1/2} \qquad (3.2)$$

When convection occurs due to concentration gradients or temperature differences, dissolved gas will be transported to the bulk solution by mass diffusion and convection; the average supersaturation concentration at the electrode will then become constant. The solution at a gas-evolving electrode is vigorously stirred by growing, detaching, coalescing and rising bubbles. The gaseous product at the gas-evolving electrode is only partly present as bubbles. This fraction is called the efficiency of gas bubble formation.

Cavities at an electrode surface can generate gas bubbles in a analogous way to that at a superheated wall [7, 8].

A relation between the supersaturation concentration of dissolved gas at the electrode surface, $\Delta c^{\sigma} = c_g^{\sigma} - c_g^s$, and the average active cavity mouth radius has been derived:

$$R_c = 2\sigma/K.\Delta c^{\sigma} = 2\sigma/\Delta P \qquad (3.3)$$

where R_c = average active cavity mouth radius, σ = the surface tension, K = Henry's constant, Δc^{σ} = the supersaturation concentration of dissolved gas at the electrode surface, ΔP = the equilibrium gas pressure in a cavity corresponding to the degree of supersaturation at the wall, c_g^{σ} = the concentration of dissolved gas at the electrode-solution interface and c_g^s = the saturation concentration of dissolved gas in the bulk solution, at atmospheric pressure.

Although (3.3) applies to bubbles formed on horizontal surfaces, a comparable relation may be expected to apply to vertical surfaces - as proposed by Sloten (Eq. 3.10).

It should be emphasized that supersaturation concentration of dissolved

gas at the electrode surface, Δc^{σ}, should not be confused with the significantly lower supersaturation in the vicinity of gas bubbles attached to the electrode, the first one predominantly controlling nucleation and the latter one controlling bubble growth and so coverage [1].

Eq. (3.3) shows that Δc^{σ} determines if a cavity is active or not, at low Δc^{σ} only the large cavities are active, while at high Δc^{σ} also the small cavities are active.

The density of active sites on the electrode surface equals its bubble population density. Sillen et al. [9] determined the effect of current density, solution flow velocity, temperature and pressure on the average bubble population density, d, both for an oxygen -and a hydrogen-evolving vertical transparent nickel electrode in 1 M KOH at 303 K, and 101 kPa, in both free and forced convection. They found that the bubble population density increases with increasing current density, decreases with increasing solution flow velocity and temperature, and increases with increasing gas pressure [2, 9, 10]. Additionally, it also depends on the nature of gas evolved, the surface texture of the electrode, the electrolyte composition and on the position and geometry of the electrode. The bubble population density fluctuates around a quasi-stationary average value. The amplitude and the time scale of these fluctuations depend on electrolytic conditions [2]. The generated gas bubble at the electrode will grow, due to the supersaturation near the electrode surface. Electrolytical bubble growth (mass transfer) is comparable with bubble growth in boiling liquids (heat transfer).

Scriven [22] derived a theoretical equation for asymptotic spherical bubble growth in an uniformly superheated infinite liquid medium by applying force, heat and mass balance at convectionless conditions. For an isothermal bubble growth and by neglecting surface tension, viscosity and long time effects, only the diffusion equation is required. The bubble growth is now limited by the diffusion rate of the dissolved gas through the liquid phase. Solving the diffusion equation, the attached-bubble radius, R_a, is obtained as function of time:

$$R_a = 2\beta(D_g t)^{1/2} \tag{3.4}$$

where D_g = the diffusion coefficient of the dissolved gas, t = the time and β = a growth parameter, which is a function of the Jakob number:

$$Ja = (\bar{c}_g - c_g{}^s)/\rho_g \qquad\qquad (3.5)$$

with $\bar{c}_g$ = the average concentration of dissolved gas in the vicinity of the gas bubble adhering to the electrode, and ρ_g = the gas density. The relation between β and Ja can be approximated by [11, 12]:

$$\beta = Ja \; [1 + (1 + \frac{2 \, \pi}{Ja})^{1/2}]/(2\pi)^{1/2} \qquad\qquad (3.6)$$

From single bubble growth experiments in free convection follows that almost no hydrodynamic convection occurs. It has been found that $R_a{}^2$ increases linearly with growth time, t [2, 8, 11, 13]. The slope of the $R_a{}^2$ versus t graph depends on the type of nucleus [11], thus each nucleus has its own value of β.

From the multiple bubble growth experiments at both free and forced convection it has been found that especially in the first part of the growth stage $R_a{}^2$ increases linearly with time. If the bubble has reached a certain critical size, fluctuations in the growth pattern, due to interference and coalescence with neighbouring bubbles, occur. In spite of these fluctuations the experimental $R_a{}^2$ versus t relation remains linear. The bubbles present on a gas-evolving electrode are in different stages of growth. The initial radius of a bubble is given by relation (3.3). The maximum radius of a bubble present on a gas-evolving electrode depends on many factors, such as the number of active sites, the morphology of the electrode surface, the flow conditions at the electrode surface and the maximum bubble radius in a convectionless solution.

3.2.2 Departure and rise

Up to now, theoretical studies on bubbles concern the departure mechanism of a single bubble growing on a horizontal wall in a convectionless liquid solution [14-16].
Chesters [16] derived the departure radius for two modes of bubbles formed slowly on a round, sharp-edged, horizontal orifice under isothermal conditions.
His derivation is based on the "equilibrium bubble shape theory".
During the growth of a bubble at a very smooth surface, the contact angle, ϕ, at first decreases and then, if the natural contact angle, ϕ_o,

between the bubble and the wall is not reached, increases again (cf. Fig. 3.1, cavity bubble).
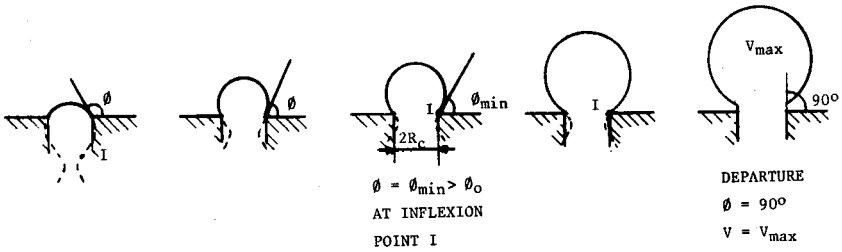
Fig. 3.1 Schematic presentation of the growth of a cavity bubble, $R_f = R_c$.
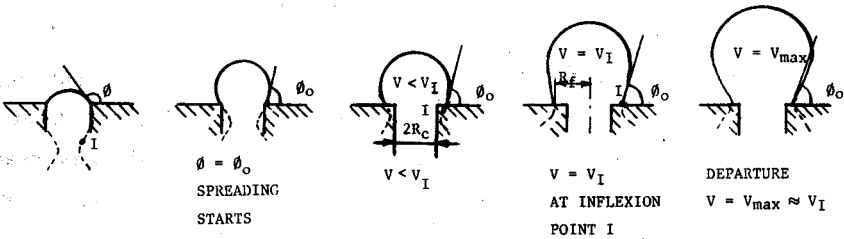
Fig. 3.2 Schematic presentation of the growth of a spreading bubble, $R_f > R_c$.

In case ϕ reaches the value ϕ_o, further growth occurs by spreading of the bubble beyond the orifice (cf. Fig. 3.2, spreading bubble).

When the growth occurs according to the cavity bubble mode (index α), the bubble foot radius, R_f, equals the cavity mouth radius, R_c, during the entire growth period (cf. Fig. 3.1) and the detached-bubble radius is given by:

$$R_{d.\alpha} = [3\sigma R_c/2g(\rho_1-\rho_g)]^{\frac{1}{3}} \qquad\qquad (3.7)$$

For the spreading bubble mode (index β), $R_f > R_c$ (cf. Fig. 3.2) and the detached-bubble radius is:

$$R_{d,\beta} = 0.0107 \, \phi_o \, [\sigma/g(\rho_1-\rho_g)]^{\frac{1}{2}} \qquad\qquad (3.8)$$

where ρ_1 = the liquid density, ρ_g = the gas (vapor) density and g = the gravitational acceleration.

Eq. (3.8) is valid for a bubble with freely moving bubble foot, and a

contact angle limited to 30°. This equation was first presented by Fritz [17]. His derivation was based on the force balance equation, which included buoyancy, adhesion due to surface tension, and an upward directed correction force acting on the bubble at departure [17].

For the derivation of the departure radius, R_d, in case of a fast growing bubble, also forces such as: liquid intertia, surface tension, viscosity and modified buoyancy force have to be considered [18, 19].

The effect of subatmospheric pressure on the departure radius, R_d, has been expressed by Cole and Shulman [15]:

$$R_d = c\phi_o/p \ [\sigma/g(\rho_1-\rho_g)]^{\frac{1}{2}} \qquad (3.9)$$

where c = a pressure-dependent constant and p = the subatmospheric pressure.

Slooten [14] developed an equation for the maximal bubble departure volume, V_{dmax}, for a bubble growing on a vertical wall with its foot attached to the mouth of the cavity, a "cavity bubble".

He assumed, among other things, that during the attachment of the bubble on the wall the upward buoyancy force equals the downwards component of the adhesion force, and obtained:

$$V_{d,max} = 4R_c\sigma/\rho_1g \qquad (3.10)$$

The radius of bubbles detached from a gas-evolving electrode varies in a wide range, due to fluctuation in the solution flow induced by departure, rise and coalescence of bubbles and to differences in the size and shape of cavities [20].

The natural rising velocity of the departing single bubble according to Stokes is :

$$v_b = 2R_d^2 \ \rho_1g/9\eta \ \text{or} \qquad (3.11)$$

$$Re = 2R_d^2v_b\rho_1/\eta = 4R_d^3\rho_1^2g/9\eta^2$$

where v_b = the rising velocity of the departing single bubble, η = the viscosity of the solution and Re = the bubble Reynolds number. Eq. 3.11 is valid if:

● the bubble surfaces are immobile (due to surface active contamination

in the system);

- Re < 1.

The detached-bubble radius, R_d, for water at Re = 1 can be calculated
with the equation $R_d = (9\eta^2/4\rho_1 g)^{1/3}$ is 61 μm. This means that Eq. 3.11
is mainly valid for very small bubbles. The velocity of a single bubble
increases with increasing rate of forced solution flow. Moreover, the
velocity of a bubble in a bubble swarm is lower in comparison to the
velocity of a bubble in a solution without bubbles.
The ratio of the average bubble velocity to the average electrolyte
velocity is called the slip ratio. The slip ratio depends on many factors
and is, in general, unknown.
Funk and Thorpe [21] determined experimentally the slip ratio for oxygen
and hydrogen gas bubbles. The slip ratio for both gases was found to be
nearly one.

3.2.3 Parameters characterizing the behaviour of attached-bubbles

In order to characterize the bubble behaviour, the following bubble
parameters have been formulated to describe observations at a
gas-evolving electrode with N_i attached-bubbles at a geometric surface
area of A_i (i: frame number):

d_i bubble population density for frame i; $d_i = N_i/A_i$, average
density of bubble population for n frames;

$$d = \sum_{i=1}^{n} d_i/n \qquad\qquad (3.12)$$

$R_{a,i}$ average radius of attached-bubbles for frame i: the radius of
an adhered bubble j on frame i is denoted by $R_{i,j}$; $R_{a,i} =$

$$\sum_{j=1}^{N_i} R_{i,j}/N_i \qquad\qquad (3.13)$$

R_a average radius of attached-bubbles for n frames;

$$R_a = \sum_{i=1}^{n} R_{a,i}/n \qquad\qquad (3.14)$$

$R_{m,i}$ radius of the biggest attached-bubble on frame i;

R_s average Sauter radius of attached–bubbles for n frames;

$$R_s = \frac{\sum_{i=1}^{n} R_{a,i}^3 /n}{\sum_{i=1}^{n} R_{a,i}^2 /n} \qquad (3.15)$$

s_i degree of screening of the electrode by attached–bubbles for frame i; i.e. the fraction of the electrode surface, covered by the projection of the bubbles;

$$s_i = \sum_{j=1}^{N_i} \pi R_{i,j}^2 /A_i \qquad (3.16)$$

s average degree of screening of the electrode by attached–bubbles;

$$s = \sum_{i=1}^{n} s_i /n \qquad (3.17)$$

$s_i(x)$ degree of screening of the electrode at a distance x from the electrode by attached–bubbles for frame i at $0 < x < 2R_{m,i}$, i.e. the fraction of the electrode surface, covered by the projection at a distance x from the electrode by attached–bubbles;

$$s_i(x) = \sum_{j=1}^{N_i} A_{i,j}(x)/A_i \qquad (3.18)$$

where

$A_{i,j}(x) = \pi(2R_{i,j} x - x^2) = $ the cross–section of the attached–

bubble diameter of bubble j in frame i at a distance x from the electrode surface, cf. Fig. 3.3; since the bubbles are almost
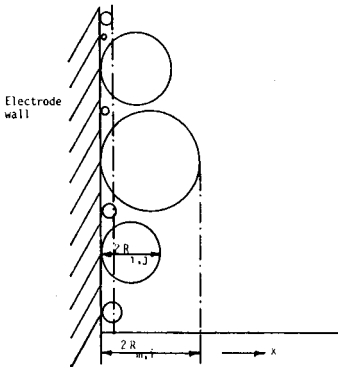
Fig. 3.3 Attached-bubbles at the electrode surface.

completely spherical, it can be assumed that $s_i(0) = 0$ and $s_i(2R_{m,i}) = 0$.

$s(x)$ average degree of screening of the electrode at a distance x from the electrode by attached-bubbles in a frame;

$$s(x) = \sum_{j=1}^{n} s_i(x)/n \qquad (3.19)$$

$V_{a,i}$ volume of attached spherical bubbles per unit area in frame i;

$$V_{a,i} = \sum_{j=1}^{N_i} \frac{4}{3} \pi R_{i,j}^3 / A_i \qquad (3.20)$$

V_a average volume of attached-bubbles per unit area;

$$V_a = \sum_{i=1}^{n} V_{a,i} /n \qquad (3.21)$$

3.3 Experimental

3.3.1 Determination of attached-bubble parameters

The experimental set-up for measurement of bubble parameters is sketched schematically in Fig. 3.4 and Fig. 3.5.
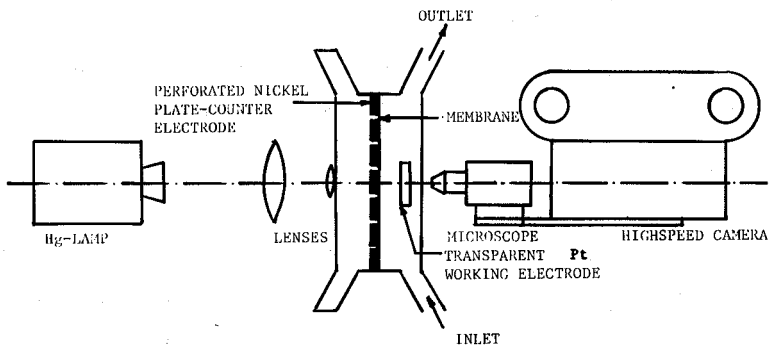
Fig. 3.4   *Schematical set-up for measurement of bubble parameters.*
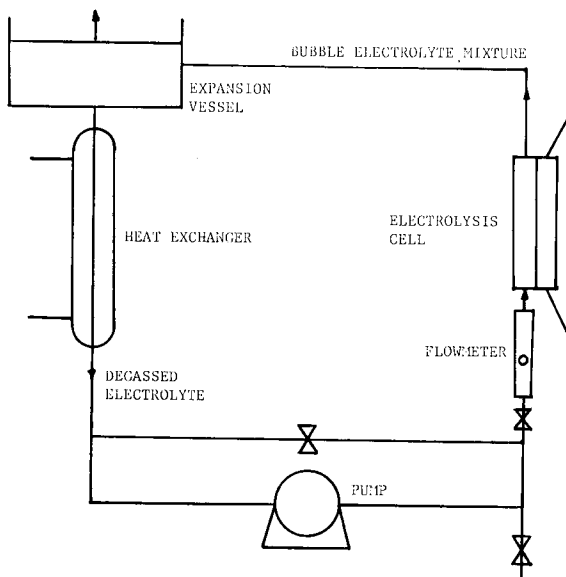
Fig. 3.5 Flow circuit.
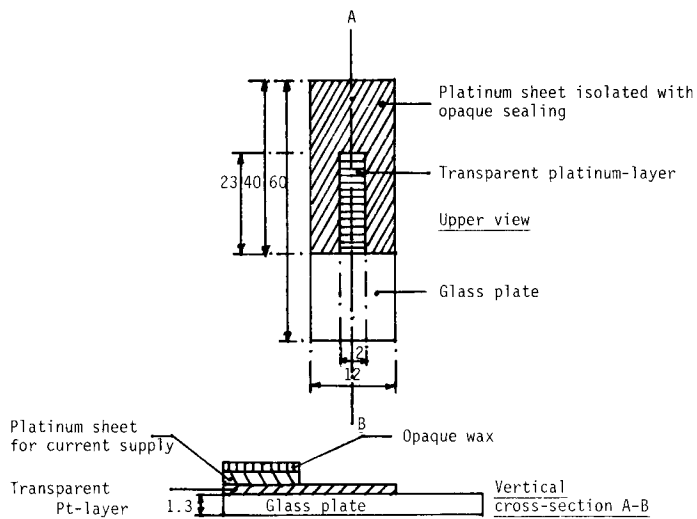
Fig. 3.6 Transparent Pt-electrode. Dimensions are given in mm.

The electrolysis was carried out in a perspex cell divided into two equal compartments (3 cm wide, 1 cm deep and 10 cm high) by a transparent cation-exchange membrane (Nafion 117). The cell is schematically represented in Fig. 3.4.

A perspex support of the working electrode was placed in the working electrode compartment, so that the cross-section of solution flow at the level of the working electrode was 72 mm^2 and the distance from the working electrode to the membrane 3 mm.

The optically transparent working electrode is schematically given in Fig. 3.6.

It consists of a glass (6.0 x 1.2 x 0.13 cm), of which the upper part of about 4 cm has been coated by sputtering it with platinum to about 30 nm.

For current-supply purposes, a thin platinum sheet with a window, 0.2 cm wide and 2.3 cm high, was glued onto the platinum coating layer and the surface of the sheet was isolated with opaque sealing wax.

The counter electrode was a perforated, 22 cm^2 nickel plate. It was situated in the middle of the counter-electrode compartment against the membrane. At working electrode height a hole was cut out of the counter electrode to ensure adequate passage of light.

The working electrode compartment was connected to a solution flow circuit, which consisted of a pump (Schmitt-Kreisel, type MPN-100), a flowmeter (no. 3F-3/8-25-5/36), a heat exchanger, a degassing reservoir and taps. The heat exchanger was thermostatted.

The working electrode compartment was filled with a solution of 4 M NaCl plus 0.1 M HCl, and was saturated with chlorine gas.

The counter electrode compartment was filled with a solution of 10 M NaOH. The electrodes were fed galvanostatically (Delta Elektronika, E030-1) and the current measured with an ammeter (Keitly 191 digital multimeter).

The optical arrangement used is schematically illustrated in Fig. 3.3. Against-the-light photography was used. For this film technique it was necessary to use a transparent plane vertical Pt-electrode. The benefit of this method works out in a sharply contrasted image of the bubble boundary seen on the pictures. Visibility of the attached-bubbles is not disturbed by rising bubbles, since the active side of the transparent electrode is focussed toward the light source. The bubbles were filmed with a high-speed film camera (Hitachi, NAC 16HD). The light source was a

Hg-lamp (Oriel, model 6144) and was placed at the opposite side of the camera. To focus the light beam on the active side of the transparent electrode, two positive lenses and one diaphragm were used. Due to the small sizes of the bubbles a microscope was required to measure the bubble diameter. In order to determine the magnification factor, a graduated scale of 1 mm was divided in 100 equal parts and placed at the position of the working electrode.

The camera initiated a light mark on the edge of the film every millisecond, so that the picture frequency could be determined.

Sharp pictures were obtained at picture frequencies of 100 to 500 frames per second for low and high current densities, respectively.

The exposed films (Kodak, 4-x reversal film 7277) were developed in a combilabor (Old Delft CMB-A-2). The bubble diameters and the number of bubbles on the surface of the working electrode (0.02939 cm^2) were measured on the screen of a motion analyser (Hitachi, NAC MC-OB/PH-160B). The data obtained were punched on paper tape and processed by the university computer system (Burroughs 7700). The computer programm was able to calculate different bubble parameters, such as: average bubble radius, average degree of screening, etc. The measured values of the bubble parameters were averaged, because of their fluctuation. To cover the bubble behaviour in different stages, approximately ten frames of the film for each experimental condition were used to obtain sufficiently accurate bubble parameters.

Unless otherwise mentioned, the experiments were performed galvanostatically with a chlorine-evolving transparent platinum electrode in 4 M NaCl plus 0.1 M HCl solution, at atmospheric pressure, 298 K and a solution flow velocity of 0.05 m/s.

No results could be obtained at a higher temperature (353 K), because the transparent platinum electrode started to crack from a temperature of approximately 323 K onwards, and finally peeled off. Further efforts to improve the transparent electrode have not resulted in a stable working electrode.

3.4 Results

3.4.1 Preceeding remarks

The bubble parameters of attached-bubbles at the electrode surface

fluctuate around a quasi-stationary state [2].

The extent of the fluctuation depends on many factors, for instance: electrode orientation, nature of gas evolved and electrolyte conditions. Additionally, the quasi-stationary state changes with increasing electrolysis time and finally becomes nearly constant. To cover the bubble behaviour in different stages, an adequate number of film frames has to be used to obtain sufficiently accurate bubble parameters. It has been found that approximately 10 successive pictures were required to obtain reliable averages of the bubble parameters.

The filming of the bubbles was started 15 minutes after electrolysis to enable the system to reach a steady state. Bubble evolution was uniformly distributed over the transparent electrode surface.

3.4.2 Effect of current density

The effect of current density on the bubble parameters d, R_a, R_s, s and V_a, is given in Table 3.1.

Nature of gas	$i(kA\ m^{-2})$	$v_s(m\ s^{-1})$	$d[(mm)^{-2}]$	$R_a(\mu m)$	$R_s(\mu m)$	s	$V_a(\mu m)$
Cl_2	5	0.05	19	112	164	0.95	208
	4	0.05	20	109	180	0.99	240
	3	0.05	17	113	209	0.96	268
	2	0.05	14	108	224	0.81	242
	1	0.05	13	107	301	0.87	357
	0.5	0.05	12	97	303	0.67	279
	0.25	0.05	6	135	300	0.61	244
	0.1	0.05	2	225	380	0.48	243
	0.5	0.05	10	114	317	0.80	335
	2	0.05	15	120	213	0.96	277

Table 3.1 Effect of i on d, R_a, R_s, s and V_a for chlorine-evolving vertical transparent platinum electrode in 4 M NaCl plus 0.1 M HCl solution at 101 kPa, 298 K and $v_s = 0.05\ m\ s^{-1}$.

The results are tabulated in sequence of performance of the experiments. Table 3.1 shows that R_a and R_s decreases rapidly with increasing current density in the current density range from 0.1 to 1 kA/m^2 and slowly at i > 1 kA/m^2. The volume of attached-bubbles is practically independent of the current density for the current range from 0.1 to 5 kA/m^2.

Since the projections of some attached-bubbles coincide partly or completely, the calculated degree of screening, s, is too high. Therefore, s(x) has been calculated.

In Fig. 3.7, s(x) is plotted as a function of the distance from the electrode surface, x, for various current densities. The figure shows curves with a maximum. This maximum, $s(x)_{max}$, increases at a decreasing rate with increasing current density.

Since the contribution of detached-bubbles is not taken into account, $s(x)_{max}$ gives too small a value for the degree of screening of the electrode by bubbles. To compare s and $s(x)_{max}$, both are represented in Fig. 3.8. This figure shows that s reaches a limiting value already at a lower current density than $s(x)_{max}$. In Fig. 3.9 the ratio s/(1-s) is plotted as a function of current density on a double logarithmic scale, at T = 298 K and v_s = 0.05 m s^{-1}.

The relation between the degree of screening and the current density can be given by:

$$\frac{s}{1-s} = a_1 i^{n_1} \tag{3.22}$$

Rearrangement of this relation gives:

$$s = \frac{a_1 i^{n_1}}{1 + a_1 i^{n_1}} \tag{3.23}$$

where a_1 and n_1 are constants. The curve of Fig. 3.8 obeys the equation:

$$s = \frac{5.6(i)^{0.9}}{1 + 5.6(i)^{0.9}} \tag{3.24}$$

where i is given in kA/m^2.
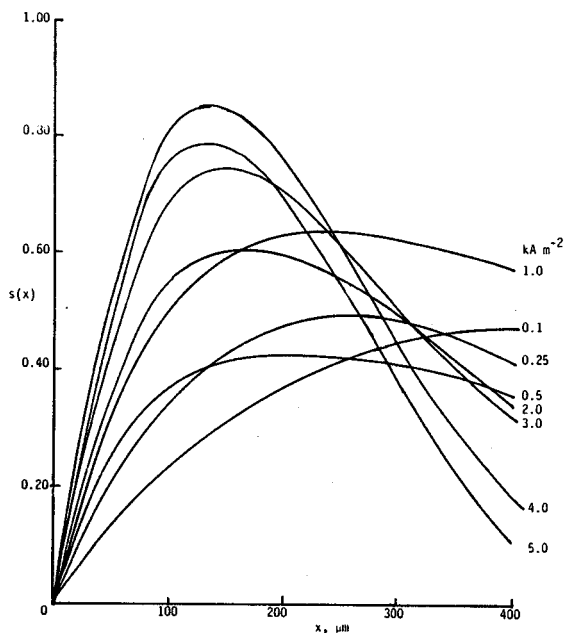
Fig. 3.7 *Effect of current density, i, on the average degree of screening of the electrode at a distance x from the electrode by attached-bubbles for a chlorine-evolving vertical transparent platinum electrode in 4 M NaCl plus 0.1 M HCl solution at 101 kPa, 298 K and $v_s = 0.05$ m s^{-1}.*
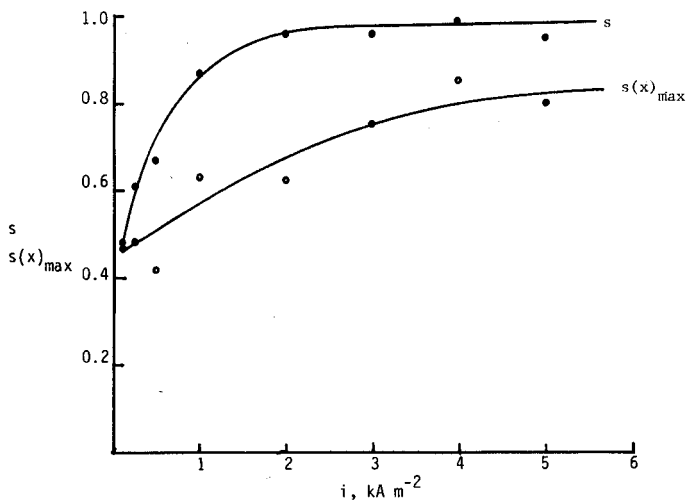
Fig. 3.8 *Effect of i on s and $s(x)_{max}$ for a chlorine-evolving vertical transparent platinum electrode in 4 M NaCl plus 0.1 M HCl solution at 101 kPa, 298 K and $v_s = 0.05$ m s^{-1}.*
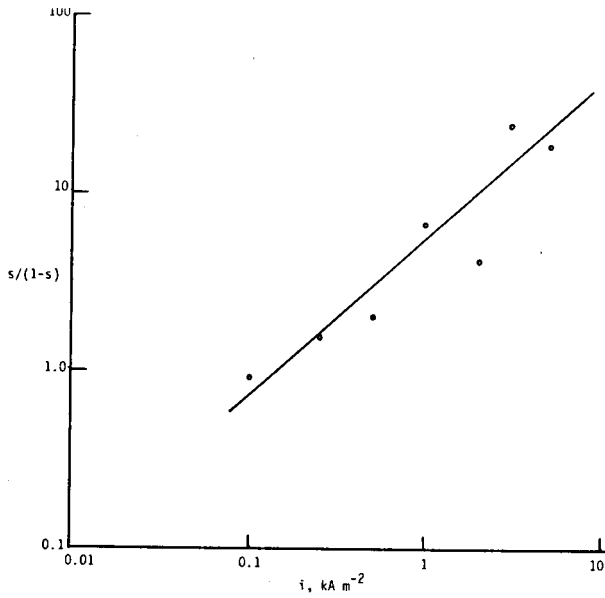
Fig. 3.9 s/(s-s) as a function of current density on double logarithmic scale; $T = 298$ K, $v_s = 0.05$ m s^{-1}.
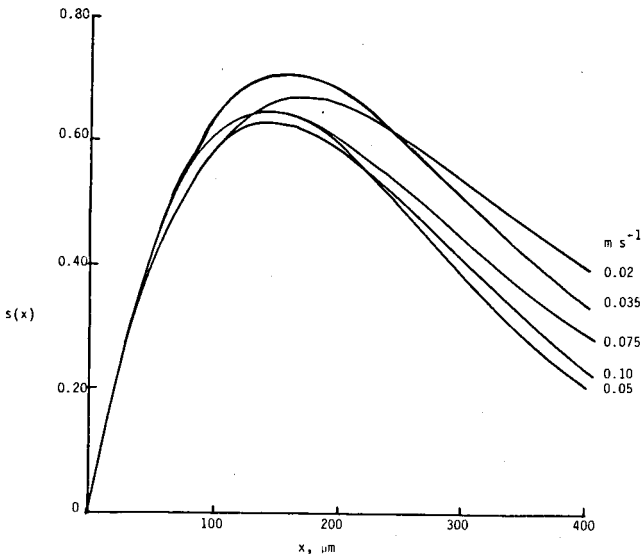
Fig. 3.10 Effect of solution flow velocity on the average degree of screening of the electrode at a distance x from the electrode by attached-bubbles for a chlorine-evolving vertical transparent platinum electrode in 4 M NaCl plus 0.1 M HCl solution at 101 kPa 298 K and $i = 2$ kA m^{-2}.

3.4.3 Effect of solution flow velocity

The effect of solution flow velocity was measured at increasing v_s. The bubble parameters are given in Table 3.2.

Nature of gas	v_s (m s^{-1})	i (kA m^{-2})	d [(mm)$^{-2}$]	R_a (μm)	R_s (μm)	s	V_a (μm)
Cl$_2$	0.020	2	15	111	245	0.93	307
	0.035	2	15	119	230	0.96	302
	0.050	2	17	105	185	0.83	185
	0.075	2	18	217	217	0.89	263
	0.100	2	16	104	196	0.83	222

Table 3.2 Effect of v_s on d, R_a, R_s, s and V_a for a chlorine-evolving vertical transparent platinum electrode in 4 M NaCl plus 0.1 M HCl solution at 101 kPa, 298 K and i = 2 kA m^{-2}.

This table shows that R_a, R_s, s and V_a decrease slowly with increasing v_s. The effect of v_s on d is questionable. It may be concluded that d increases a little with increasing v_s.
Fig. 3.10 shows s(x) as a function of x for various v_s.
The maximum value of s(x), s(x)$_{max}$, and s are plotted as a function of v_s in Fig. 3.11. This figure shows that s(x)$_{max}$ and s decrease with increasing v_s.
In Fig. 3.12, the ratio s/s$_o$-s is plotted versus the solution flow velocity on a double logarithmic scale at T = 298 K and i = 2 kA m^{-2}.

The relation between the degree of screening and the solution flow velocity can be represented by:

$$\frac{s}{s_o - s} = a_2 v_s^{n_2} \qquad (3.25)$$

Rearranging equation (3.25) yields:

$$s = \frac{a_2 s_o v_s^{n_2}}{1 + a_2 v_s^{n_2}} \qquad (3.26)$$

where s_o , the maximum of screening at natural convection, obtained by extrapolation of the s/v_s curve (s_o = 1, cf. Fig. 3.11), depends on current density [3,5]; a_2 and n_2 are constant. The curve of Fig. 3.11 obeys the equation :
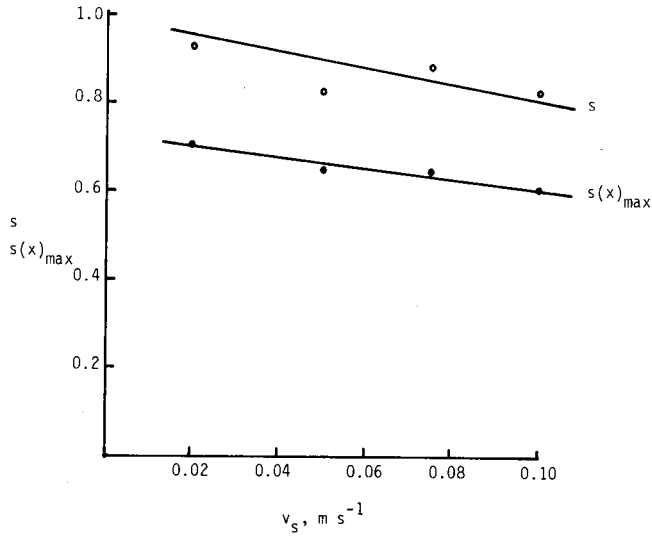
Fig. 3.11 Effect of solution flow velocity on s and s(x)$_{max}$ for a chlorine-evolving vertical transparent platinum electrode in 4 M NaCl plus 0.1 M HCl solution at 101 kPa, 298 K and i = 2 kA.
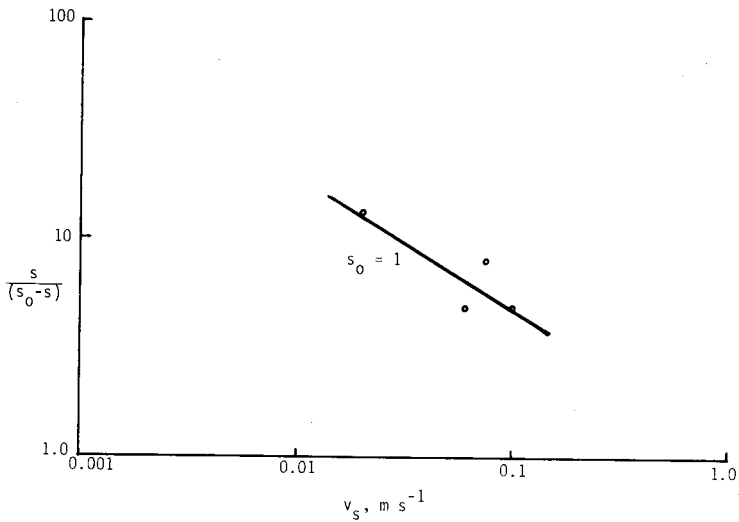
Fig. 3.12 s/(s$_0$-s) as a function of solution flow velocity on double logarithmic scale; T = 298 K, i = 2kA m^{-2}.

$$s = \frac{1.2 \ (v_s)^{-0.6}}{1 + 1.2 \ (v_s)^{-0.6}} \qquad\qquad (3.27)$$

3.5 Discussion

The results from Tabel 3.1 indicate that the bubble population density, d, and the attached-bubble radius, R_a, increases, respectively, decreases with increasing i. The supersaturation concentration of dissolved gas at the electrode surface is small at small i (cf. Eq. 3.2). Hence, according Eq. 3.3, only big cavities will be activated.

At increasing i, the supersaturation of dissolved gas will increase (see results Chapter 4), so that small cavities become also active. Consequently, d and R_a increases, respectively, decreases with increasing i.

As the degree of screening, s, is proportional to d . R_a, and, in addition, d increases faster with increasing i than R_a decreases with increasing i, s increases with increasing i.

During the growth the chlorine bubble remains at its initiation site. Even at a solution flow velocity of $0.1 \ ms^{-1}$, the position of the chlorine bubble does not change, supporting the assumption that the bubbles are cavity bubbles (cf. Section 5.5).

The volume of attached chlorine bubbles per unit area of electrode surface is almost independent of the current density for the entire range of current density. Table 3.2 shows that the attached-bubble radius decreases with increasing solution flow velocity, v_s, because increasing v_s increases the upward force on the attached-bubbles. Consequently, smaller bubbles are expected. Fig. 3.8 shows that the degree of screening, s, is very high and almost constant, approximately 0.96, at i $\geq 2 \ kAm^{-2}$; $s(x)_{max}$ is also almost constant, viz. 0.8, at i $\geq 4 \ kAm^{-2}$. This high degree of screening suggests that the gas voidage of the liquid-bubble layer near the surface of the gas-evolving electrode with a thickness of the average diameter of the attached-bubbles (about 220 μm) must be very high.

Taking the different calculation methods for s and $s(x)_{max}$ into account, it can be shown that the gas voidage is > 0.60.

The maximum gas voidage can be derived from geometric considerations for several lattice types of bubble arrangement.

For example, if we assume bubbles of the same size in a body-centered cubic structure, then the maximum gas voidage is 0.52. For a face-centered cubic close-packed structure this value is 0.74.

By comparing the results, it can be concluded that the gas-voidage in the 220 µm thick liquid-bubble layer is about maximum.

This high gas-voidage near the electrode surface increases the ohmic resistance of the liquid-bubble layer near the surface of a gas-evolving electrode significantly, especially, when the electrode is a flat-plate electrode. It should be emphasized that this bubble effect can be reduced to a negligable value by applying the appropriate electrode configuration (cf. Chapter 9).

3.6 References

1   H. Vogt, Fortschr. Verfahrungstechnik 20 (1982) 369

2   C.W.M.P. Sillen, Thesis, Eindhoven University of Technology (1983)

3   L.J.J. Janssen, C.W.M.P. Sillen, E. Barendrecht and S.J.D. van Stralen, Electrochmi. Acta. 29 (1984) 633

4   L.J.J. Janssen and S.J.D. van Stralen, Electrochim. Acta. 26 (1981) 1001

5   B.E. Bongenaar-Schlenter, Thesis, Eindhoven University of Technology (1984)

6   K.J. Vetter, Elektrochemische Kinetik, Springer Verslag, Berlin (1961)

7   S.J.D. van Stralen and R. Cole, Boiling Phenomena, Hermisphere Publishing Corporation, Washingtin (1979)

8   D.E. Westerheide and J.W. Westwater, A.I.Ch.E. Journal 7 (1961) 357

9   C.W.M.P. Sillen, L.J.J. Janssen, E. Barendrecht and S.J.D. van Stralen, Electrochim. Acta. 29 (1984) 633

10 L.J.J. Janssen and S.J.D. van Stralen, Electrochim. Acta 26 (1981) 1011

11 H.F.A. Verhaart, R.M. de Jonge and S.J.D. van Stralen, Int. J. Heat Mass Transfer 23 (1980) 293

12 W. Zijl, Ph.D. Thesis, Eindhoven University of Technology (1979)

13 J.P. Glas and J.W. Westwater, Int. J. Heat Mass Transfer 7 (1964) 1427

14 P.C. Slooten, Ph.D. Thesis, Eindhoven University of Technology (1984)

15 R. Cole and H.L. Shulman, Chemical Engineering Progress Symposium
    Series, Heat Transfer, Los Angeles 62 (1966) 6
16 A.K. Chesters in: S.J.D. van Stralen and R. Cole, Boiling Phenomena,
    Hemisphere Publishing Corporation, Washington, Chapter 26 (1979)
17 W. Fritz, Phys. Zeitschrift 11 (1935) 379
18 J.S. Saini, C.P. Gupta and S. Lal, Int. J. Heat Mass Transfer 18
    (1975) 472
19 A.M. Kiper, Int. J. Heat Mass Transfer 14 (1971) 931
20 L.J.J. Janssen and E. Barendrecht, Electrochim. Acta 30 (1985) 683
21 J.E. Funk and J.F. Thorpe, J. Electrochem. Soc. 116 (1969) 48
22 L.E. Scriven, Chem. Eng. Sci. 10 (1959) 1

Chapter 4

Gas supersaturation at gas-evolving electrodes
under conditions of forced convection

4.1 Introduction

The phenomenon of gas supersaturation has already been stipulated in Section 3.2.1.

The supersaturation concentration, $c_g^\sigma - c_g^s$, depends on many factors, such as: rate of gas formation, solution velocity, number of active nucleation sites, nature and solubility of the gas evolved, growth rate of bubbles, bubbles size, coalescence behaviour and the adhesion of bubbles to the electrode surface. All these factors affect each other in a very complex manner.

Up till now, only some experimental results have been published on gas supersaturation. Moreover, they show wide scattering [1], seeming to be caused by the different applied measuring techniques.

The method used to determine the supersaturation for hydrogen, oxygen and chlorine is based on the determination of the efficiency of gas bubble evolution and of the mass transfer coefficient for the indicator ion moving towards the gas-evolving electrode.

In Section 4.2, the experimental equipment and conditions are described.

In Section 4.3, the results are presented. The results are discussed in Section 4.4.

4.2 Experimental

A schematic diagram of the measuring system is shown in Fig. 4.1.

The working electrode compartment had an inner cross section of 1.35 cm^2 and a length of about 10 cm and was provided with a wire-type working electrode. This wire electrode was placed vertically in the middle of the tube opposite both membranes.

Two platinum plates of about 30 mm^2 each were used as counter electrodes. To obtain a stable laminar liquid flow, a grid was placed in the lowest part of the cell.

The current was adjusted galvanostically (Delta Electronika, E 015-20)

and measured with an ammeter (Keitly 191, digital multi- meter). The solution volume in the working electrode compartment was about 500 cm^3. The volumetric flow-rate of the thermostatted solution through the working electrode compartment was measured with a calibrated flow meter (F & P Co., Precision Bore flowrator, tube No. F.P.-3/8-25-G-5/36, stainless steel or glass float).

For the hydrogen and oxygen experiments, the working electrode was a nickel wire with a diameter of 0.5 x 10^{-3} m and a length of 2.8 x 10^{-3} m (surface area 4.59 x 10^{-6} m^2); the working electrode and the counter electrode compartment were filled with 1 M and 10 M KOH, respectively. In case of the chlorine evolution, a platinum wire working electrode was used; the working electrode compartment was filled with 0.5 M HCl and the counter electrode compartment with 6 M HCl.

High-concentration KOH and HCl solutions were used in the counter electrode compartment to avoid exhaustion. The mass transfer coefficients, k_{fi} (for ferricyanide ions at a hydrogen-evolving electrode), k_{fo} (for ferrocyanide ions at a oxygen-evolving electrode and k_{co} (for cero ions at a chlorine-evolving electrode), were determined in sequence of increasing current densities at constant solution flow velocity.

Sixty minutes after the previous sampling, a new sample of 50 ml was taken and analyzed, etc. The time of electrolysis for each series of electrolysis was about 5 hours.

The bulk concentrations of ferrocyanide, $c^s{}_{fo}$, and ferricyanide, $c^s{}_{fi}$, formed during the hydrogen and oxygen evolution, respectively, were determined with a platinum disc electrode, rotating at 64 rps.

The concentration of ceri ions, $c^s{}_{ci}$, formed during the chlorine evolution, was determined potentiometrically with 0.005 M ferroammoniumsulfate solution. The results obtained by this method were more reliable than those with the RDE method.

It has been found that $c^s{}_{fo}$, $c^s{}_{fi}$ and $c^s{}_{ci}$ increased linearly with time of electrolysis, t_e. The mass transfer coefficients, k_{fi}, k_{fo} and k_{co} were calculated from :

$$k_{fi} = \frac{V^s_s}{c^s_{fi} A_e} \frac{dc_{fo}}{dt_e} \qquad (\text{m s}^{-1}) \qquad (4.1)$$
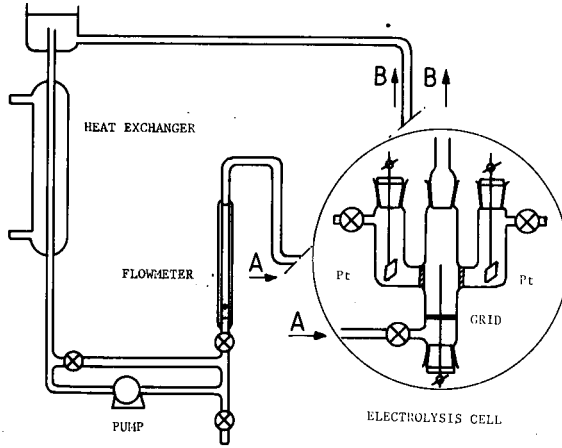
Fig. 4.1 Flow circuit and measuring cell.

$$k_{fo} = \frac{V_s}{c_{fo}^s A_e} \frac{dc_{fi}^s}{dt_e} \qquad (m\ s^{-1}) \qquad (4.2)$$

$$k_{co} = \frac{V_s}{c_{co}^s A_e} \frac{dc_{ci}^s}{dt_e} \qquad (m\ s^{-1}) \qquad (4.3)$$

where V_s = the solution volume in the working electrode compartment in m^3; c_{fi}^s, c_{fo}^s and c_{co}^s are the average bulk concentrations of the indicator ions in kmol m^{-3} during the electrolysis; A_e = the surface area of the working electrode in m^2 and

$\dfrac{dc_{fo}^s}{dt_e}$, $\dfrac{dc_{fi}^s}{dt_e}$ and $\dfrac{dc_{ci}^s}{dt_e}$ are the slopes of the linear function c_{fo}^s/t_e, c_{fi}^s/t_e

and c_{ci}^s/t_e, respectively.

4.3 Results

4.3.1 Mass transfer coefficient

As known, diffusion determines both the ferricyanide reduction at $i_H > 0$ kA m^{-2} and the ferrocyanide oxidation at $i_0 > 0.1$ kA m^{-2} [3].
This means that under these conditions the concentration of the indicator ions at the electrode surface, c_i^{σ}, is zero.

The mass transfer coefficient k_i of the indicator ion i, towards a gas-evolving electrode, is calculated with:

$$k_i = \frac{v_i}{c_i^s A_e} = \frac{I_i}{n_i F c_i^s A_e} \quad (m\ s^{-1}) \qquad (4.4)$$

where v_i = the rate of oxidation or reduction of the indicator ion i (kmol s^{-1}), c_i^s = the concentration of the indicator ions in the bulk (kmol m^{-3}), A_e = the electrode surface (m^2), n_i = number of electrons, involved in the electrode reaction for indicator ion i (keq. $kmol^{-1}$, in our case = 1), F = 96.487×10^6 (C keq^{-1}) and I_i = the current for the oxidation or reduction of the indicator ion i. So $I_i = n_i F v_i$ and, consequently, both I_H, I_0, or $I_{Cl} = I - I_i$, where I_H, I_0 and I_{Cl} are the currents required for the formation of hydrogen, oxygen and chlorine (kA), respectively, and I = the adjusted current (kA). For the simultaneous and stationary electrolysis, the diffusion layer of the indicator ion, δ_i, and of the dissolved gas, δ_g, are related by:

$$\frac{\delta_g}{\delta_i} = \left[\frac{D_g}{D_i}\right]^{1/3} \quad \text{or} \quad k_g = \left[\frac{D_g}{D_i}\right]^{2/3} k_i \quad (m\ s^{-1}) \qquad (4.5)$$

where k_g = the mass transfer coefficient of the dissolved gas; D_g and D_i are the diffusion coefficients of the dissolved gas and the indicator ion, respectively ($m^2\ s^{-1}$). These formulae are based on the assumption that mass transfer of the indicator ion and of the dissolved gas occur simultaneously, but in opposite direction.

4.3.2 Supersaturation concentration at gas-evolving electrodes

The part of gas generated at an electrode, that is not absorbed by the bubbles present on the electrode surface, is transported as dissolved gas to the bulk-solution by diffusion, forced convection and convection induced by detached and rising bubbles.
The transport rate of the dissolved gas from the electrode surface into the bulk-solution = $(1 - \eta_b) i_g / n_g F$.

We assume that this rate equals $k_g (c_g^\sigma - c_g^s)$,

where: η_b = the efficiency of gas bubble evolution (cf. Section 5.4), i_g

= the electric current density for total gas evolution (kA m^{-2}), n_g = the number of electrons, involved in the electrode reaction to form one molecule of gas (n_g = 4 keq kmol^{-1} for O_2, n_g = 2 for both H_2 and Cl_2), F = the Faraday constant, c^{σ}_g = the surface concentration of dissolved gas at the electrode surface, including the saturation concentration and c^s_g = the concentration of dissolved gas in the bulk–solution at 298 K and 101 kPa (kmol m^{-3}).

Consequently, c^{σ}_g can be calculated by the equation:

$$c^{\sigma}_g = \frac{(1-\eta_b)i_g}{n_g F k_g} + c^s_g \quad (\text{kmol m}^{-3}) \qquad (4.6)$$

4.3.3 Hydrogen–evolving electrode

The mass transfer coefficient of the indicator ion ferricyanide, k_{fi}, is plotted versus i_H in Fig. 4.2 for a hydrogen–evolving Ni electrode in 1 M KOH as supporting electrolyte, at 298 K and v_s = 0.12 m s^{-1}. Fig. 4.2 shows that k_{fi} = (3.60 + 0.28 i_H) x 10^{-5} m s^{-1} with i_H expressed in kA m^{-2}. The k_{fi} increases relatively slightly with increasing current density for hydrogen evolution.

The mass transfer coefficient, $k_{f,fi}$, at forced convection and in absence of gas formation has been obtained by determining the limiting current of ferricyanide reduction, at a working–electrode potential of –0.5 V vs. SCE: $k_{f,fi}$ = 1.2 x 10^{-5} m s^{-1}, at v_s = 0.12 m s^{-1} and T = 298 K.

Linear extrapolation of k_{fi} to i_H = 0 gives a value of 3.60 x 10^{-5} m s^{-1}, which is higher than the value of $k_{f,fi}$. The mass transfer coefficient of hydrogen, k_H, equals $(D_H/D_{fi})^{2/3}$ k_{fi}, where D_H = 30 x 10^{-10} m^2 s^{-1} [4] and D_{fi} = 7.9 x 10^{-10} m^2 s^{-1} [5] and k_H = (8.76 + 0.68 i_H) x 10^{-5} m s^{-1}, with i_H expressed in kA m^{-2}.

The supersaturation concentration of dissolved hydrogen at the electrode surface, c^{σ}_H, equals:

$$c^{\sigma}_H = \frac{(1-\eta_H)i_H}{n_H F k_H} + c^s_H \quad (\text{kmol m}^{-3}) \qquad (4.7)$$

The efficiency of hydrogen bubble evolution, η_H, and the saturation concentration c^s_H = 0.52 10^{-3} kmol m^{-3} for hydrogen at 101 kPa are reported in Section 5.4 and [4].

The degree of hydrogen supersaturation, i.e. the ratio c^{σ}_H/c^s_H is shown
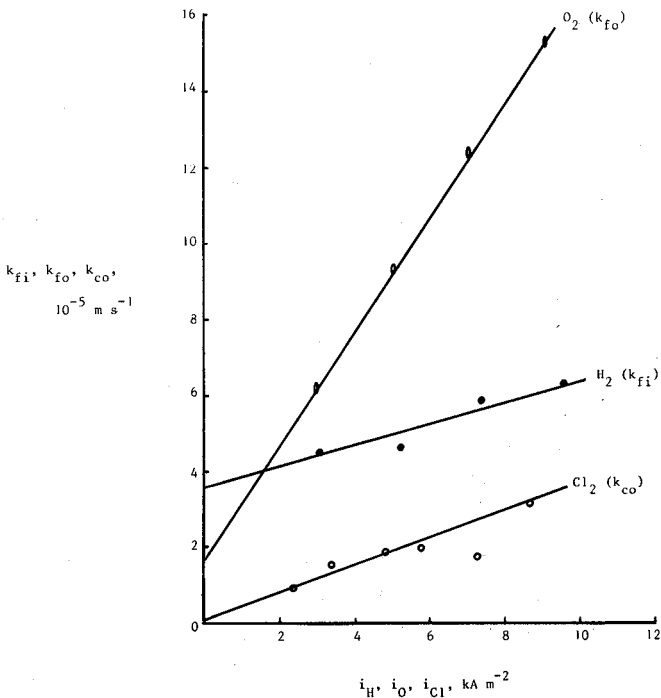
Fig. 4.2   Mass-transfer coefficient of fi and fo, respectively, to a hydrogen- and oxygen-evolving nickel wire electrode in 1 M KOH at 298 K and v_s = 0.12 m s^{-1} vs. the current density for hydrogen and oxygen evolution, respectively, and the mass transfer coefficient of co to a chlorine-evolving platinum wire electrode in 0.5 M HCl at 298 K and v_s = 0.12 m s^{-1} vs. the current density for chlorine evolution.

as a function of i_H in Fig. 4.3. This figure indicates that c^{σ}_H/c^s_H increases rapidly with increasing i_H in the current density range from 0 to 2 kA m^{-2}.

4.3.4 Oxygen—evolving electrode

Fig. 4.2 shows the mass transfer coefficient of the indicator ion fo, k_{fo}, as a function of i_0 for an oxygen—evolving electrode in 1 M KOH, at 298 K and v_s = 0.12 m s^{-1}. This curve fits k_{fo} = (1.60 + 1.51 i_0) x10^{-5} m s^{-1} with i_H expressed in kA m^{-2}.
The k_{fo} value increases linearly and rather steep with increasing current density for oxygen evolution. The $k_{f,fo}$—value for the fo—oxidation in absence of gas formation, at 298 K and v_s = 0.12 m s^{-1} and at a working—electrode potential of +0.45 V was 1.1 x 10^{-5} m s^{-1}.
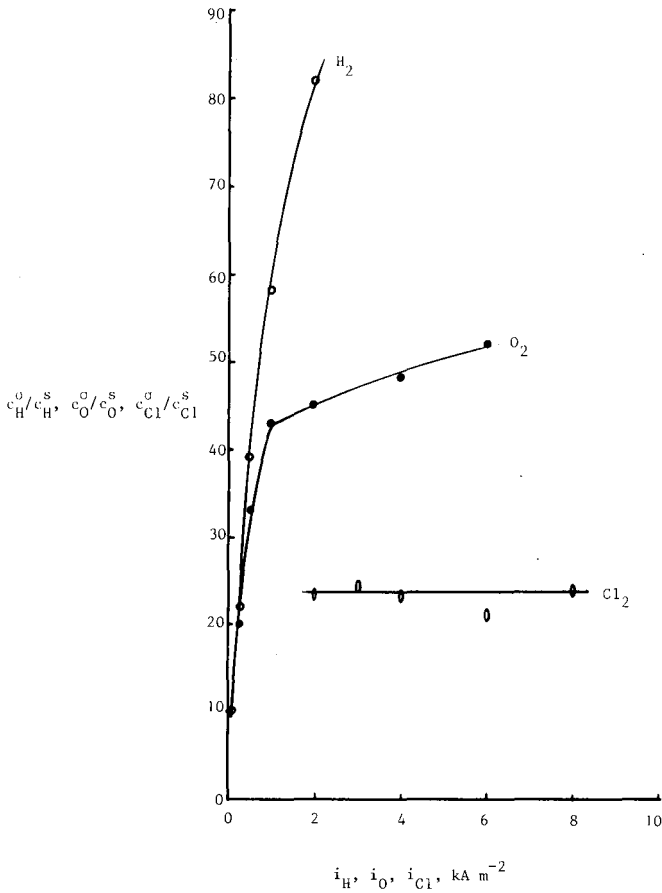
Fig. 4.3 Degree of supersaturation vs. current density for a hydrogen, an oxygen- and a chlorine-evolving electrode at similar conditions as for Fig. 4.2.

The linear extrapolation of k_{fo} to $i_0 = 0$ gives $k_f = 1.60 \times 10^{-5}$ m s^{-1}.
Both mass transfer coefficients are approximately the same.
The mass transfer coefficient of oxygen, k_0, is given by $(D_0/D_{fo})^{2/3} k_{fo}$,
where $D_0 = 1.59 \times 10^{-9}$ m^2 s^{-1} [4] and $D_{fo} = 7.0 \times 10^{-10}$ m^2 s^{-1} [5], i.e.
$k_0 = (2.76 + 2.61\ i_0) \times 10^{-5}$ m s^{-1} with i_0 in kA m^{-2}.
The concentration of dissolved oxygen at the electrode surface , $c^{\sigma}_0 =$
$(1-\eta_0)i_0/\eta_0 F k_0 + c^s_0$, where $c^s_0 = 0.89 \times 10^{-3}$ kmol m^{-3} at 101 kPa and η_0
= the efficiency of oxygen bubble evolution; see cf. Section 5.4 and [6].
Fig. 4.3 indicates that c^{σ}_0/c^s_0 increases very fast with increasing i_0 in

the current density range of 0 to 1 kA m^{-2} and then it increases more slightly.

4.3.5 Chlorine-evolving electrode

No oxidation of cero took place at a Pt or a RuO_2 electrode in 4 M NaCl + 0.1 M HCl solution or in 1 M HCl [4]. In both solutions ceri was quite unstable and even oxidizes Cl^- into chlorine. A diffusion limited current for cero oxidation was obtained at a Pt electrode in 0.5 M HCl at i_{Cl} > 1.5 kA m^{-2}, where the working electrode potential was > 1.8 V vs. SCE. The determination of ceri formed (in 0.5 M HCl) was carried out potentiometrically with 0.005 M ferroammoniumsulfate solution; the concentration found was corrected.

The mass transfer coefficient of the indicator ion cero, k_{co} = (0.05 + 0.37 i_{Cl}) x 10^{-5} m s^{-1} (cf. Fig. 4.2) with i_{Cl} expressed in kA m^{-2}. The k_{co} increases relatively slowly with increasing i_{Cl}. The mass transfer coefficient of chlorine, $k_{Cl} = (D_{Cl}/D_{co})^{2/3} k_{co}$, where D_{Cl} = 1.22 x 10^{-9} m^2 s^{-1} [6] and D_{co} = 7.1 x 10^{-10} m^2 s^{-1} [4]. Therefore, k_{Cl} = (0.09 + 0.64 i_{Cl}) x 10^{-5} m s^{-1}.

The concentration of dissolved chlorine at the electrode surface, c^{σ}_{Cl} = $(1-\eta_{Cl})i_{Cl}/n_{Cl}Fk_{Cl} + c^{s}_{Cl}$, where c^{s}_{Cl} = 22 x 10^{-3} kmol m^{-3} at 101 kPa and η_{Cl} = the efficiency of chlorine evolution; see cf. Section 5.4 and [3].

The degree of supersaturation of chlorine is, according to Fig. 4.3, independent of i_{Cl} in the current density range of 2 to 8 kA m^{-2}.

4.4 Discussion

Gas bubbles attached to the electrode surface hinder the mass transfer of indicator ions to the electrode surface. It seems that mass transfer is enhanced by slipping of attached-bubbles and by detached and rising bubbles.

Generally speaking, gas evolution enhances mass transfer of the indicator ions to the electrode surface. The degree of enhancement depends mainly on the gas bubble behaviour in question. Gas bubbles generated at the electrode surface can be divided into [7, 8]:

- gas bubbles, attached weakly to the electrode surface; they are slipping at the electrode surface, and detach in a slow rate from the electrode surface, and rise upwards in the solution; thereby, a

relatively weak solution flow velocity near the electrode surface is induced (e.g. hydrogen bubbles generated on a nickel electrode in alkaline solution);

- gas bubbles, attached strongly to the electrode surface; they touch surrounding attached-bubbles and coalesce during their growth; depending on the size of the coalesced bubbles, the new bubbles formed suddenly jump perpendicularly from the electrode surface and so cause a strong solution flow near the electrode surface (e.g. oxygen bubbles generated on a nickel electrode in alkaline solution).

It was found that the mass transfer coefficient, k_{fi}, at a forced convected hydrogen-evolving electrode is about three times higher than $k_{f,fi}$ (the mass-transfer coefficient of the f_i indicator ion at forced convection in the absence of gas bubble evolution). This can be explained qualitatively by the fact that, at very low current density, the weakly attached hydrogen bubbles are slipping at the electrode surface, causing an additional solution flow near the electrode surface. Therefore, the mass transfer near the electrode surface will increase.

For an oxygen evolving electrode, $k_{f,fo}$ is approximately the same as k_{fo}. This means that, at low current density, the strongly attached oxygen bubbles at the electrode surface induce practically no solution flow near the electrode surface. Fig. 4.2 shows that k_{fo} increases stronger with increasing current density than in case of k_{fi} or k_{co}. This is due to the coalescence behaviour of attached oxygen bubbles at high current denstiy. As mentioned before, the detached oxygen bubbles jump perpendicularly from the electrode surface and cause a jet flow to the electrode surface, resulting in a significant enhancement of the mass transfer of the indicator ion to the surface of an oxygen evolving electrode. Probably, the solution flow induced by the hydrogen or chlorine bubbles in the vicinity of the electrode surface is not that strong, because of the absence of coalescence. Some experimental results concerning the degree of supersaturation for a hydrogen- and an oxygen- evolving electrode have been published. Thus, Komshaya et al. [9] reported a degree of supersaturation (c^σ_g/c^s_g) of 10 to 15 for a nickel oxygen evolving electrode in 5.8 M KOH; Shibata [10-13] used different techniques and found at $i_H > 2$ kA m^{-2} a degree of supersaturation of 23 to 165 for a hydrogen evolving platinum electrode in 1 M H_2SO_4, and for a oxygen evolving platinum electrode in 1 M H_2SO_4, a degree of 71.

Rotating ring-disc and ring-cone electrodes were also used to determine

the degree of supersaturation [9,14].

The results obtained in Fig. 4.3 indicate that the degree of supersaturation of hydrogen and oxygen, respectively, increases with increasing current density. At $i_0 > 1$ kA m^{-2}, the degree of oxygen supersaturation tends to level out, perhaps because of coalescence. Similar results were found by Shibata [10-13].

Supersaturation concentration values of chlorine are not yet available in literature and are presented here for the first time. It appears that supersaturation is constant over a wide range of current densities for chlorine evolution. The experimental values for the degree of super-saturation are beyond the maximum value and can be calculated with:

$$\eta = (2.3RT/nF) \log (c_g^\sigma/c_g^s) \tag{4.8}$$

with η the pertaining overpotential.

However, a satisfying explanation needs more data, especially about the kinetics of dissolution.

4.5 References

1   H. Vogt, Comprehensive Treatise of Electrochemistry (edited by E. Yeager,
    J.O.M. Bockris, B.E. Conway and S. Sarangapani), Vol. 6, (1983) 445
2   L.J.J. Janssen, E. Barendrecht and S.J.D. van Stralen, Extended Abstracts, 36th ISE-Meeting, Spain (1985) 04020
3   A.M. Yatkovski and N.A. Fedotov, R.J. Phys. Chem. 43, (1969) 575
4   L.J.J. Janssen and J.G. Hoogland, Electrochim. Acta 15, (1970) 1013
5   L.J.J. Janssen, Electrochim. Acta 23, (1978) 81
6   F.T.B.J. van den Brink, Thesis, Eindhoven University of Technology (1981)
7   L.J.J. Janssen and S.J.D. van Stralen, Electrochim. Acta 26, (1981) 1011
8   L.J.J. Janssen and E. Barendrecht, Electrochim. Acta 24, (1979) 693
9   E.A. Khomskaya and A.S. Kolosov, Sov. Electrochem. 6, (1970) 245
10 S. Shibata, Bull. Chem. Soc. Japan 36, (1963) 53
11 S. Shibata, Electrochim. Acta 23, (1978) 619
12 S. Shibata, Bull. Chem. Soc. Japan 33, (1960) 1635
13 S. Shibata, Denki Kagaku 44, (1976) 709
14 L.J.J. Janssen and E. Barendrecht, Electrochim. Acta 29 (1984) 1207

Chapter 5

Bubble departure and efficiency of gas
bubble evolution for a chlorine-, a hydrogen-
and an oxygen-evolving wire electrode

5.1 Introduction

Electrogenerated bubbles at gas-evolving electrodes have received much
attention, because of their industrial importance.
All theoretical work performed in the past concerns the departure
mechanism of a single growing bubble on a horizontal wall in a
convectionless solution.
The bubble departure radius of a relatively large bubble can be
calculated with the Chesters equation (cf. Section 3.2.2). It is quite
difficult to verify the calculated result experimentally, because the
required contact angle of the bubble or the bubble foot radius are
generally unknown and hardly determinable.
It is evident that for practical, i.e. industrial purposes, the
multi-bubbles system is important. At present no theoretical treatment of
the multi-bubbles system is available; the few experimental results
published are not very trustworthy and even questionable [1]. Therefore,
it was decided to determine the bubble behaviour in a more thorough and
comprehensive manner.
So far, little has been done on the efficiency of gas bubble evolution at
a gas-evolving electrode. Only some experimental results in that respect
are known in the literature [2-5].
In this investigation the bubble parameters and the efficiency of gas
bubble evolution were determined under semi-industrial conditions. In
this chapter a short literature review is presented in Section 5.2.
In Section 5.3, the experimental set-up of the determination of departure
bubble parameters, efficiency of gas bubble evolution and preparation
method of electrodes are described. The results obtained are presented in
Section 5.4. The results are discussed and explained in Section 5.5.

5.2 Literature review

5.2.1 Size of depature bubbles

An extensive discussion about the size of departure bubbles is presented by Chesters [5] and van Stralen [6].

Recently, Brandon and Kelsall [7] have given experimental bubble departure radii for hydrogen-, oxygen- and chlorine-evolving micro-electrodes, on which only one bubble was present. Their results cannot be explained by the presently derived theoretical relations. They proposed that the electrostatic force between the bubble and electrode double layer controlled the bubble departure radius and that the gas and solid phase were separated by a thin liquid film. A similar idea was suggested by Coehn in 1933 [8]. In the same year Kabanow and Frumkin showed that during the departure process the electrostatic force is negligible in comparison to the buoyancy force.

In their theory the contact angle, ϕ, is a major factor, being proportional to the electrode potential or the current density [9].

5.2.2 Efficiency of gas bubble evolution

The product at the gas-evolving electrode is only partly present as bubbles. This fraction is called the efficiency of gas bubble evolution, η_b.

Vogt [10] has reported some calculated results. Van Stralen et al. [11] and Brandon et al. [7] found experimentally, for a single-bubble electrode system, that η_b increases with increasing ratio of bubble to electrode radius, increasing degree of screening of the electrode by the attached bubble or with increasing circumference of the cross-section of the attached bubble. Sides and Tobias [12] calculated theoretically the current distribution around a spherical bubble in contact with a plane electrode. They found that the current density is zero at the contact point and that the current denstity is 10% and 80% of its undisturbed value at $0.44 \, R_a$ and $0.95 \, R_a$, respectively, where R_a is the attached bubble radius, measured from the contact point.

According to Dukovic and Tobias [13], the evolved gas for a multi-bubbles system is mainly formed at the unscreened electrode surface.

5.3 Experimental

5.3.1 Determination of bubble departure parameters and efficiency of gas bubble evolution

The experimental set-up of the electrolytic cell and solution flow circuit is almost the same as described in Fig. 4.1. Only the solution reservoir for the working electrode was bigger (about 2000 cm^3).
The optical arrangement is shown in Fig. 5.1.
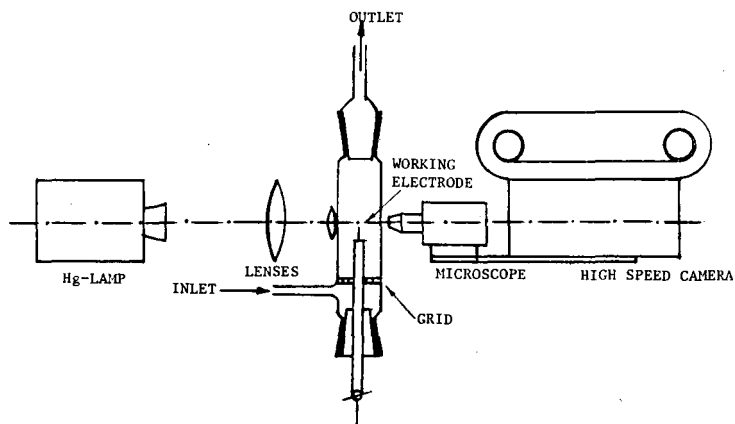
Fig. 5.1 Optical set-up at forced convection.

The same optical technique and computer program, as described in Section 3.3, were used to measure the bubble parameters. The departing chlorine, hydrogen and oxygen bubbles were filmed with a high-speed film camera in a space 1.7 mm above the working electrode.
The diameters of all evolved bubbles passing a imaginary line during a certain time (about 0.8 second) were measured by means of a motion analyser.
By using a wire-working electrode, all evolved gas bubbles were in the pictured area (1.7 mm high and 1.6 mm wide). The depth of sharpness of the pictured area was sufficient to film all the bubbles, present in the filmed area, at picture frequencies of 2000 to 3000 frames per second. The measured bubble parameters were averaged, because of fluctuations. In order to cover the bubble behaviour in different stages, approximately 500 frames of the film for each experimental condition were used to obtain sufficiently accurate bubble parameters for calculating the efficiency of gas bubble evolution (cf. Section 5.4).
For the chlorine experiments, a solution of 4 M NaCl plus 0.1 M HCl was used as anolyte. A 1 M KOH solution has been used as catholyte for the hydrogen evolution and as anolyte for the oxygen evolution at 298 K. For

the hydrogen evolution at 353 K a 6.8 M NaOH has been used as catholyte. The solution flow circuit containing the counter-electrode compartment was generally filled with 10 M NaOH.

The choice of the electrolysis conditions was based on common industrial operation conditions of the chlor-alkali process.

The working electrode consisted of a nickel or platinum wire (diameter 0.5 mm) with or without a coating layer of RuO_2 or Co_3O_4. The length of the wire was about 3 mm.

5.3.2 Preparation of electrodes

5.3.2.1 Preparation of RuO_2-electrode [14]

The platinum-wire was placed during 10 minutes in concentrated caustic at 353 K and then in concentrated hydrochloric acid at 353 K. The wire was coated by dipping into a solution of 0.1 M $RuCl_3$ and 20 wt% HCl, then dried at 353 K and heated during 10 minutes at 723 K.

This procedure was repeated six times. Finally, the wire was heated for one hour at 723 K.

5.3.2.2 Preparation of Co_3O_4-electrode [15]

The platinum-wire was etched during 10 minutes in concentrated hydrochloric acid at 353 K, then dipped into a 0.5 M $Co(NO_3)_2$ solution, dried for about 1 minute at 353 K and heated for 3 to 5 minutes at 623 K. This procedure was repeated three times. Finally, the wire was heated for one hour at 623 K.

5.4 Results

5.4.1 Characteristics of departing chlorine, hydrogen and oxygen bubbles

Only part of the product formed during electrolysis is evolved as bubbles, the rest of the product is dissolved into the solution. The rate of the gas bubble evolution is proportional to the current density, i_b, being a fraction of the current density, i_g, used for the total gas production. The bubble behaviour can be characterized by bubble parameters, such as bubble radius, bubble cross-section, bubble volume

and bubble frequency.

Assuming that the bubbles formed during electrolysis are saturated with water vapor, the volume of the gas is calculated by:

$$V_g = V_{(g+H_2O)} \frac{[p(g+H_2O) - p(H_2O)]}{p(g+H_2O)} \tag{5.1}$$

where V_g = the volume of the gas (m^3), $V(g+H_2O)$ = the volume of gas (g) plus water vapor (m^3), $p(g+H_2O)$ = the sum of the partial pressures of gas and water vapor is supposed to be 101 kPa. The hydrostatic head was not taken into account in the gas volume calculation because its value was negligible.

The $p(H_2O)$ of different kinds of solution are given as a function of temperature in literature [16].

The values of characteristic quantities of attached-bubbles at the electrode surface fluctuate around a quasi-stationary state [17]. Due to variations in the nucleation properties of the electrode surface, the extent of the fluctuation depends, moreover, on electrode orientation, nature of the gas evolved and electrolytic conditions.

Similar phenomena are expected to occur with detached-bubbles. Moreover, the quasi-stationary state changes with increasing electrolysis time and, finally, becomes practically constant.

The values of the measured bubble parameters are averaged, because of their fluctuations. A common method for averaging is as follows: the bubble behaviour on a small surface is filmed during a certain period of time. To cover the bubble behaviour in different stages, an adequate number of frames of the film has to be used to obtain sufficiently accurate bubble parameters; then, the bubble parameters are averaged in time.

It has been found that about 500 frames of the film are required to obtain reliably averaged values of the bubble parameters, at a film speed of 3000 frames per second. At the beginning of filming, the camera is not running steadily: it requires some time before becoming stationary; therefore, the first thousand frames of the film are skipped. Additionally, for each set of electrolysis conditions a pre-electrolysis time of about 30 minutes is required to enable the electrolytic system to be stabilized.

From the experimental bubble radii we calculated:

$$R_{d,av} = \sum_{i=1}^{n} \frac{R_{d,i}}{n}, \qquad R_{s,d,av} = \frac{\sum_{i=1}^{n} \frac{R_{d,i}^3}{n}}{\sum_{i=1}^{n} \frac{R_{d,i}^2}{n}}, \qquad (5.2)$$

$$(R_d^2)_{av} = \sum_{i=1}^{n} \frac{R_{d,i}^2}{n} \text{ and } (R_d^3)_{av} = \sum_{i=1}^{n} \frac{R_{d,i}^3}{n} \qquad (5.3)$$

where $R_{d,av}$ = the average radius of detached-bubbles, $R_{d,i}$ = the radius of detached-bubble i, n = the number of bubbles, $R_{s,d,av}$ = the average Sauter radius of detached-bubbles, $(R_d^2)_{av}$ = the average of the square of the bubble radii, and $(R_d^3)_{av}$ = the average of the third power of the bubble radii.

In the formula of $R_{d,av}$, the contribution of the small bubbles dominates too much and that of the bigger bubbles too low. Therefore, it is preferable to use $R_{s,d,av}$.

5.4.1.1 Effect of current density

Fig. 5.2 shows the average Sauter radius of detached-bubbles, $R_{s,d,av}$, as a function of the current density, i_b, on a double logarithmic scale for chlorine and hydrogen evolution at two temperatures, and for oxygen evolution at only one temperature.

From Fig. 5.2 it follows that log $R_{s,d,av}$ for all three gases increases linearly with increasing log i_b, for i_b from about 0.01 to 5 kA m^{-2}. The experimental results showed that the average radius, $R_{d,av}$, the average square of radius, $(R_d^2)_{av}$, the average third power of radius, $(R_d^3)_{av}$, and the frequency of detached-bubbles, ω, as a function of current density, i_b, on a double logarithmic scale are linear too.

These linear relations can be expressed by:

$$R_{d,av} = a_1 \, i_b^{n_1}, \quad (R_d^2)_{av} = a_2 \, i_b^{n_2}, \quad (R_d^3)_{av} = a_3 \, i_b^{n_3}, \quad R_{s,d,av} = a_4 \, i_b^{n_4}$$

and

$$\omega = a_5 \, i_b^{n_5}. \qquad (5.4)$$

The constants a_1 to a_5 and n_1 to n_5 are tabulated in table 5.1.

Fig. 5.2 *Average Sauter bubble radius vs. the current density i_b on a double logarithmic scale for a hydrogen-evolving nickel electrode in 1 M KOH, at 298 K and a solution flow velocity of 0.12 m s^{-1}, and in 6.8 M NaOH, at 353 K and a solution flow of 0.05 m s^{-1}; evenso for an oxygen-evolving nickel electrode in 1 M KOH, at 298 K and a solution flow velocity of 0.12 m s^{-1}, and for a chlorine-evolving RuO$_2$/Pt electrode in 4 M NaCl + 0.1 M HCl, at 298 K and 353 K and a solution flow velocity of 0.05 m s^{-1}.*

Gas	T (K)	$v_{s,o}$ (m s^{-1})	Electrode material	Electrolyte	$a_1 \times 10^5$	n_1	$a_2 \times 10^9$	n_2	$a_3 \times 10^{13}$	n_3	$a_4 \times 10^5$	n_4	$a_5 \times 10^{-6}$	n_5
Cl$_2$	298	0.05	RuO$_2$/Pt	4M NaCl+0.1M HCl	7.2	0.17	6.0	0.46	5.3	0.60	9.4	0.19	57	0.38
Cl$_2$	353	0.05	RuO$_2$/Pt	4M NaCl+0.1M HCl	4.7	0.13	3.2	0.14	2.9	0.13	10.5	0.07	220	0.95
H$_2$	298	0.12	Ni	1M KOH	4.0	0.20	2.2	0.49	1.3	0.74	6.0	0.26	260	0.28
H$_2$	353	0.05	Ni	6.8 M NaOH	4.6	0.22	2.5	0.43	1.6	0.55	6.6	0.15	330	0.47
O$_2$	298	0.12	Ni	1 M KOH	4.8	0.24	2.7	0.50	1.5	0.63	5.7	0.21	180	0.41

Table 5.1 The values of empirical constants a_1 - a_5 and n_1 - n_5.

The detached-bubble frequency, ω, i.e. the number of detached-bubbles from the electrode per second and per m^2 electrode surface, for chlorine, hydrogen and oxygen is plotted versus the current density, i_b, on a

double logarithmic scale in Fig. 5.3. The parameters a_5 and n_5 depend strongly on both the nature of the gas evolved and the temperature.

5.4.1.2 Effect of solution flow velocity

The average Sauter radius, $R_{s,d,av}$, for chlorine, hydrogen and oxygen bubbles is plotted as a function of solution flow velocity, $v_{s,o}$, for a constant i_g in Fig. 5.4.
From Fig. 5.4, it can be concluded that in the solution flow velocity range from 0 to 0.2 m s^{-1} the $R_{s,d,av}$ for the three gases decreases linearly with increasing $v_{s,o}$ at 298 K and 353 K.
In Fig. 5.5, the detached–bubble frequency ω versus $v_{s,o}$ at constant i_g is given for hydrogen, chlorine and oxygen. The results obtained show that in the solution flow velocity range from 0 to 0.12 m s^{-1} the detached–bubble frequency for the three gases increases linearly with increasing solution flow velocity, at 298 K and 353 K.

5.4.1.3 Effect of temperature and electrode material

In Fig. 5.6 the logarithm of average Sauter radius, $R_{s,d,av}$, for the three gases is shown as a function of the reciprocal temperature. The dependence of $R_{s,d,av}$ on the reciprocal temperature can be represented by:

$$R_{s,d,av} = a_6 . 10^{\frac{n_6}{T}} \qquad (5.5)$$

The parameters a_6 and n_6 of the three gases are given in table 5.2.
The constants a_6 and n_6 depend on the solution flow velocity, the current density, the nature of the gas evolved, the electrode material and the electrolyte. The dependence of the detached–bubble frequency on the temperature for chlorine, hydrogen and oxygen is showed in Fig. 5.7. The curves show that, in the temperature range from 298 K to 353 K at constant i_g, the detached–bubble frequency for the three gases increases linearly with increasing temperature.
For only the chlorine experiment the temperature was extended to 363 K. In the temperature range from 353 K to 363 K the detached–bubble frequency for chlorine increases rapidly with increasing temperature, probably due to water vapour formation.
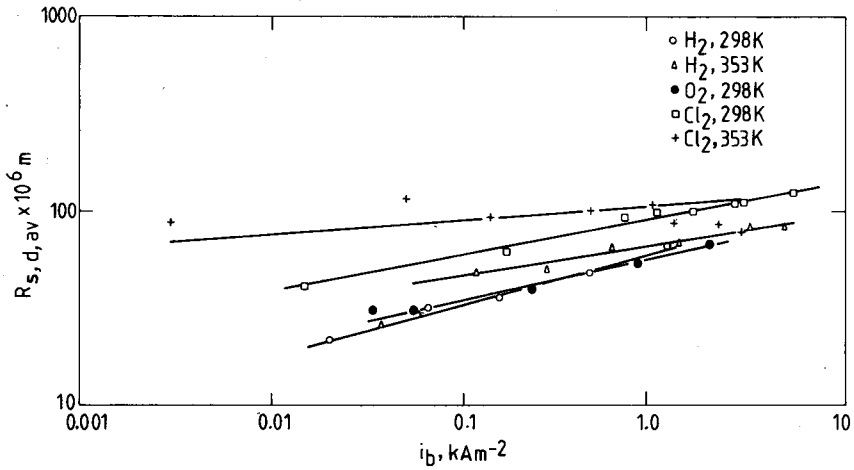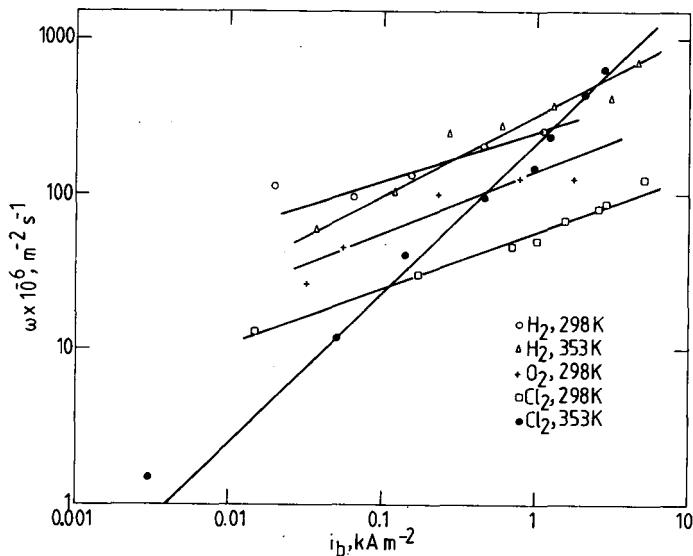
Fig. 5.3 *Detached-bubble frequency vs. the current density i_b on a double logarithmic scale for a hydrogen-evolving nickel electrode in 1 M KOH, at 298 K and a solution flow velocity of 0.12 m s^{-1}, and in 6.8 M NaOH, at 353 K and a solution flow of 0.12 m s^{-1}; evenso for an oxygen-evolving nickel electrode in 1 M KOH, at 298 K and a solution flow velocity of 0.12 m s^{-1}, and for a chlorine-evolving RuO$_2$/Pt electrode in 4 M NaCl + 0.1 M HCl, at 298 K and 353 K and a solution flow velocity of 0.05 m s^{-1}.*
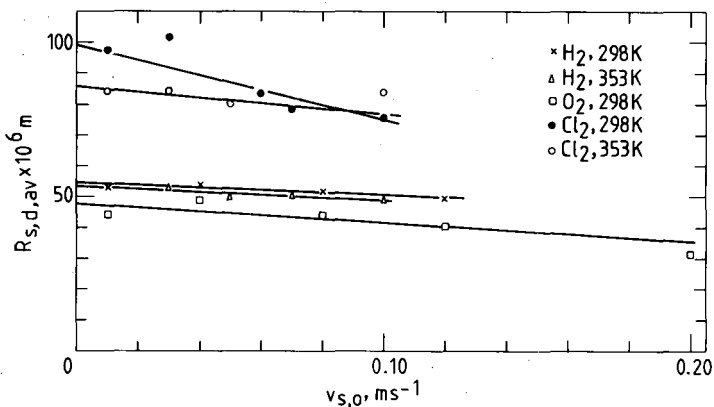
Fig. 5.4 *Average Sauter radius of detached-bubbles versus the solution flow velocity for a hydrogen-evolving nickel electrode in 1 M KOH, at 298 K and 1 kA m^{-2}, and in 6.8 M NaOH, at 353 K and 1 kA m^{-2}; evenso for an oxygen-evolving nickel electrode, at 298 K and 1 kA m^{-2}, and for a chlorine-evolving RuO$_2$/Pt electrode in 4 M NaCl + 0.1 M NaCl at 298 K and 353 K, respectively, at 2 kA m^{-2} and 4 kA m^{-2}.*

– 53 –
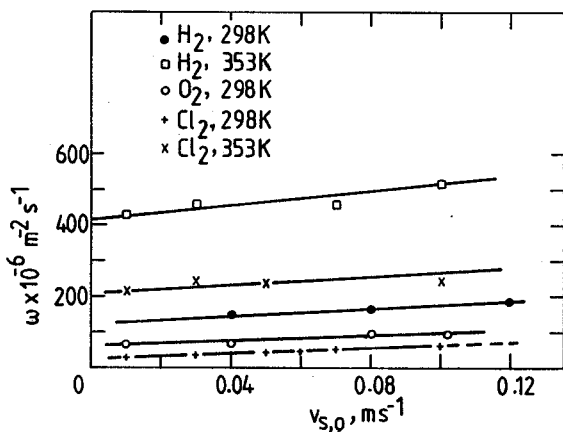
Fig. 5.5 *Detached-bubble frequency versus the solution flow velocity of an oxygen-evolving nickel electrode in 1 M KOH, at 298 K and 1 kA m^{-2}; evenso for an chlorine-evolving RuO$_2$/Pt electrode in 4 M NaCl + 0.1 m HCL, at 298 K and 353 K, respectively, at 2 kA m^{-2} and 4 kA m^{-2}, and for a hydrogen-evolving nickel electrode in 1 M KOH, at 298 K and 1 kA m^{-2} and in 6.8 M NaOH, at 353 K and 1 kA m^{-2}.*
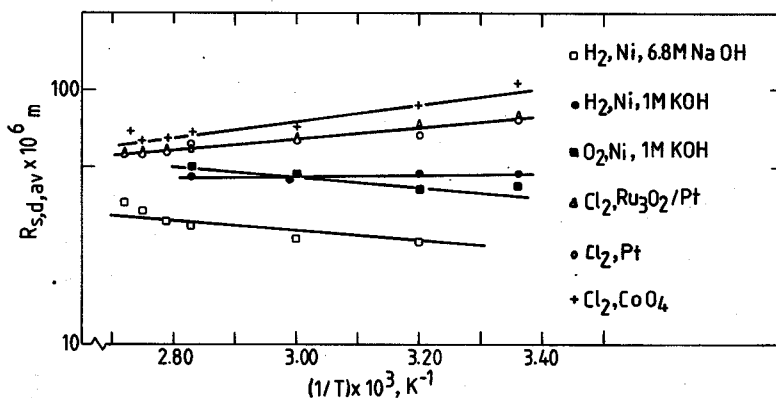
Fig. 5.6 *Average Sauter radius versus reciprocal temperature on a single logarithmic scale for a hydrogen-evolving nickel electrode in 1 M KOH, at 1 kA m^{-2} and a solution flow velocity of 0.12 m s^{-1}, and in 6.8 M NaOH, at 0.5 kA m^{-2} and a solution flow velocity of 0.05 m s^{-1}; evenso for a n oxygen-evolving nickel electrode in 1 M KOH, at 1 kA m^{-2} and a solution flow velocity of 0.12 m s^{-1}, and for a chlorine-evolving electrode of RuO$_2$/Pt, Pt and Co$_3$O$_4$ in 4 M NaCl + 0.1 M HCl, at 2 kA m^{-2} and a solution flow velocity of 0.05 m s^{-1}.*
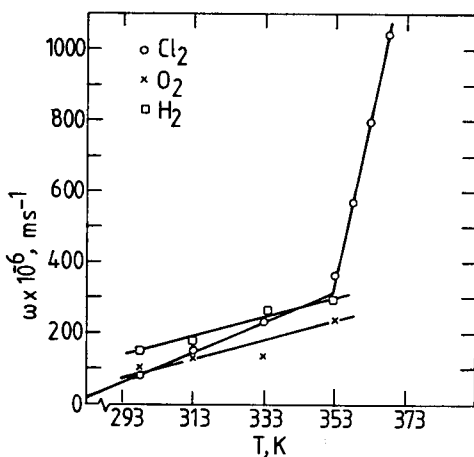
Fig. 5.7 *Detached-bubble frequency versus the temperature for a hydrogen- evolving nickel electrode in 1 M KOH at 1 kA m^{-2} and a solution flow velocity of 0.12 m s^{-1}; evenso for an oxygen-evolving nickel electrode in 1 M KOH, at 1 kA m^{-2} and a solution flow velocity of 0.12 m s^{-1}, and for a chlorine-evolving RuO$_2$/Pt electrode in 4 m NaCl + 0.1 M HCl at 2 kA m^{-2} and a solution flow velocity of 0.05 m s^{-1}.*

Gas	i_g (kA m^{-2})	$v_{s,o}$ (m s^{-1})	Electrode material	Electrolyte*	$a_6 \cdot 10^6$	n_6
Cl$_2$	2	0.05	RuO$_2$/Pt	4M NaCl+0.1M HCl	13.2	229
Cl$_2$	2	0.05	Pt	4M NaCl+0.1M HCl	13.2	229
Cl$_2$	2	0.05	Co$_3$O$_4$	4M NaCl+0.1M HCl	9.8	295
H$_2$	0.5	0.05	Ni	6.8 M NaOH	112	−200
H$_2$	1	0.12	Ni	1 M KOH	34.7	40
O$_2$	1	0.12	Ni	1 M KOH	15.9	−182

* Saturated with Cl$_2$, H$_2$ or O$_2$.

Table 5.2 The values of empirical constants a$_6$ and n$_6$.

5.4.2 Efficiency of bubble evolution

The efficiency of bubble evolution is defined by:

$$\eta_b = \frac{v_{g,b}}{v_{g,o}} \qquad\qquad (5.6)$$

where $v_{g,o} = \frac{i_g}{nF} \frac{T}{298} V_M$ (theoretical gas production rate, when the gas

formed is completely taken up by bubbles, V_M = the volume of one mol gas
at 298 K and a pressure of 101 kPa = 24.5×10^{-3} m^3 mol^{-1}, i_g = the
current density used for the total gas production in kA m^{-2}, n = the
number of electrons, involved in the reaction to form one molecule of
Cl_2, H_2 or O_2) and $v_{g,b}$ = the experimental gas bubble production rate
corrected for the effect of vapour.

5.4.2.1 Effect of current density

The efficiency of gas bubble evolution versus the current density for
oxygen and hydrogen evolution is plotted in Fig. 5.8 and for chlorine in
Fig. 5.9. The results obtained show that the efficiency of gas bubble
evolution increases asymptotically with increasing current density i_g.
Hydrogen evolution has the highest η_b and chlorine evolution the lowest.
In Fig. 5.10, $\eta_b/(1-\eta_b)$ is plotted as a function of the current density,
i_b, on a double logarithmic scale for chlorine and hydrogen evolution at
298 K and 353 K, and for oxygen evolution at 298 K.
Fig. 5.10 shows that log $\eta_b/(1-\eta_b)$ for all three gases increases linearly
with increasing log i_b in the i_b range from 0.02 to 5 kA m^{-2}.
These linear relations are expressed by:

$$\frac{\eta_b}{1-\eta_b} = a_7 i_b^{n_7} \qquad\qquad (5.7)$$

The parameters a_7 and n_7 of the three gases are given in table 5.3, where
i_b is given in kA m^{-2}.
The constant a_7 depends on the temperature, the solution flow velocity
and the nature of the gas evolved, the electrode material and the
electrolyte. Here, the constant n_7 is 0.39.
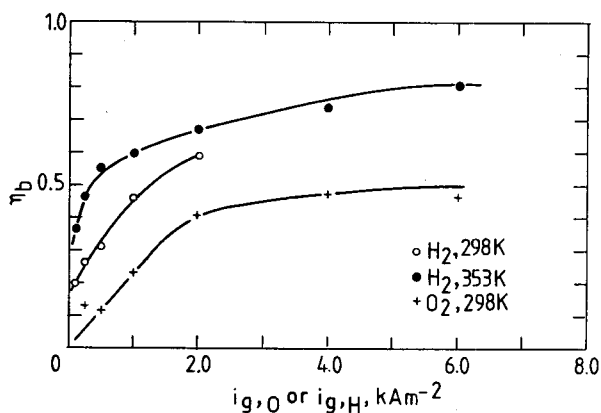
Fig. 5.8 *Efficiency of gas bubble evolution as a function of current density for hydrogen evolution on a nickel electrode in 1 M KOH, at 298 K and a solution flow velocity of 0.12 m s⁻¹, and in 6.8 M NaOH, at 353 K and a solution flow velocity of 0.05 m s⁻¹; evenso for oxygen- evolution on a nickel electrode in 1 M KOH at 298 K and a solution flow velocity of 0.12 m s⁻¹.*
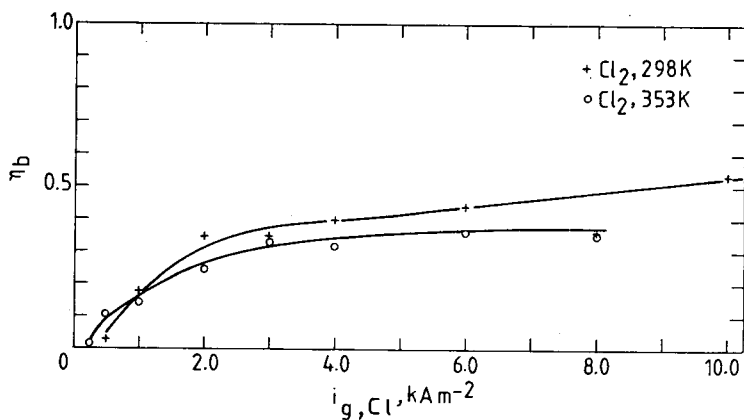
Fig. 5.9 *Efficiency of gas bubble evolution as a function of current density for chlorine evolution on a RuO₂/Pt electrode in 4 M NaCl + 0.1 M HCl, at 298 K and 353 K and a solution flow velocity of 0.05 m s⁻¹.*
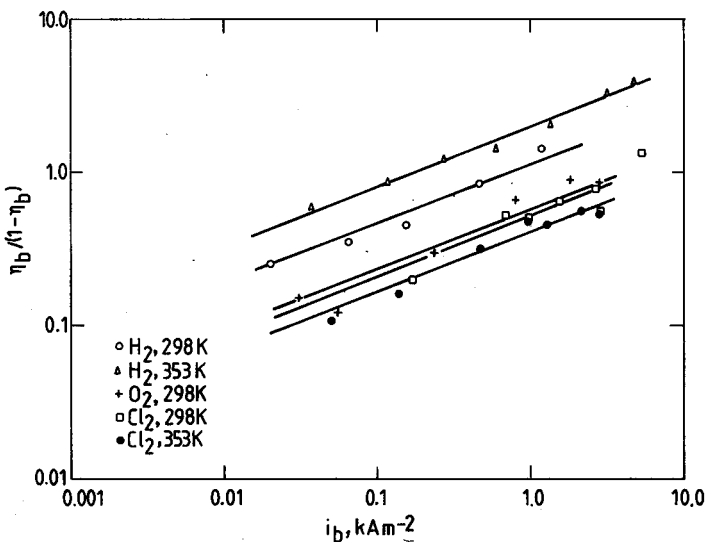
Fig. 5.10 $\eta_b/(1-\eta_b)$ plotted versus the current density, i_b, on a double logarithmic scale for a hydrogen-evolving nickel electrode in 1 M KOH, at a 298 K and a solution flow velocity of 0.12 m s^{-1}, and in 6.8 M NaOH, at 353 K and a solution flow of 0.05 m s^{-1}; evenso for an oxygen-evolving nickel electrode in 1 M KOH, at 298 K and a solution flow velocity of 0.12 m s^{-1}, and for a chlorine-evolving RuO$_2$/Pt electrode in 4 M NaCl + 0.1 M HCl, at 298 K and 353 K and a solution flow velocity of 0.05 m s^{-1}.

Gas	T (K)	$v_{s,o}$ (m s^{-1})	Electrode material	Electrolyte	a_7	n_7
Cl$_2$	298	0.05	RuO$_2$/Pt	4M NaCl+0.1M HCl	0.5	0.39
Cl$_2$	353	0.05	RuO$_2$/Pt	4M NaCl+0.1M HCl	0.4	0.39
H$_2$	353	0.05	Ni	6.8 M NaOH	2.0	0.39
H$_2$	298	0.12	Ni	1 M KOH	1.1	0.39
O$_2$	298	0.12	Ni	1 M KOH	0.6	0.39

Table 5.3 The values of empirical constants a_7 and n_7.

5.4.2.2 Effect of solution flow velocity

Fig. 5.11 shows $\eta_b/(1-\eta_b)$ for the three gases versus the solution flow velocity at constant i_g. From Fig. 5.11 it follows that $\eta_b/(1-\eta_b)$ for chlorine, hydrogen and oxygen decreases slightly with increasing solution flow velocity.

5.4.2.3 Effect of temperature and electrode material

In Fig. 5.12 the efficiency of gas bubble evolution for chlorine, hydrogen and oxygen is plotted as a function of temperature.
The curves show that in the temperature range from 298 K to 368 K the $\eta_{b,H}$ for hydrogen evolution on a nickel electrode in 1 M KOH solution at 1 kA m^{-2} and $v_s = 0.12$ m s^{-1} is independent of T, while $\eta_{b,H}$ for hydrogen evolution on a nickel electrode in 6.8 M NaOH solution at 0.5 kA m^{-2} and $v_s = 0.05$ m s^{-1} increases slightly with increasing temperature.
$\eta_{b,O}$, for oxygen evolution on a nickel electrode in 1 M KOH solution at 1 kA m^{-2} and $v_s = 0.12$ m s^{-1} increases strongly with increasing temperature.
Fig. 5.13 shows the efficiency of gas bubble evolution for chlorine as a function of temperature for three different electrode materials, viz.: RuO_2/Pt, Pt and Co_3O_4 electrodes.
The curves show that RuO_2/Pt electrode has the highest efficiency of gas bubble evolution and Co_3O_4 electrode the lowest.
The η_b of all three types electrodes increases with increasing temperature till it reaches a maximum value at about 348 K and then decreases by increasing temperature.

5.5 Discussion

5.5.1 The applicability of models for slow bubble growth to electrolysis bubbles

During the experiment bubbles rise in the space filmed just above the top of the working electrode: the number of bubbles did not change, i.e.no coalescence occurred in the space just above the working electrode. Since the electrode is very short (about 3 mm), it can be assumed that during the period between the detachment of a bubble and the filming of this
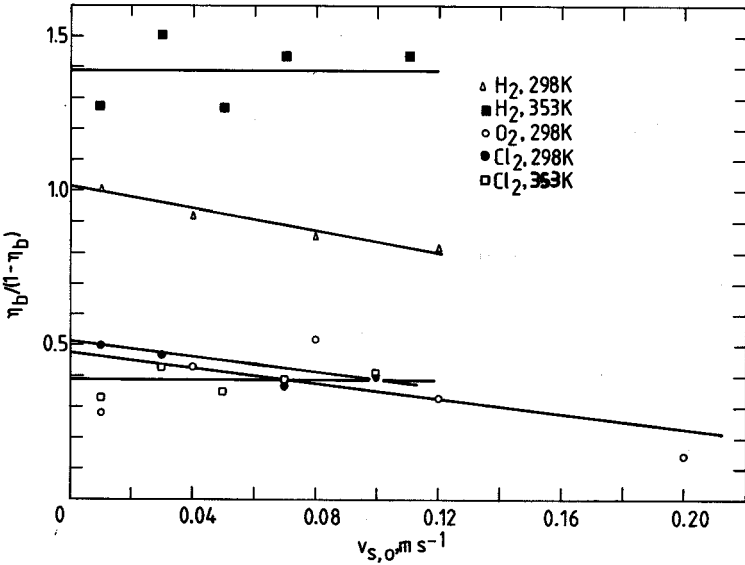
Fig. 5.11 $\eta_\beta/(1-\eta_\beta)$ *as a function of solution flow velocity for a hydrogen-evolving nickel electrode in 1 M KOH, at 1 kA m^{-2}, and 298 K and in 6.8 M NaOH, at 1 kA m^{-2} and 353 K; evenso for an oxygen-evolving nickel electrode in 1 M KOH, at 1 kA m^{-2} and 298 K, and for a chlorine-evolving RuO$_2$/Pt electrode in 4 M NaCl + 0.1 M HCl, at 2 kA m^{-2} and 4 kA m^{-2}, respectively, at 298 K and 353 K.*
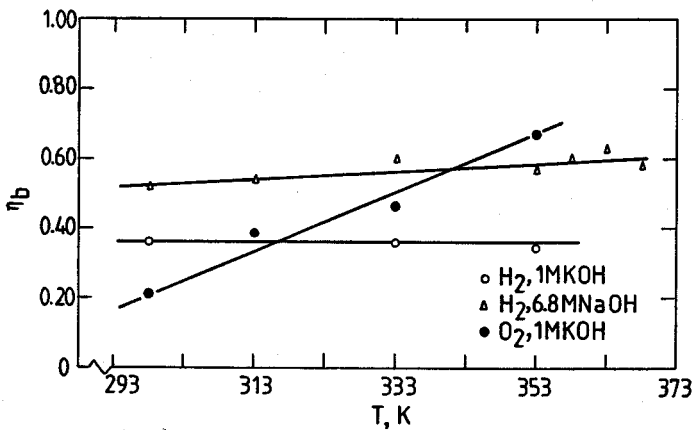
Fig. 5.12 Efficiency of gas bubble evolution as a function of temperature for a hydrogen-evolving nickel electrode in 1 M KOH, at 1 kA m^{-2} and a solution flow velocity of 0.12 m s^{-1}, and in 6.8 m NaOH at 0.5 kA m^{-2} and a solution flow velocity of 0.05 m s^{-1}; evenso and for an oxygen-evolving nickel electrode in 1 M KOH, at 1 kA m^{-2} and a solution flow velocity of 0.12 m s^{-1}.
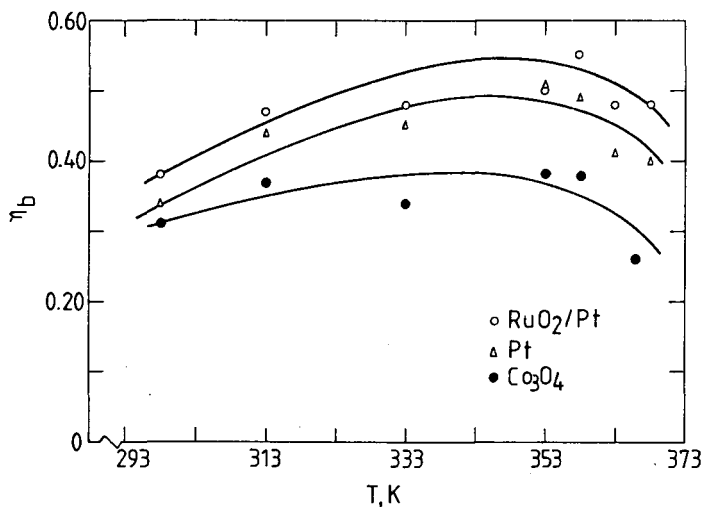
Fig. 5.13 Efficiency of gas bubble evolution as a function of temperature for a chlorine-evolving electrode of RuO₂/Pt, Pt and Co₃O₄ in 4 M NaCl + 0.1 M HCl saturated with Cl₂, at 2 kA m⁻² and a solution flow velocity of 0.05 m s⁻¹.

bubble, coalescence of detaching rising bubble is negligible.

This result agrees with the literature, i.e. coalescence of hydrogen bubbles in alkaline solution and of chlorine bubbles in acidic chlorine solution occurs only to a limited extent [3,18]. Probably the growth of a bubble can be neglected after detachment until the moment of filming, since no bubble growth rate was detected in the observed space (picture height 1.70 mm). It can therefore be concluded that pictured bubbles have almost the same size as bubbles departing from the electrode surface.

The applicability of models for slow bubble growth to electrolysis bubbles will be discussed here.

The two pertinent results for cavity bubbles are:

$$R_c = 2\sigma/K\Delta c^\sigma = 2\sigma/\Delta P \qquad\qquad (3.3)$$

and

$$R_{d.\alpha} = [3\sigma R_c/2g(\rho_1-\rho_g)]^{1/3} \qquad\qquad (3.7)$$

These results can be combined to give:

$$R_{d.\alpha} = [3\sigma^2/g(\rho_1-\rho_g)\Delta P]^{1/3} \qquad\qquad (3.28)$$

A first comparison of Eq. 3.28 with the bubble sizes and supersaturation levels observed suggested that there is broad agreement. Thus, ignoring details of electrode geometry and surface treatment in the first analysis, Fig. 4.3 shows that for large current densities ΔP_{Cl} is 24 x 10^5 N m^{-2}, yielding $R_{d,Cl} = 87$ µm if σ is taken as 7.2 x 10^{-2} N m^{-1}. This agrees with the order of magnitude found in the experiments: both with the plane vertical electrode (cf. Table 3.1) and with the wire one (cf. Table 5.4). Furthermore, the greater values of ΔP for oxygen and chlorine (cf. Fig. 4.3) agree with the observation that the bubbles are smaller in these cases (taking $\Delta P_O = 45$ x 10^5 N m^{-2} and $\Delta P_H = 80$ x 10^5 N m^{-2} (cf. Fig. 4.3), Eq. 3.28 yields $R_{d,O} = 71$ µm and $R_{d,H} = 58$ µm (cf. Table 5.4)). On the other hand, the sizes of the active cavities implied by these values of ΔP are much smaller than those typical of boiling on metal surfaces, as indicated by the fact that for water at atmospheric pressure a value of ΔP of, say, 50 x 10^5 N m^{-2}, would require a superheat of over 150°C (i.e. a water temperature adjacent to the heated surface of over 250°C).

The corresponding value of R_c is found from Eq. 3.3 to be 300 Å. The fact that larger cavities (of micron size) do not appear to be active may be due to the surfaces concerned being very smooth, but while this is conceivable in the sputtered case it seems unlike in the case of the wire (N.B. in the latter case it could, in fact, be checked by inducing boiling on the wire and observing the size of the resulting bubbles).

It has been found, that in alkaline solution, hydrogen bubbles slip over the electrode surface more frequently than oxygen bubbles [19].

Unlike a cavity bubble, which by definition remains anchored to the cavity on which it originates, a spreading bubble can drift over the surface (an example is provided by CO_2 bubbles in Seven Up on a plastic beaker).

The observation that hydrogen bubbles appear to do this is thus consistent with the possibility that they are spreading bubbles but remains questionable for two reasons:

- as noted above the bubble size is consistent with cavity bubbles, given the very small cavities implied by the degree of supersaturation

observed;

- the value of the contact angle required to explain the size observed is of the order of one degree (cf. Eq. 3.8); in practice contact-angle hysteresis always requires the actual angle to fall several degrees below this value before the contact line begins to receed; in the present case this is clearly impossible since the angle would then have to become negative;
- such tiny contact angles are not consistent with the statement that the contact angle increases with current density since the contact angle of aqueous media on metals for zero current density is typicaly around 70 deg.

Experimentally it was found that the detached-bubble radius, $R_{s,d}$, increases with increasing current density (cf. Fig. 5.2). The opposite trend has been observed with a plane vertical electrode (cf. Table 3.1). This difference cannot be explained with the existing theory. The same is true as the fact that the active cavity (and hence bubble) size appears to depend on the electrolytic reaction taking place at the surface-cavities, being consistently smaller for hydrogen and oxygen than for chlorine (cf. Table 5.4).

This and other facts strongly suggest that electric and interfacial phenomenon interact - as suggested also by the statement [9] that the contact angle rises with increasing current density. (Unfortunately this would not explain the wetting and resulting deactivation of large cavities, which should be promoted by contact angle reduction). It is then conceivable that the surface tension, too, is a function of the current density.

It can be concluded that while the main tendencies observed appear consistent with the mechanics of cavity bubbles there are many anomalies which probably have their origin in combined interfacial and electrical effects. A satisfactory description of these effects does not appear to exist at present, nor even to have been attempted.

It has been found, that under the condition $i_g = 2$ kA m^{-2}, $T = 298$ K and $v_{s,o} = 0.12$ m s^{-1}, $R_{d,H}$ is approximately the same as $R_{d,O}$ (42×10^{-6} m), and significantly smaller than $R_{d,Cl}$ (56×10^{-6} m).

Still more time is required to obtain a solution free from hydrogen than for oxygen and chlorine bubbles.

This means that the separation of bubbles from a solution is not only determined by departure bubble radius, but also by the coalescence

Gas	H_2		O_2		Cl_2	
$v_{g,b} \times 10^4$ m s^{-1}	0.126	1.26	0.126	1.26	0.126	1.26
i_b (kA m^{-2})	0.1	1.0	0.2	2.0	0.1	1.0
$R_{d,av}$ (m)	25×10^{-6}	40×10^{-6}	31×10^{-6}	55×10^{-6}	36×10^{-6}	59×10^{-6}
$(R^2_d)_{av}$ (m^2)	7×10^{-10}	22×10^{-10}	12×10^{-10}	38×10^{-10}	14×10^{-10}	41×10^{-10}
$(R^3_d)_{av}$ (m^3)	2.3×10^{-6}	13×10^{-14}	4.7×10^{-14}	26×10^{-14}	7×10^{-14}	29×10^{-10}
$R_{s,d,av}$ (m)	32×10^{-6}	60×10^{-6}	40×10^{-6}	67×10^{-6}	51×10^{-6}	79×10^{-6}
ω (m^{-2} s^{-1})	120×10^6	260×10^6	74×10^6	180×10^6	36×10^6	84×10^6
η_b	0.30	0.56	0.22	0.43	0.13	0.28

Table 5.4 Bubble parameters for hydrogen and oxygen evolution at a Ni electrode in 1 M KOH, evenso for chlorine evolution at a RuO$_2$/Pt electrode in 4 M NaCl + 0.1 M HCl at two volumetric rates of bubble evolution, viz. $v_{g,b} = 0.126 \times 10^{-4}$ and 1.26×10^{-4} m s^{-1}, at T = 298 K and $v_{s,o} = 0.12$ m s^{-1}.

Gas	H_2	O_2	Cl_2
diffusion coefficient m^2/s [20,22]	3.0×10^{-9}	1.59×10^{-9}	1.22×10^{-9}
solubility concentration mol/m^3 [20-22]	0.52	0.89	22
i_g kA/m^2	1.8	4.7	3.6
i_b kA/m^2	1.0	2.0	1.0
η_b	0.56	0.43	0.28
s degree of screening [19]	0.40	0.40	0.80
d (mm^{-2}) bubble polulation density [19]	1500	250	19
R_z (μm) attached bubble radius [19]	8	17	110
$2\pi dR_a$ (mm^{-1}) total circumference of the cross-section of bubbles	76	27	13

Table 5.5 Parameters for hydrogen-, and oxygen- and chlorine gas-evolving electrodes at a volumetric rate of bubble evolution of 1.26×10^{-4} m/s, a solution flow velocity of 0.12 m/s and at 298 K.

behaviour of bubbles.

5.5.2 Efficiency of bubble evolution

The results obtained indicate that the size of a departure bubble remains almost constant during its rise in the film region (cf. Section 5.5.1). So it follows that the efficiency of bubble evolution, η_b, determined from the pictures taken just above the top of the working electrode equals that near the surface of the gas-evolving electrode.
The theoretically calculated η_b by Vogt [10] is, however, much lower. Since the solution at the inlet of the cell is saturated, the solution near the electrode surface becomes supersaturated by gas evolution.
The supersaturation decreases with increasing distance from the gas-evolving electrode, due to diffusion, convection and gas absorption by bubbles.
Table 5.4 shows that the efficiency of bubble evolution, η_b, decreases in the sequence H_2, O_2 and Cl_2 ($\eta_H > \eta_O > \eta_{Cl}$). No exact or even approximate theory is available to explain this phenomenon up till now.
Bubble parameters in literature, that are relevant for the explanation of the results obtained are tabulated in Table 5.5.
The great difference in η_b for H_2 and O_2 (cf. Table 5.5) cannot be explained by the relatively slight differences in diffusion coefficient and solubilities. Additionally, solubility has no influence on η_b, because the solution at the inlet of the cell is already saturated with the gas evolved. A more appropriate approach is to compare the observed phenomenon with the gas transport to an electrode in a fuel cell.
It is well known that the length of the three-phase boundary (electrode-solution-gas) mainly determines the transport of gas to the electrode. Evidently, the total circumference of the cross-section of bubbles (cf. Table 5.5) attached to the electrode determines η_b.
Fig. 5.14 shows that only part of the gas formed during electrolysis is evolved as bubbles at the electrode, the rest of the gas is dissolved into the solution.
The transport of dissolved gas formed at the electrode to the attached-bubble increases with increasing total circumference of the cross-section of bubbles attached to the electrode. Hence, η_b increases with increasing $2 \pi d R_a$.
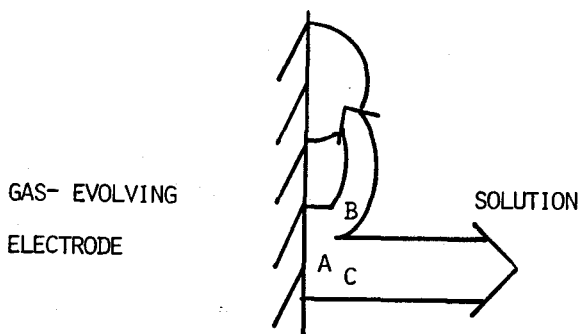
Fig. 5.14 Total flow of dissolved gas formed at the electrode, A, flow of dissolved gas to the attached-bubble, B, and flow of dissolved gas into the bulk, C.

5.6 References

1   L.J.J. Janssen and E. Barendrecht, Electrochim. Acta 30, (1985) 683

2   N. Ibl, E. Adam, J. Venczel and E. Schalok, Chem. Ing. Tech. 43 (1971) 202

3   L.J.J. Janssen, E. Barendrecht and S.J.D. van Stralen, 36th ISE-meeting, Salamanca, Spain, September 23-28, 1985, 4020-4022

4   S. Shibata, Electrochim. Acta 23 (1978) 619

5   A.K. Chesters in: S.J.D. van Stralen and R. Cole, Boiling Phenomena, chapter 26, Hemisphere Publishing Corporation, Washington 1, (1979)

6   S.J.D. van Stralen in: S.J.D. van Stralen and R. Cole, Boiling Phenomena, Hemisphere Publishing Corporation, Washington 1, 1979

7   N.P. Brandon and G.H. Kelsall, J. Appl. Electrochem. 5 (1984) 475

8   A. Coehn, Z. Electrochem. 29 (1923)

9   B. Kabanov and A. Frumkin, Z. Chem. 165 (1933) 433-452

10 H. Vogt, Ext. Abstracts 34th ISE-meeting, Erlangen (1983) 413

11 S.J.D. van Stralen, R. de Jonge and H. Verhaart in: S.J.D. van Stralen and R. Cole, Boiling Phenomena, Hemisphere Publishing Corporation, Washington 1, (1979) 413

12 P.J. Sides and C.W. Tobias, J. Electrochem. Soc. 127 (1980) 288

13 J. Dukovic and C.W. Tobias, Proc. Electrochem. Soc. 1986 (86-12) 122

14 S. Trasatti, Electrodes of conductive metallic oxides, part A, Elsevier Publishing Company, Amsterdam, Oxford, New York (1980), 315

15 V.V. Shalaginov, D.M. Shub, N.V. Kozlova and V.N. Lomova, Effect of

conditions of preparation on anodic behaviour of Ti/Co_3O_4 electrodes in chlorine solution, Elektrokhimiya $\underline{19}$ (1983) 537–541

16 C.J. West, International Critical Tables Vol. III, 370, McGraw–Hill, New York, London (1933)

17 C.W.M.P. Sillen, Thesis, Eindhoven University of Technology, 1983

18 L.J.J. Janssen, Electrochim. Acta $\underline{23}$ (1978) 81

19 L.J.J. Janssen, C.W.M.P. Sillen, E. Barendrecht and S.J.D. van Stralen, Electrochim. Acta $\underline{29}$ (1984) 633

20 L.J.J. Janssen and J.G. Hoogland, Electrochim. Acta. $\underline{15}$ (1970) 1013

21 A.M. Yatkoviski and N.A. Fedonton, R.J. Phys. Chem. $\underline{43}$ (1969) 575

22 F.T.B.J. van den Brink, Thesis, Eindhoven University of Technology (1981)

Chapter 6

Gas void fraction distribution, specific
ohmic resistance and current density distribution
in a gas-evolving electrolysis cell

6.1 Introduction

Up to now, the gas void fraction (i.e. the fraction of the total solution volume that is occupied by the gas bubbles) and the bubble distribution in a vertical two flat-plates electrolytic cell were studied by many investigators. However, they mostly focussed their attention on the effect of gas bubbles on the current density distribution and the ohmic resistance in the electrolyzer.
The very important effect of gas bubbles on the electrode overpotential was practically neglected (cf. Chapter 9).
In Section 6.2, a short literature overview is given. A new experimental technique to determine the gas void fraction in a semi-industrial cell (50 cm high) is described in Section 6.3. In Section 6.4, the results obtained are presented. The discussion of these results is given in Section 6.5.

6.2 Literature review

6.2.1 Gas void fraction distribution

The gas void fraction in a vertical flat-plate-electrode cell increases with increasing current density and increasing cell height. Consequently, the current density and specific ohmic resistance of the electrolyte decreases, respectively, increases with increasing height [1-4].
A number of publications reported a higher gas void fraction in a layer near the electrode [1,2,6].
Experimentally, it was found that each gas bubble-electrolyte mixture seems to have its own limiting gas void fraction [5]. This phenomenon can be explained at an acceptable manner by the recently developed coalescence barrier model [5].

6.2.2 Specific ohmic resistance of dispersions

In the discussion of Section 6.5, a selection has been made in the many existing models concerning the relation between the volume fraction, f, and the specific ohmic resistance, ρ, of the dispersion, whereby the dispersed particles are non-conductors.
Maxwell found [7]:

$$\rho/\rho_p = (1 + \tfrac{1}{2}f)/(1-f) \qquad\qquad (6.1)$$

where ρ_p = the specific ohmic resistance of the pure bulk solution.
The derivation was based on the following assumptions:
- random arrangements of uniform spheres;
- no electrical field interactions between spheres;
- the average distance between spheres is large with respect to the sphere radius.

Maxwell's equation has been derived for a range of volume fractions in diluted heterogeneous media up to f = 0.1, but many investigators had experienced that this equation is also valid for more concentrated dispersions [8-10].
Rayleigh [11,12,13] obtained for low volume fractions:

$$\rho/\rho_p = (1 + f)/(1-f) \qquad\qquad (6.2)$$

with the assumptions:
- of ordered arrangements of infinitely long, parallel cylinders in a square array;
- that the electrical field is perpendicular to the cylinder axes;
- that higher order electrical interactions are excluded.

Eq. 6.2 is only valid for low values of f, because the higher order terms of f have been neglected.
For ordered arrangements of monosized spheres at low gas void fraction, f, in a cubic array of spheres, he found Eq. 6.1 plus terms of the order of $f^{1/3}$ and higher [11] to be valid.
Bruggeman found [14]:

$$\rho/\rho_p = (1-f)^{-3/2} \qquad\qquad (6.3)$$

with the assumptions:
- of random arrangements of a broad range of multisized spheres;

- that by introducing a relatively large sphere into a dilute dispersion of smaller spheres, the electrical field interactions of these small spheres around the large sphere can be ignored; due to this fact he treated the surroundings of the large sphere as a continuum, having a bulk conductivity;
- that f is small.

The experimental results obtained by La Rue and Tobias [15] on suspension of glass beads, in a broad range of particle sizes, indicated that Bruggeman's equation is quite satisfactory.

It has been shown [16] that Bruggeman's equation is useful to determine the ohmic resistance of a solution layer containing gas bubbles of different sizes with each bubble adhering to the electrode surface. Many semi-empirical and empirical equations have been developed for more concentrated dispersions for non-conducting spheres. Mashovet [17], for example found: $\rho_p/\rho = 1 - 1.78 \ f + f^2$ (6.4)

As at f = 1, ρ_p/ρ does not approach zero, Eq. (6.4) is only valid up to f $\simeq$ 0.7.

6.2.3 Specific ohmic resistance in a gas-evolving electrolysis cell

Many models have been developed to correlate the gas void fraction, f, and the specific ohmic resistance, ρ, of a bubble-electrolyte mixture between two gas-evolving vertical flat-plate electrodes.

Rousar et al. [18,19] derived an equation for the relative resistance, R/R_p, for a bubble-electrolyte mixture as a function of the volumetric gas production rate and solution flow rate for monopolar and bipolar flat-plate electrolyzers under forced flow conditions, introducing some simplifications (e.g. no slip) and using the modified Maxwell's equation. They obtained:

$$R/R_p = 1 + 1.5 \ V_{g,o}/V_{s,o}$$ (6.5)

where R = the resistance of the bubble-electrolyte mixture, R_p = the resistance of the pure electrolyte, $V_{g,o}$ = the volumetric gas production rate and $V_{s,o}$ = the volumetric liquid-flow rate.

Hine et al. [20] developed an empirical equation for the bubble effect on the ohmic potential drop in a vertical rectangular cell with stainless

steel flat-plate electrodes evolving hydrogen bubbles under forced convection.
They found:

$$R/R_p = K_1 \; (\frac{2f}{1-f})^\alpha \; (\frac{d_{wm}}{w})^\beta \qquad\qquad (6.6)$$

where K_1 = an empirical coefficient, f = the gas void fraction, α = 0.12, β = -0.65, d_{wm} = the distance between working electrode and membrane and w = the width of the electrode.

Vogt [21] suggested, that the accumulated bubbles near the electrodes must have a great impact on the ohmic resistance of the electrolysis cell. In his hydrodynamic model he divided the inter-electrode gap in two different layers (cf. Fig. 6.1):

● a bubble-rich stagnant layer near the electrodes with thicknesses, δ_a and δ_c, which are equal the detached-bubble diameter; the gas void fraction in these two stagnant layers was supposed to be 0.6-0.7;

● a flowing bubble-electrolyte layer, next to both stagnant layers, having a thickness of $(d-\delta_a-\delta_c)$ and a uniform bubble distribution over the entire sectional area with a gas void fraction less than that in the stagnant layers.

The bubbles evolved at the electrodes penetrate from the stagnant layers into the flowing bubble-electrolyte layer. He obtained:

$$R/R_p = 0.4 \; (1-Y) \frac{V_{g,o}}{V_{s,o}} \; [(1 + \frac{V_{g,o}}{V_{s,o}})^{2.5} - 1] + YQ \qquad\qquad (6.7)$$

where $Y = (\delta_a + \delta_c)/d$ and Q = the relative resistance of the bubble layer obtained from Bruggeman's equation. Assuming Y = 0.01 and Q = 5, he claimed that this model agrees well with the experimental results obtained by Hine and Murakami [22]. However, older experimental results of Hine et al. [20] could not be explained properly. Hine et al. [20] were the first who proposed the variation of gas void fraction in the direction perpendicular to the electrode surface.

Sillen [1] came with about the same idea as Vogt. He divided the electrode-diaphragm section in three parts (cf. Fig. 6.2):

● the first sublayer consists of attached-bubbles with thickness equal
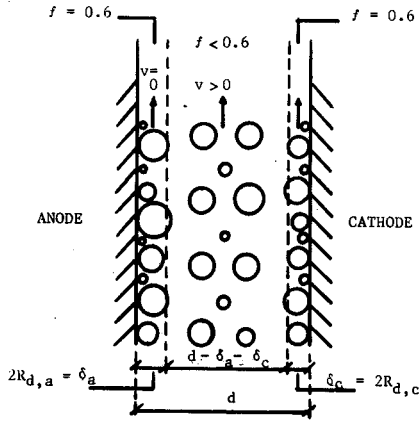
Fig. 6.1 Two-phase flow, δ_a = the thickness of the stagnant bubble layer at the anode, δ_c = the thickness of the stagnant bubble layer at the cathode, d = the distance between the electrodes, $R_{d,a}$ = the average detached-bubble radius evolved at the anode, $R_{d,c}$ = the average detached-bubble radius evolved at the cathode, v = the bubble-electrolyte flow velocity and f = gas void fraction.
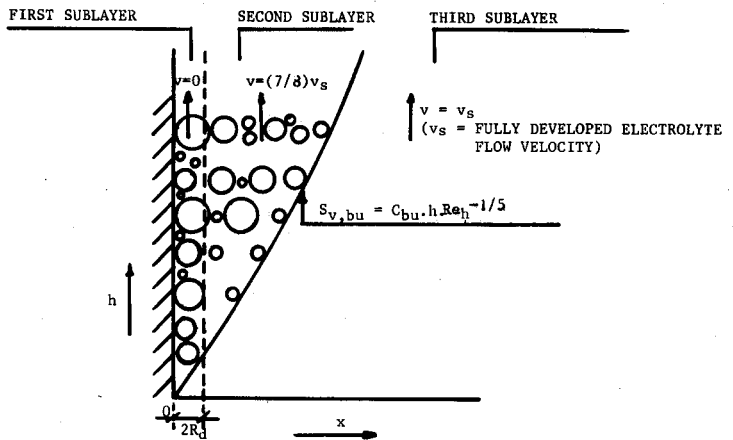
Fig. 6.2 Boundary layer for two-phase flow.

the average bubble departure diameter, $2R_d$; the velocity of this layer is assumed to be zero;

• the second sublayer consists of detached–bubbles with thickness:

$$\delta_{v,bu} - 2R_d, \text{ with} \qquad\qquad\qquad (6.8)$$
$$\delta_{v,bu} = C_{bu}.h.Re_h^{-1/5}$$

where $\delta_{v,bu}$ = the thickness of the velocity boundary layer, C_{bu} = a function of the volumetric gas production rate, h = electrode height and Re_h = the Reynolds number. The velocity of this sublayer is assumed to be $(7/8)\ v_s$, where v_s = the fully developed electrolyte flow velocity.

The third sublayer consists of a bubble–free electrolyte.

The current density distribution at the electrodes is considered to be uniform. The resistance of the first sublayer is derived by using the equation suggested by literature [16]:

$$R/R_p = \frac{1}{2R_d} \int_o^{2R_d} (1 - s(x))^{-3/2} dx \qquad\qquad (6.9)$$

where $s(x)$ = the degree of screening by attached–bubbles at a distance x perpendicular to the electrode. The gas void fraction of the second sublayer is given by:

$$f_h = \frac{8}{7} \frac{RTi}{npF} \frac{h}{v(\delta_{v,bu} - 2R_d)} \qquad\qquad (6.10)$$

with p = the partial pressure of the evolved gas.

The resistance of this sublayer is calculated by applying Bruggeman's equation. The total relative ohmic resistance of the bubble containing electrolyte between the electrode and diaphragm at height h is expressed by:

$$R/R_p = \frac{1}{d_{wm}}[\int_o^{2R_d} (1-s(x))^{-3/2} dx + (\delta_{v,bu} - 2R_d)(1-f_h)^{-3/2} + (d_{wm} - \delta_{v,bu})]$$
$$(6.11)$$

Bongenaar [2] developed a model using pretty much the same idea as Vogt and Sillen. She separated the electrode–diaphragm gap in only two bubble–

electrolyte layers (cf. Fig. 6.3):

● the first layer has a relatively high gas void fraction and a relatively low solution flow velocity; the gas void fraction at the electrode is marked as f_o and decreases linearly over the width of this layer ending at f_b;

● the second layer has a low gas void fraction and a high solution flow velocity; the gas void fraction of this layer is constant and its value is f_b.

The gas void fraction, f_b, is approximately equal the ratio of volumetric gas production rate to volumetric liquid flow rate and it depends on current density, solution flow velocity and height in the electrolysis cell. The resistance of both layers has been calculated by applying Bruggeman's equation. The resistance of the first layer is expressed by:

$$R_1 = \rho_p \int_o^\delta [1 - f_o + (f_o - f_b) \, x/\delta]^{-3/2} dx \qquad (6.12)$$

where R_1 = the resistance of the first layer and δ = the thickness of boundary layer. The resistance of the second layer is given by:

$$R_2 = \rho_p \, (1 - f_b)^{-3/2} \, (d_{wm} - \delta) \qquad (6.13)$$

The total relative ohmic resistance in the electrode—membrane gap is:

$$R/R_p = \frac{\int_o^\delta [1-f_o + (f_o - f_b) \, x/\delta]^{-3/2} \, dx + (1-f_b)^{-3/2} \, (d_{wm}-\delta)}{d_{wm}} \qquad (6.14)$$

In general, the flow profile and the gas void distribution in an industrial cell is totally different, due to the electrode configuration applied.

The design of industrial electrodes permits rapid bubble release to the backside of the electrodes, so that bubble effects on the ohmic resistance can be practically neglected. In other words, the above mentioned models are not applicable to industrial chlor–alkali membrane cells (cf. Chapter 9).

6.2.4 Current density distribution in a gas–evolving electrolysis cell

6.2.4.1 Current density distribution without bubble evolution

The current density distribution for two vertical flat-plate electrodes has been derived by Parrish and Newman [23]. For the derivation of primary current density distribution they assumed:
● no concentration differences, hence mass-transfer overpotential $\eta_d = 0$;
● zero activation overpotential, $\eta_a = 0$.
Under these conditions the primary current density at the electrode is given by:

$$i = \lambda_s \ (d\phi/dx)_{x=0} \tag{6.15}$$

where λ_s = the specific conductivity of the solution, x = the coordinate perpendicular to the electrode surface and $(d\phi/dx)_{x=0}$ = the potential gradient at the electrode surface. With the electroneutrality of the solution, the assumption that λ_s is independent of the concentration and the proper boundary conditions for the Laplace equation, they found for the primary current distribution:

$$\frac{i}{i_{av}} = \frac{\alpha \ \cosh \ \alpha/B \ (\tanh^2\alpha)}{[\sinh^2\alpha - \sinh^2(2h-H) \ \alpha/H]^{\frac{1}{2}}} \tag{6.16}$$

where i = current density, i_{av} = average current density, $\alpha = \pi H/2d$, B = a complete elliptic integral of the first kind, h = the distance to the beginning of the electrode, H = the total electrode length and d = the distance between the electrodes.

For d >> H, respectively, d << H in Eq. (6.16), they obtained (cf. Fig. 6.4):

$$\frac{i}{i_{av}} = \frac{2/\pi}{(1 - (\frac{2h-H}{H})^2)^{1/2}} \qquad \text{,for } d >> H \tag{6.17}$$

$$\frac{i}{i_\infty} = \frac{1}{(1 - \exp(-2\pi h/d) \ )^{1/2}} \qquad \text{,for } d << H \tag{6.18}$$

For H = d/2, the current density at both edges of the electrode approaches infinity and a major part of the middle of the electrode surface is quite uniform in current density. For the hypothetical case,
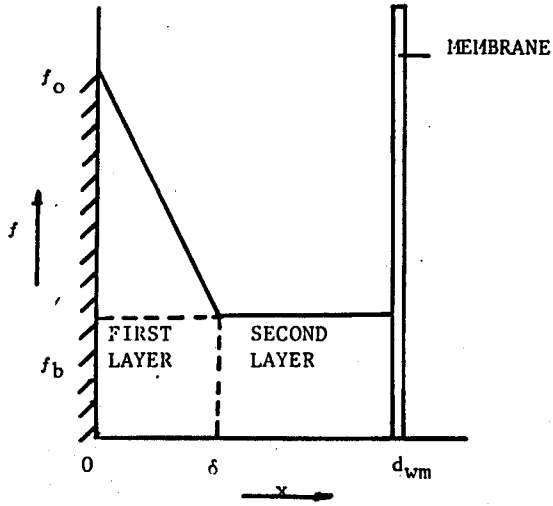
Fig. 6.3   Gas void fraction perpendicular to the electrode surface.
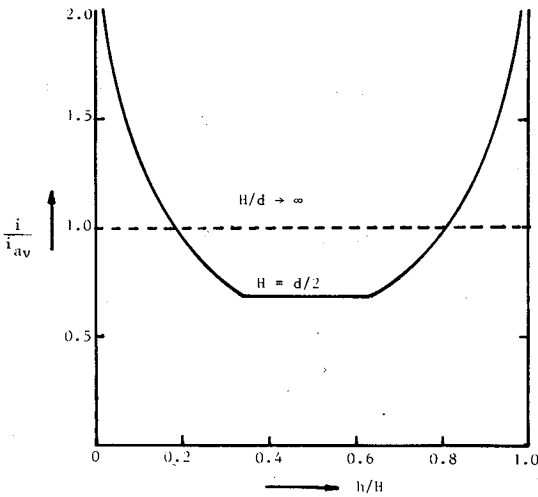
Fig. 6.4   Primary current distributions in a parallel plate reactor.

$H/d \rightarrow \infty$, the current density distribution is uniform over the entire electrode surface.

The secondary current distribution was obtained by solving the Laplace equation with the boundary condition:

$$\phi_0 = \phi_{0.1} - \eta_a \qquad\qquad (6.19)$$

where ϕ_0 = the potential of the solution at the electrode/solution interphase, $\phi_{0.1}$ = the potential of the electrode for the primary current distribution, which is constant and η_a = the activation overpotential, which is a function of the current density. The most simple case is for linear polarization:

$$i = \eta_a \left(\frac{di}{d\eta}\right) = \left(\frac{\alpha i_o F}{RT}\right) \eta_a \qquad\qquad (6.20)$$

Combining Eqs. 6.15, 6.19 and 6.20 results in:

$$\phi_0 = \phi_{0.1} + \frac{\lambda_s R T}{\alpha i_o F} \left(\frac{d\phi}{dx}\right)_{x=0} \qquad\qquad (6.21)$$

The second term on the right hand side of Eq. 6.21 is the correction term for the primary potential. In case the primary current density distribution is unequal, the overpotential, η_a, will have the tendency to create a more uniform secondary current density distribution. High current density increases the activation overpotential, η_a, and decreases the potential of the solution, ϕ_0, because the potential of the electrode, $\phi_{0.1}$, is constant (cf. Eq. 6.19).

The tertiary current density distribution occurs, when:

● the mass transfer overpotential, $\eta_d \neq 0$;

● the activation overpotential, $\eta_a \neq o$.

The boundary conditions for the Laplace equation are now very complicated, because:

● $(d\phi/dx)_{x=0}$ is a function of the concentration and the potential;

● the current density distribution varies with the variation of the ohmic resistance of the bulk electrolyte, the ohmic resistance changes occur when during the electrolysis process conducting or non-conducting species in the electrolyte are produced or consumed;

● the concentration of the different species is a function of the

location in the cell; hence, the conductivity, λ_s, of the solution is no longer a constant.

6.2.4.2 Current density distribution with bubble evolution

In the past, many models have been developed to describe the distribution of i, f and ρ as function of the electrolysis cell parameters, such as electrode height, h, distance between electrodes, d, etc. Most of the authors have applied Maxwell's or Bruggemans's equation to correlate the gas void fraction, f, with the specific resistance, ρ, of the bubble-electrolyte mixture. At increasing height, h, in the cell, all the models predict increasing f and ρ, and decreasing i.

Tobias [3] derived an equation for the relative current density as a function of the gas effect parameter, polarization and electrode height in an electrolysis cell with two vertical flat-plate electrodes, under natural convection condition. For his derivation he assumed:

● the electrode surface is equipotential;
● the bubble size distribution is constant in time and at all level;
● the bubble rise velocity is constant;
● the effect on bubble velocity, due to coalescence, is neglectable;
● the polarization is linear over the working potential range $E_p = b'i_h$;
● the curvature of current flow is disregarded;
● the bubble distribution, at height, h, from the bottom of the electrode, is uniform in the inter-electrode gap.

The unit surface resistance, R_h', at height, h, is given by Bruggeman's equation:

$$R_h' = R_p' \ (1 - f_h)^{-3/2} \tag{6.22}$$

He obtained:

$$\frac{i_h}{i_{av}} = \frac{3}{2} \ . K[(\mu + 1)^2 + 3KH*]^{-\frac{1}{2}}[[(\mu + 1)^2 + 3K]^{\frac{1}{2}} - (\mu + 1)]^{-1} \tag{6.23}$$

where K = the gas effect parameter ($RTUH*/pnF \ \rho_p \ vd^2$), H* = the dimensionless height (h/H), μ = the polarization parameter($b'/\rho_p d$), d = the distance between the electrodes, U = the operating cell voltage and v = the average rising velocity of bubbles. Nagy [24] used about the

similar approach as Tobias to describe the effect of gas evolution on current density distribution for ribbed electrodes.

Funk and Thorpe [4] determined the correlation between the gas void fraction, f, current density distribution, i, slip ratio, s, and electrode height, h, for an electrolysis cell consisting of two vertical flat-plate electrodes and a membrane, under forced flow convection condition. They assumed that:

- both gas and liquid are incompressible and isothermal;
- the bubble distribution between electrodes and membrane, at the same level is uniform;
- the membrane is only permeable for ions and not for liquid or gas.

Applying the laws of conservation of mass, motion and energy, Ohm's law and Mashovets equation (6.4), they found:

$$f = \cfrac{1}{1 + \cfrac{\rho_g}{\rho_s}\, s\, \cfrac{\Gamma_o}{L}} \qquad\qquad (6.24)$$

where

$$f = \frac{A_g}{A} \ \text{(void fraction)}$$

$$s = \frac{v_g}{v_s} \ \text{(slip ratio)}$$

$$\Gamma_o = \left(\frac{d}{H}\right) \left(\frac{n\,\rho_1\,U_\ell}{i_1\,M_g}\right) \ \text{(non-dimensional parameter)}$$

$$L = \int_o^{h/H} \frac{i}{i_1}\, d\!\left(\frac{h}{H}\right) \ \text{(integral of non-dimensional parameter)}$$

where A_g = area occupied by gas, A = the area occupied by gas and liquid, v_g = the actual gas velocity in the cell, v_s = the actual liquid velocity in the cell, d = the distance between electrode and membrane, H = the total electrode height, h = the height from the bottom of the electrode, n = the number of electrons transferred in the reaction, ρ_g = the gas density in the cell, ρ_s = the liquid density in the cell, ρ_1 = the liquid inlet density, $v_{s,o}$ = the superficial solution velocity, i_1 = the current density under inlet conditions and M_g = the atomic weight of the gas.

Bongenaar [2] derived an empirical equation for the local current density distribution as a function of the average current density, i_{av}, and the

superficial solution flow velocity, $v_{s,o}$, for a water electrolysis cell consisting of two vertical nickel flat-plate electrodes under forced convection. She obtained:

$$i_h = i_{av} + 0.24 \left(\frac{H-2h}{2H}\right) (1 - v_{s,o}^{0.06}) \, i_{av}^{1.6} \qquad (6.25)$$

where i_h = the current density at height, h. This empirical equation is valid for the current density range from 2 to 10 kA m^{-2} and a solution flow velocity range from 0.05 to 1.0 m s^{-1}.

None of the suggested models can, however, be applied for industrial chlor-alkali membrane cells, because of the special electrode configuration of the industrial electrodes (cf. Chapter 9).

6.3 Experimental

6.3.1 Determination of gas void fraction and its distribution

6.3.1.1 Apparatus

The experimental set-up, proposed by L.J.J. Janssen, used to determine the gas void fraction in an electrolysis cell is shown schematically in Fig. 6.5. The perspex cell (external 70 cm high) was divided into a working- and a counter-electrode compartment, by a cation-exchange membrane (Nafion 117).

The working-electrode compartment had an inner cross-section of 1.73 cm^2 and a height of about 70 cm. The working-electrode consisted of 5 segments (each 10 cm high, 2 cm wide and 0.5 cm thick) and was placed against the backwall of the working-electrode compartment; the distance of the working electrode to the membrane was 0.865 cm.

The working-electrode material was nickel or nickel-teflon plate for hydrogen and oxygen evolution; for chlorine evolution a titanium plate coated with RuO_2 was used.

The counter-electrode compartment had an inner cross-section of 2.20 cm^2 and a height of about 70 cm. The counter-electrode was a nickel venetian blind electrode (50 cm high, 2 cm wide and 0.5 cm thick) and was mounted against the membrane.
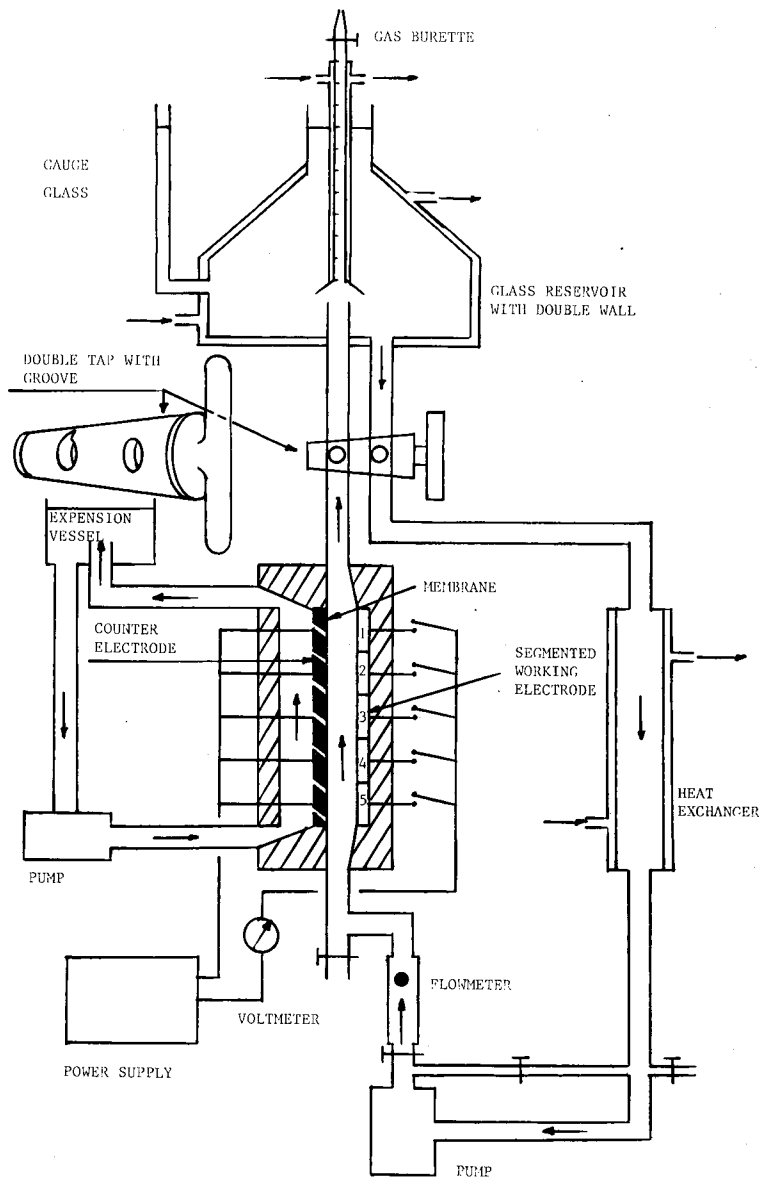
Fig. 6.5   Schematical set-up for measurement of gas void fraction.

In the working-electrode compartment a 6.8 M NaOH has been used as catholyte for hydrogen evolution and as anolyte for oxygen evolution. For the chlorine evolution a solution of 3.5 M NaCl plus 0.5 M HCl was used as anolyte. All solutions were saturated with the gas evolved. The counter-electrode compartment solution flow circuit was filled with 6.8 M NaOH.

The working-electrode compartment was connected to a solution flow circuit, which consisted of a pump (Schmitt-Kreisel, type MPN), valves, a flowmeter (no. 3F-3/8-25-5/36), a double tap, a degassing glass reservoir with double wall for heating, a gauge glass and a heat-exchanger.

The heat-exchanger and the degassing reservoir were thermostatted.

The solution volume in the working-electrode compartment was about 6000 cm^3.

The counter-electrode compartment has a separate solution flow circuit, which consisted of a pump (Eheim, type 1018) and a degassing reservoir; the total solution volume was about 500 cm^3.

The constant current was supplied by a power-supply (Farnell, type H30/100 (0-40 V, 0-150 A). The current was measured with a resistance of 1 m Ω and a digital voltmeter (Keithly, 177 DMM).

By closing the double tap, the degassing reservoir of the working-electrode flow circuit was separated from both the working-electrode compartment and the heat-exchanger.

The tap which separated the degassing reservoir and the cell compartment had a narrow-groove with a total volume of 6.8 cm^3 (cf. Fig. 6.5). This groove was able to release only the gas bubbles present in the tap passage, when the tap was opened carefully. The volume of released gas was measured with a gas buret (cf. Fig. 6.5).

6.3.1.2 Calculations

During the electrolysis only part of the gas formed is evolved as bubbles, the rest of the gas remained in the solution.

For the time being, no reliable techniques are available to measure the gas supersaturation in a semi-industrial cell. Therefore and for simplicity's sake, we assume that the current efficiency is 100% and that all the gas formed is evolved as bubbles, saturated with water-vapour. The inlet solution of the cell is saturated with the gas evolved.

The slip ratio, s, in the cell is:

$$s = v_g/v_s \qquad\qquad (6.26)$$

i.e. the ratio between the actual bubble velocity, v_g, and the actual solution flow velocity, v_s.

A relation between s and f can be obtained as follows.
The actual bubble velocity, v_g, is defined by:

$$v_g = v_{g,o}/f \qquad\qquad (6.27)$$

with f, the gas void fraction, i.e. the part of the volume of the dispersion, that is occupied by the bubbles in absence of gas supersaturation:

$$f = v_{g,o}/v_g \qquad\qquad (6.28)$$

so:

$$(1-f) = v_{s,o}/v_s \qquad\qquad (6.29)$$

where $v_{g,o}$ = the superficial gas velocity and $v_{s,o}$ = the superficial solution flow velocity.
As the gas void fraction, f, cannot exceed one, at high current densities, v_g should increase with increasing f.
The superficial gas bubble velocity is then:

$$v_{g,o} = \frac{iV_M}{nF} \times \frac{T}{298} \times \frac{p(g + H_2O)}{p(g + H_2O) - p(H_2O)} \quad (m\ s^{-1}) \qquad\qquad (6.30)$$

Substitution of Eq. (6.27) and (6.29) into (6.26) gives:

$$s = \frac{v_{g,o}(1-f)}{v_{s,o}\ f} \qquad\qquad (6.31)$$

Rearranging gives:

$$f = \frac{v_{g,o}}{v_{g,o} + s\ v_{s,o}} \qquad\qquad (6.32)$$

In case the cross-section of the cell, A_c, deviates from the electrode surface area, A_e, Eq. 6.32 has to be modified into:

$$f = \frac{V_{g,o}}{V_{g,o} + s\,V_{s,o}} = \frac{v_{g,o} \times A_e}{(v_{g,o} \times A_e) + s\,(v_{s,o} \times A_c)} \qquad (6.33)$$

were $V_{g,o}$ = the volumetric gas production rate $(m^3 s^{-1})$ and $V_{s,o}$ = the volumetric solution flow rate $(m^3 s^{-1})$.

Consequently, the slip ratio, s, can be determined experimentally by measuring f.

A novel technique has been developed to measure the gas void fraction in a semi-industrial electrolysis cell. It operates as follows:

during the electrolysis all 5 segments were switched on; the numbering sequence of the cell segments is from top to bottom (cf. Fig. 6.5); after switching off the current, pump and tap, simultaneously, the gas caught in the tap was carefully released through the groove of the tap, and the total gas volume, $V_{tap,5}$, was measured with the gas burette (cf. Fig. 6.5).

The gas void fraction in the tap, whereby 5 segments were producing gas, is denoted as $f_{tap,5}$:

$$f_{tap,5} = V_{tap,5}/V_{tap} \qquad (6.34)$$

$V_{tap,5}$ = the total gas volume in the tap was measured, as said, by means of a gas burette and corrected for hydrostatic pressure; V_{tap} = the total volume of the passage of the tap (6.8 cm^3).

Here, it is assumed that:

$$f_{tap,5} = f_{1,5} \qquad (6.35)$$

where $f_{1,5}$ = the gas void fraction at the upper edge of electrode segment 1, during gas evolving at all 5 electrode segments.

So, the notation $f_{x,y}$, stands for the gas void fraction, at the upper edge of electrode segment x, during gas evolution at the top y electrode segments; evenso $f_{tap,k}$, stands for the gas void fraction in the tap, during gas evolution of the top (k) electrode segments.

Experimentally, it was found that:

$$f_{1,1} = f_{2,1} = f_{3,1} = f_{4,1} = f_{5,1} \qquad (6.36)$$

So, it is reasonable to assume that:

$$f_{1,5} = f_{tap,5} \qquad\qquad\qquad (6.37)$$

Furthermore, it can be shown experimentally, that:

$$f_{2,5} = f_{1,4} = f_{tap,4} \qquad\qquad (6.38)$$
$$f_{3,5} = f_{1,3} = f_{tap,3} \qquad\qquad (6.39)$$
$$f_{4,5} = f_{1,2} = f_{tap,2} \qquad\qquad (6.40)$$
$$f_{5,5} = f_{1,1} = f_{tap,1} \qquad\qquad (6.41)$$

Therefore, the gas void fraction at the height of the upper edge of each of the five gas-evolving segments can be determined by taking the right combination of active electrode segments and by measuring $V_{tap,k}$ and correcting for hydrostatic pressure of each combination, separately.

6.3.2 Preparation of electrodes

6.3.2.1 Preparation of RuO_2 electrode [25]

The titanium plate was degreased, grated and etched lightly with diluted HCl.
A solution of 0.1 M $RuCl_3$ and 20 wt% HCl was brought on one side of the plate surface by means of a small brush. Then, the treated plate was heated in air during 10 minutes at 723 K.
This procedure was repeated six times. Finally, the plate was heated for one hour at 723 K.

6.3.2.2 Preparation of Ni-teflon electrode [26]

The nickel plate (10 x 2 x 0.5 cm) was grated with emery-paper, rinsed with distilled water, etched with a solution of concentrated HNO_3 and HCl, and again rinsed with distilled water.
The cleaned nickel plate was put vertically into an electrolysis cell between two perforated plate anodes.
A "Wattsbad" (containing $NiSO_4$ (1 M), $NiCl_2$ (0.1 M) and H_3BO_3 (10 g/l)), to which 30 g/l teflonpowder (5 to 10 µm) and 10 g/l Monoflor 71 (damper) was added, was used as electrolyte.
The electrolysis was carried out during 10 minutes, under constant stirring (magnetic stirrer), at I = 10 A and T = 40 °C.

6.4 Results

6.4.1 Effect of current density

The gas void fraction, $f_{1,5}$, for oxygen, hydrogen and chlorine bubbles is plotted as a function of current density, i_g, at 351 K and $v_{s,o} = 0.05$ m s^{-1} in Fig. 6.6.

From this figure, it can be concluded that $f_{1,5}$ for the three gases increases linearly with increasing i_g.

Further, the gas void fraction for Cl_2 and H_2 reaches a limiting value at high current density of about 7 and 9 kA m^{-2}, respectively. For O_2 a current density of more than 10 kA m^{-2} is required, before the limiting gas void fraction can be obtained.

6.4.2 Effect of height

In Fig. 6.7 the gas void fraction in the cell is shown as a function of the electrode height, h, at 351 K, 4 kA m^{-2} and a solution flow velocity of 0,05 m s^{-1}.

The results obtained indicate that the gas void fraction in the cell for all three gases increases practical linearly with increasing height of the electrode, for h from about 0 to 40 cm. Under the operation condition mentioned, no limited gas void fraction has been observed.

6.4.3 Effect of solution flow velocity

Fig. 6.8 shows the gas void fraction, $f_{1,5}$, for the three gases versus the superficial solution flow velocity, $v_{s,o}$, at 351 K and a current density of 5 kA m^{-2}. This figure shows that the gas void fraction for oxygen and hydrogen decreases with increasing $v_{s,o}$, while the gas void fraction for chlorine decreases only slightly with increasing $v_{s,o}$, for $v_{s,o}$ from 0,03 to 0,10 m s^{-1}.

6.4.4 Effect of temperature

The dependence of the gas void fraction, $f_{1,5}$, for both hydrogen and chlorine, on the temperature, at 5 kA m^{-2} and a solution flow velocity of 0,05 m s^{-1}, is illustrated in Fig. 6.9. From this figure, it follows that
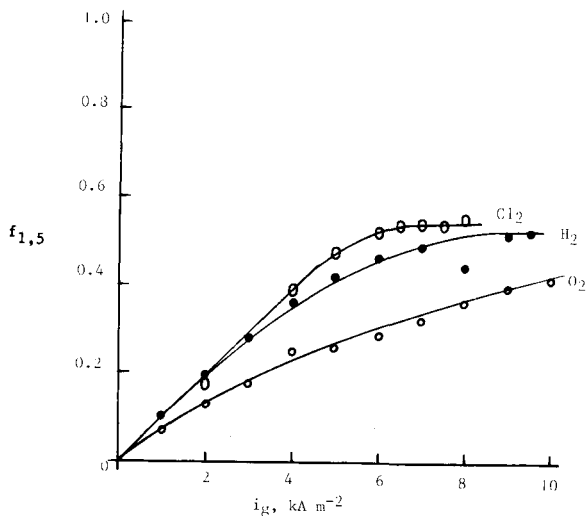
Fig. 6.6 Gas void fraction, $f_{1,5}$ as a function of current density, i_g, for oxygen and hydrogen evolution on a segmented flat-plate nickel electrode in 6.8 M NaOH, at 351 K and a solution flow velocity of 0.05 m s^{-1}; evenso for chlorine evolution on a segmented flat-plate RuO$_2$/Ti electrode in 3.5 M NaCl + 0.5 M HCl, at 351 K and a solution flow velocity of 0.05 m s^{-1}.
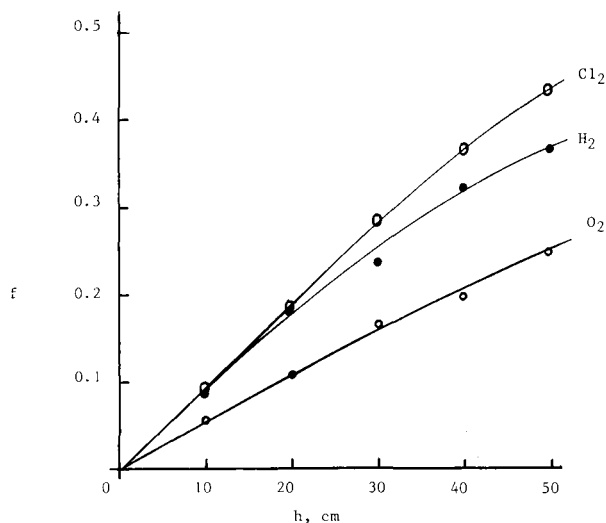
Fig. 6.7 Gas void fraction in the cell vs. height of the electrode for oxygen and hydrogen evolution on a segmented flat-plate nickel electrode in 6.8 M NaOH, at 351 K, 4 kA m^{-2} and a solution flow velocity of 0.05 m s^{-1}; evenso for chlorine evolution on a segmented flat-plate RuO$_2$/Ti electrode in 3.5 M NaCl + 0.5 M HCl, at 351 K, 4 kA m^{-2} and a solution flow of 0.05 m s^{-1}.

– 87 –
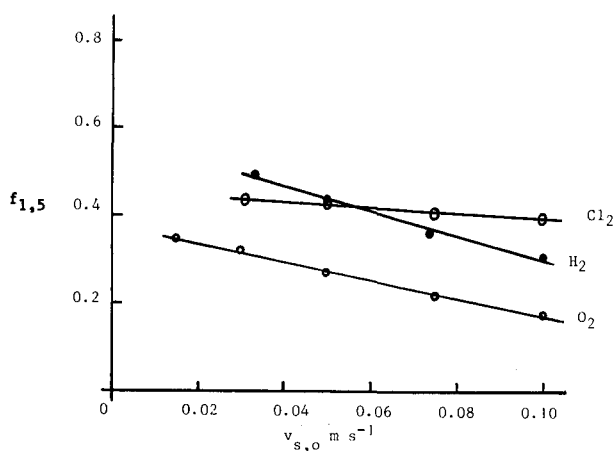
Fig. 6.8 Gas void fraction, $f_{1,5}$, as a function of the superficial solution flow velocity for oxygen an hydrogen evolution on a segmented flat-plate nickel electrode in 6.8 M NaOH, at 351 K and a current density of 5 kA m^{-2}; evenso for chlorine evolution on a segmented flat-plate RuO2/Ti electrode in 3.5 m NaCl + 0.5 M HCl, at 351 K and a current density of 5 kA m^{-2}.
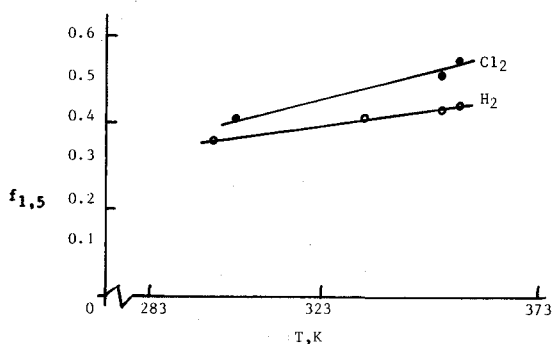
Fig. 6.9 Gas void fraction, $f_{1,5}$, vs. temperature for hydrogen evolution at a segmented flat-plate nickel electrode in 6.8 M NaOH, at 5 kA m^{-2} and a solution flow velocity of 0.05 m s^{-1}; evenso for chlorine evolution on a segmented flat-plate RuO$_2$/Ti electrode in 3.5 M NaCl + 0.5 M HCl, at 5 kA m^{-2} and a solution flow velocity of 0.05 m s^{-1}.

– 88 –

for both gases the gas void fraction increases linearly with increasing temperature, for T from 298 to 355 K.

6.4.5 Effect of electrode material

Fig. 6.10 (for oxygen) and 6.11 (for hydrogen) show the gas void fraction, $f_{1,5}$, as a function of current density for two different electrode materials, viz.: Ni and Ni-teflon electrodes, at 351 K and $v_{s,o}$ = 0.05 m s^{-1}.
The gas void fraction for oxygen depends clearly on the electrode material, for i_g from 1 to 10 kA m^{-2}; while for hydrogen a difference in gas void fraction only appears at a current density greater than 3 kA m^{-2}.

6.5 Discussion

Generally speaking, the gas void fraction behaviour for electrogenerated oxygen, hydrogen and chlorine in a vertical flat-plate electrode cell shows practically the same trend (cf. Fig. 6.6 - 6.9). These trends confirm earlier reports [3-4]. A limiting gas void fraction has been found for hydrogen and chlorine, at i_g of about 8 kA m^{-2}, with values of 0.52 and 0.54, respectively (cf. Fig. 6.6).
The limiting gas void fraction for oxygen is expected to be occur, at i_g of about 16 kA m^{-2}.
The limiting gas void fraction found by Kreysa et al. [5], however, was considerably lower.
These differences are evidently caused by the different operating conditions.
Eq. 6.32, shows that the gas void fraction, f, approaches that for an infinite superficial gas velocity, $v_{g,o}$.
Experimentally, it has been found that the limiting gas void fraction is much lower than one. This is probably caused by the fact that f depends on the slip ratio, $s = v_g/v_s$, which, in turn, depends on many factors, such as: superficial gas velocity, superficial solution velocity, current density, bubble diameter, temperature, etc.
It has been found that s decreases with increasing $v_{s,o}$, respectively, increases with increasing temperature, within the investigated range.
The calculated slip ratio versus the current density is plotted in Fig. 6.12. For chlorine evolution the slip ratio decreases with increasing
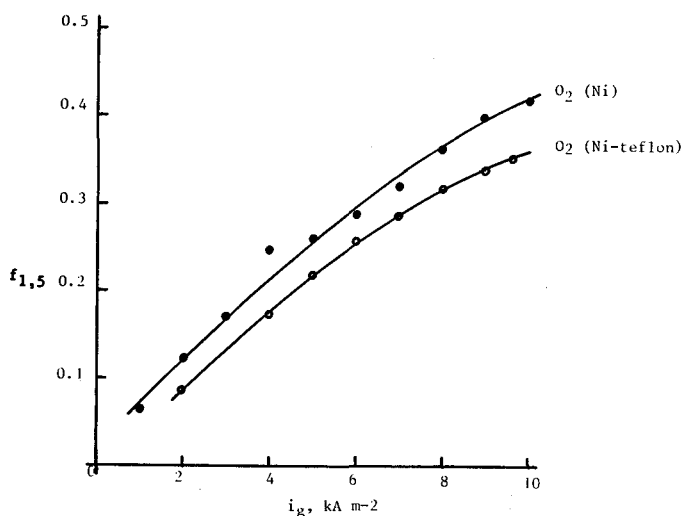
Fig. 6.10 Gas void fraction, $f_{1,5}$, as a function of current density for an oxygen-evolving, segmented flat-plate electrode of nickel and nickel-teflon in 6.8 M NaOH, at 351 K and a solution flow velocity of 0.05 m s⁻¹.
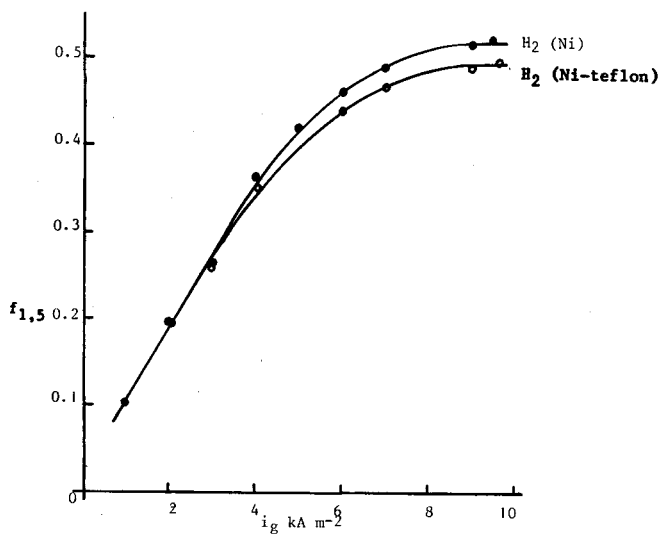
Fig. 6.11 Gas void fraction, $f_{1,5}$, as a function of current density for a hydrogen-evolving, segmented flat-plate electrode of nickel and nickel-teflon in 6.8 M NaOH, at 351 K and a solution flow velocity of 0.05 m s⁻¹.
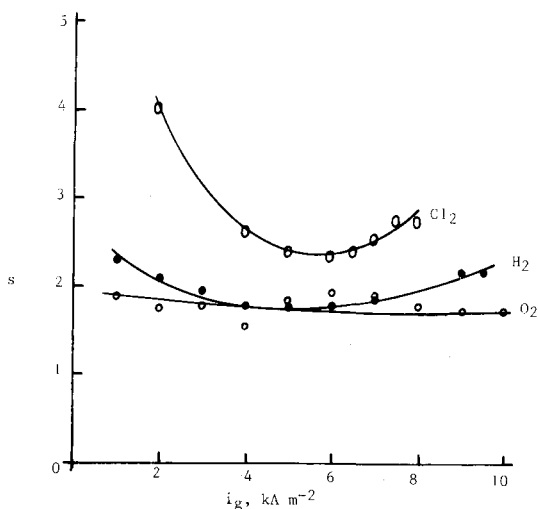
Fig. 6.12 Slip ratio, s, versus current, i_g, for oxygen and hydrogen evolution on a segmented flat-plate nickel electrode in 6.8 M NaOH, at 351 K and a solution flow velocity of 0.05 m s^{-1}; evenso for chlorine evolution on a segmented flat-plate RuO$_2$/Ti electrode in 3.5 M NaCl + 5 M HCl, at 351 K and a solution flow velocity of 0.05 m s^{-1}.

current density from 2 to about 6 kA m^{-2}; from 6 to 8 kA m^{-2}, however, the slip ratio increases with increasing current density. The decreasing part of the curve can be explained by the well-known fact that the rise velocity of a bubble swarm is less than that of a single bubble. So, it is reasonable to assume that the actual bubble velocity, v_g, or s decreases with increasing current density. At higher current densities coalescence of gas bubbles can be expected, resulting in bigger bubbles. According to the Stokes equation (cf. 3.11), the single bubble velocity will increase. Hence, s will also increase with increasing current density. The same reasoning can be applied to elucidate the dependence of s and i_g for hydrogen evolution and oxygen evolution.

It should be emphasized that the results show in Fig. 6.6 and 6.7 are only valid for flat-plate gas-evolving electrodes and not for expanded mesh or perforated plate electrodes, which are commonly used in the industrial chlor-alkali membrane cells. The results obtained indicated that f increases with increasing height of the electrode (cf. Fig. 6.7). The limiting gas void fraction will be reached at a certain electrode

height and above this height the gas void fraction remains constant. In other words, there is no need to construct low electrolysis cells, because the effect of electrode height on the cell voltage after a certain electrode height is negligible.

The above arguments are not applicable to the industrial chlor-alkali membrane cell, because the used electrode configurations permit rapid bubble release at the backside of the electrodes, so that no bubble accumulation takes place between the anode and cathode gap. Consequently, by applying the proper electrode configurations, it is possible to reduce the ohmic resistance of the bubble-solution mixture within the interelectrode gap to a minimum (cf. Chapter 9). Hence, the electrode height has practically no effect on the cell voltage. Thus the electrolysis cells can be constructed as high as desired, without influencing the cell voltage significantly. This conclusion is in contrast with current opinion.

6.6 References

1   C.W.M.P. Sillen, Thesis, Eindhoven University of Technology, 1983
2   B.E., Bongenaar-Schlenter, Thesis, Eindhoven University of Technology, 1984
3   C.W. Tobias, J. Electrochem. Soc. 106 (1959) 833
4   J.E. Funk and J.F. Thorpe, J. Electrochem. Soc. 116 (1969) 48
5   G. Kreysa, M. Kuhn, J. Appl. Electrochem. 15 (1985) 517
6   H. Vogt, Electrochim. Acta. 26 (1981) 1311
7   J.C. Maxwell, A. treatise on electricity and magnetism, 2nd. ed., Vol. 1, Clarendon Press, Oxford (1881)
8   H. Fricke and S. More, Phys. Rev. 25 (1925) 361
9   A. Eucken, VDI-Forschungsheit 353 (1932) 353
10 C. Orr and J.M. Dalla Valla. Chem. Eng. Progr. Symposium Ser. No. 9, 5 (1954) 29
11 D.A. de Vries, Annexe 1952-1 au Bulletin de l'Institute du Froid, Paris (1952) 115
12 R.E. Meredith and C.W. Tobias, Advances in Electro Chemistry and Electrochemical Engineering, Vol. II, John Wiley & Sons, New York (1962)
13 Lord Rayleigh, Phil. Mag. 34 (1892) 481
14 D.A.G. Bruggeman, Ann. Physik 24 (1935) 659

15 R.E. de la Rue and C.W. Tobias, J. Electrochem. Soc. 106 (1959) 827

16 L.J.J. Janssen and E. Barendrecht, Electrochim. Acta 28 (1983) 341

17 V.P. Mashovet, J. Appl. Chem. (USSR) (English Translation) 24 (1951)
    391

18 I. Rousar, V. Cezner, J. Negepsova, M.M. Jaksic, M. Spasojevic and
    B.Z. Nikilic, J. Appl. Electrochem. 7 (1977) 427

19 I. Rousar, J. Electrochem. Soc. 116 (1969) 676

20 F. Hine, M. Yasuda, R. Nakamura and T. Noda, J. Electrochem. Soc. 122
    (1975) 1185

21 H. Vogt, Electrochim. Acta. 26 (1981) 1311

22 F. Hine and K. Murakami, J. Electrochem. Soc. 117 (1970) 292

23 W.R. Parrish and J. Newman, J. Electrochem. Soc. 117 (1970) 43

24 Z. Nagy, J. Appl. Electrochem. 6 (1976) 171

25 S. Transatti, Electrodes of conductive Metallic Oxides, Parta,
    Elsevier Publishing Company, Amsterdam, Oxford, New York (1980) 315

26 Patent AKA 1431, Partent Application No. 13423/73 filed 2'th March
    1973

27 C.J. West, International Critical Tables Vol. III, 370, McGraw-Hill,
    New York, London (1933)

Chapter 7

Membrane resistance in a chlor–alkali electrolysis cell process

7.1 Introduction

The world's first commercial membrane chlor–alkali process was started in Japan in 1975 [1].

In the membrane cell process approximately 12% of the total cell voltage is caused by the membrane voltage drop. This membrane drop depends on many factors such as: the cell operation conditions, the membrane composition, its thickness, the type of mechanical reinforcement, and, in the case of the asymmetric membrane or bimembrane: the thickness of the barrier layer. A bilayer membrane consists of a very thin layer of perfluorocarboxylic acid (about 2–10 μm thick) and a layer of perfluorosulfonic acid (about 0.3 mm thick).

The last ten years marked progress has been achieved in improving the membrane properties.

At present, high quality bimembranes (current efficiency of about 95,5%, low resistance and excellent service life) are commercially available.

The high current efficiency of the bilayer membrane is due to the low water content of the perfluorocarboxylic acid layer; thus, high fixed anion concentration in the carboxylic acid layer faces the catholyte and prevents migration of hydroxide ion. The perfluorosulfonic acid layer is unable to prevent such migration, due to its high water content (low fixed anion concentration) and its high dissociation constant.

During the chlor–alkali membrane cell process, hydrochloric acid is added to the anolyte to prevent oxygen gas evolution. It is very important that the anolyte acidity doesn't exceed 0.01 M (pH > 2), because a higher acidity decreases the conductivity of the perfluorocarboxylic acid layer of the membrane drastically due to the lower dissociation constant of the carboxylic acid group.

To prevent gas bubble adhesion on the membrane surface, different techniques have been applied. For example, by increasing the hydrophilicity of the surface by covering it with a porous, non–corrosive and non– electroconductive inorganic layer [2] or by roughening the surface of the membrane during its manufacture [3].

At present, the energy requirement for the membrane cell process is less

than that for the mercury cell and the diaphragm cell process. For this and for more reasons, it is clear that the membrane cell process will be the predominant process for chlorine and caustic production in the future. In order to provide the proper scientific basis for the optimization of membrane cell technology, it is important to have a good insight into the ion transport mechanism in the membrane during the electrolysis.

As far as we know, no good membrane resistance measuring techniques are reported in the literature. So, we have developed a method to measure the membrane resistance at ambient temperature and under industrial conditions.

First, however, in this Chapter a short literature review concerning diaphragm and membrane resistance is presented in Section 7.2.

In Section 7.3, the experimental set-up of the impedance and resistance measuring technique is described.

In Section 7.4, the obtained results are presented. The results are discussed in Section 7.5.

7.2 Literature review

7.2.1 Diaphragm

In order to prevent mixing of solutions, the cell is divided into two compartments by means of a diaphragm, which may be made of porous plastic, or made of porous ceramic or asbestos deposited on a gauze [4]. The diaphragm resistance $R_D = R_2 - R_1$ (cf. Fig. 7.1 and 7.2), where $R_1 =$ the electrolyte resistance (Ω) and $R_2 =$ the electrolyte plus diaphragm resistance (Ω) [5].
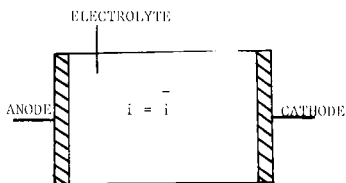
Fig. 7.1 Resistance of the cell filled with electrolyte, R_1, (Ω) without diaphragm.
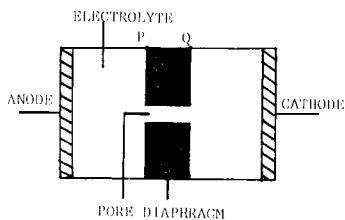
Fig. 7.2 Resistance of the cell with electrolyte, R_2, (Ω) with diaphragm of one pore.

During the electrolysis, the diaphragm creates an additional joule heat
between P and Q (cf. Fig. 7.2). The heat is given by:

$$W = \rho_p \times i^2 \qquad\qquad\qquad (7.1)$$

where W = the joule heat (J s^{-1} m^{-3}), ρ_p = the specific resistance of the
pure electrolyte (Ω m) and i = the current density (A m^{-2}).
The additional joule heat is developed mainly in front of and within the
pore due to a concentration of the electric field lines pattern, i.e.
where i >> i.
A real diaphragm is permeable for all ions present in the electrolyte.
The transport numbers of these ions in the diaphragm are the same as
those of the bulk solution. Consequently, it can be considered as a
geometric obstruction, a narrowing.
Moreover, no concentration or depletion of ions takes place adjacent to
or in the diaphragm. This means that the solution flow velocity has no
effect on the diaphragm resistance [8].

7.2.2 Membrane

7.2.2.1 Structure, swelling and ion transport

A Nafion perfluorosulfonic acid membrane consists of a perfluorinated
backbone, having pendant groups of the form [6-7]:
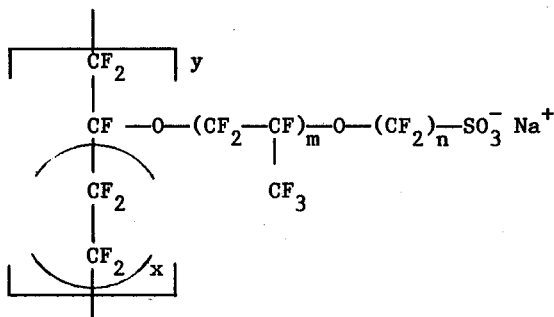
where 5 < x < 13, y ≈ 1000, 0 < m < 3 and 2 < n < 6.
The cluster-like structure of this membrane is shown in Fig. 7.3 [7].
The hydrophilic SO_3^- group is responsible for the swelling of the
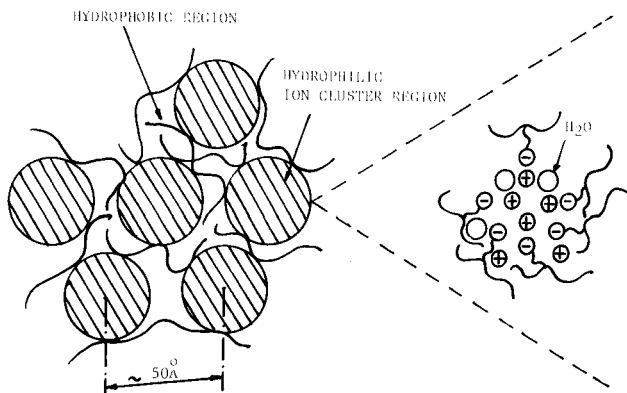
Fig. 7.3 Microphase building-up of nafion by a hydrophobic fluorcarbon region and a hydrophilic ion cluster region.
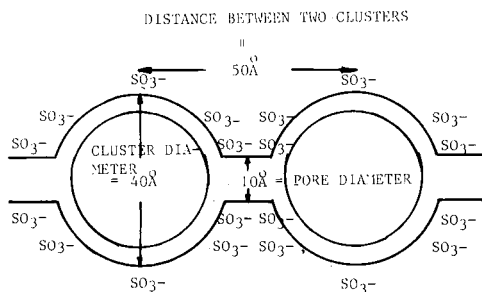
Fig. 7.4 Schematic illustration of the cluster-network model of Gierke.

hydrophobic polymer network on exposure to water.

Swelling of the membrane mainly depends on the pK of the ionogenic group and its concentration, in the sense that the equilibrium water-uptake for strong acid membranes exceeds that of membranes containing less hydrophilic weak acid groups due to the higher dissociation constant of the strong acid groups. Consequently, much more water is required for the hydratation of the strong acid groups.

Gierke [7] had developed a cluster network model to describe ion transport in a Nafion perfluorosulfonic acid membrane, see Fig. 7.4.

In this model, the cluster structure can be described as inverse micelles in which the SO_3^- sites are present in a spherical water domain. Gierke suggested, that OH^- ions will be excluded by electrostatic repulsive forces from the surface of the clusters and pores. If an OH^- ion migrates

through a membrane, it experiences an oscillating potential, low in the cluster and high in the pore; the cluster diameter (40 Å) is larger than the pore diameter (10 Å) (cf. Fig. 7.4).

7.2.2.2 Concentration profile

In a cation-selective membrane chlor-alkali process, the transport number of the Na^+ ion in the membrane is one and thus higher than in the bulk of the anolyte, resulting in the formation of a boundary (diffusion) layer depleted of NaCl on the anode side of the membrane and concentration of NaOH on the cathode side of the membrane (cf. Fig. 7.5).
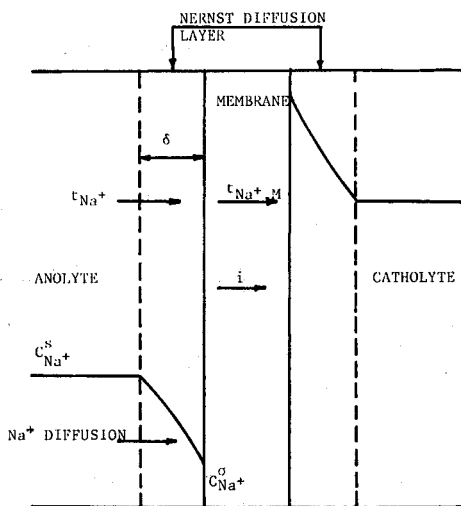
Fig. 7.5   Concentration profile on the surface of membrane.

During electrolysis this membrane has a quite similar concentration profile as at an electrode (cf. Fig. 7.5); however, no electron charge transfer reactions occur at the membrane surface.

The material balance of the depleted layers at steady state at the anode side is expressed by [8]:

$$t_{Na^+,M} \frac{i}{F} = t_{Na^+} \frac{i}{F} + \frac{D}{\delta} (c^s_{Na^+} - c^\sigma_{Na^+}) \qquad (7.2)$$

where i = the current density (A m^{-2}), $t_{Na^+,M}$ = the transport number of Na^+ in the membrane, F = the Faraday's constant (96487 x 10^3 C keq^{-1}),

t_{Na^+} = the transport number of Na^+ ion in the anolyte, D = the NaCl diffusion coefficient in the depleted layer (m^2 s^{-1}), $c^s_{Na^+}$ = the concentration of Na^+ in the bulk anolyte (keq m^{-3}), $c^\sigma_{Na^+}$ = the concentration of Na^+ in the depleted layer at the membrane surface and δ = the thickness of depleted layer (m).

The left hand side of the Eq. 7.2 represents the flux of Na^+ ions through the cation-selective membrane.

The $t_{Na+} \dfrac{i}{F}$ term on the right hand side represents the flux of Na^+ ion by migration. The second term of the right hand side represents the flux of supply of Na^+ to the membrane surface by diffusion from the bulk solution.

At the limiting current density, i_1, $c^\sigma_{Na^+}$ becomes zero and Eq. 7.2 becomes:

$$\frac{i_1 \delta}{c^s_{Na^+}} = \frac{DF}{t_{Na^+,M} - t_{Na^+}} \qquad (7.3)$$

The Nernst diffusion layer, δ, is determined by the anolyte flow velocity and the cell structure. This means that the solution flow velocity affects the membrane resistance and so the membrane energy loss.

The right hand side of Eq. 7.3 is determined by the membrane characteristics and the electrolysis temperature. If the supply of salt to the membrane is running short at the limiting current density, the water at the anode is decomposed, and the current flow is transported partly by migration of generated H^+ ions. The so-called polarization causes lower current efficiency and thus a higher electrolysis voltage.

Energy losses in a membrane can be calculated by measuring the potential drop across the membrane or the electrical resistance of the membrane.

It should be stressed that the membrane resistance is only defined in combination with both electrolyte compositions and the operating conditions.

So, during the chlor-alkali electrolysis energy losses occur in and on the membrane.

The major energy loss is caused by the frictional losses of the moving Na^+ ions in the membrane (ohmic loss). To transfer Na^+ ions from the

anolyte with low activity to the catholyte with high activity, the Na^+
ions have to overcome a membrane potential, $\Delta\phi$:

$$\Delta\phi = 2.3 \cdot \frac{RT}{F} \, t_{Na+,M} \, \log \frac{a_{Na^+} \, (catholyte)}{a_{Na^+} \, (anolyte)} \quad (7.4)$$

where $t_{Na+,M}$ = the transport number of species Na^+ in the membrane, a_{Na}^+
= the activity of species Na^+ outside the membrane. At room temperature
the value for 2.3 RT/F is 0.059 V and at 363 K it is 0.072 V.
The energy required the overcome this potential barrier is stored in the
system and cannot be recovered, so it has to be considered as an energy
loss.

7.3 Experimental

7.3.1 Determination of membrane impedance and resistance

A schematic set-up of the measuring system is depicted in Fig. 7.6. The
measurement was performed in a perspex cell divided into two equal
compartments (1 cm wide, 1 cm deep and 10 cm high) by a cation-selective
membrane (Nafion).
The adjustable anode and cathode consisted of a thin platinum sheet (1 cm
wide and 10 cm high) with a hole in the middle (for the reference
electrode), diameter 0.5 cm, and placed against the backwall of the cell.
Both electrode compartments were connected to a separate teflon solution
flow circuit. Each circuit had a pump, flow meter, thermostatted bath,
degassing reservoir, tap and platinum adjustable reference electrode
(wire diameter 0.5 mm and capillary tip diameter 1 mm).
Both electrode compartments were filled with a solution of 24 wt% NaCl
plus 1 wt% NaOH.
The AC (alternating current) and AC/DC (alternating current superimposed
on the direct current) impedance experiments were performed with a
Solartron Frequency Response Analyser (1250). For DC resistance
measurements, the current was adjusted galvanostatically (Delta
Electronika D050-10) and the voltage drop across the adjustable reference
electrodes was measured by an automatic multimeter (PM 2519 Philips).
The volume of solution in both compartments was about 2000 cm^3. The
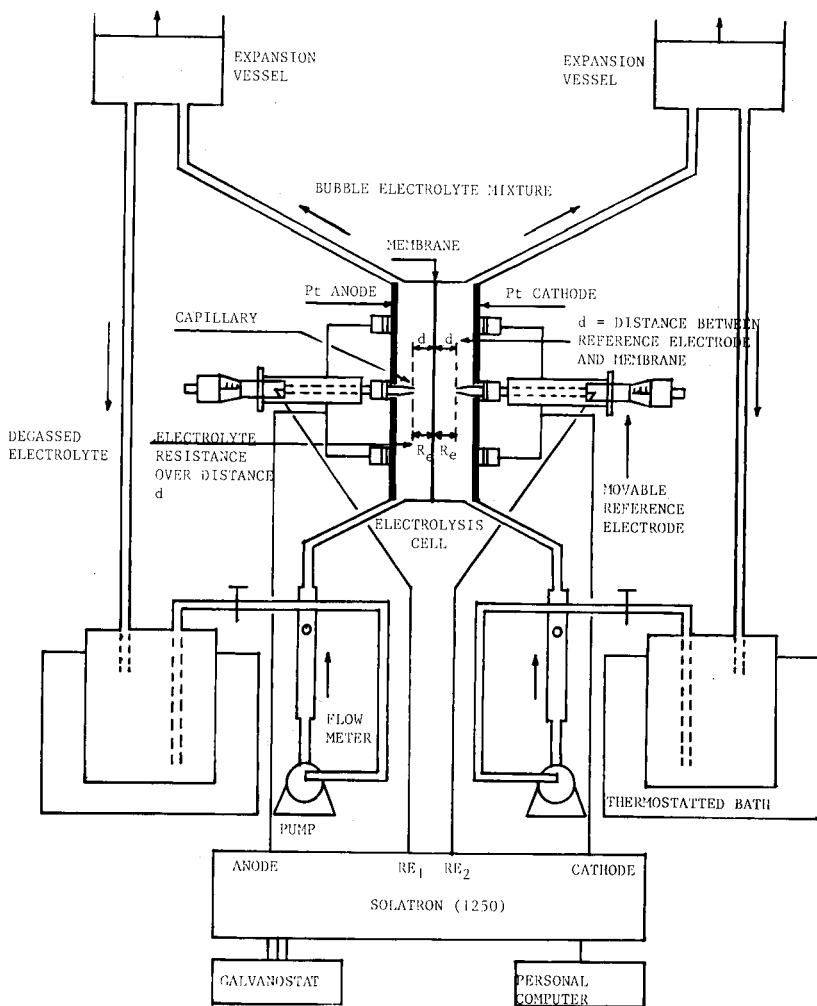
Fig. 7.6 Schematic set-up of the membrane impedance or resistance measuring system.

volumetric flow rate of the thermostatted solution of both compartments
was measured with a calibrated flow meter.

Unless otherwise mentioned, the experiments were carried out galvano-
statically, at atmospheric pressure, 298 K and a solution flow velocity
of 0.1 m s^{-1}.

7.4 Results

7.4.1 Measuring techniques

All experiments were performed by means of a four-electrodes system (cf. Fig. 7.6).
The anode and cathode of the electrolytic cell are the outer electrodes through which an electric current (AC, AC/DC or DC) is passed.
The two adjustable reference electrodes measure the response of this signal in volts.
With this method the electrolyte resistance between the reference electrodes (including the membrane resistance) is measured.
The membrane resistance (or impedance) can be obtained by extrapolating distance d to zero.

7.4.2 Membrane impedance of Nafion 901 measured by AC and AC/DC technique

The concentration polarization is excluded in these two measuring techniques, only the ohmic resistance of the membrane is measured. In other words, these two techniques cannot be applied to measure the total energy losses of a membrane, which are lost during the DC electrolysis.
For comparision purposes both methods are suitable.
In this experiment, two different methods were used to correct for electrolyte resistance:
- extrapolation of the distance between the reference electrode and membrane, d, to zero;
- substracting the calculated electrolyte resistance, R_e.
The electrolyte resistance, R_e, of the solution (24 wt% NaOH plus 1 wt% NaOH), can be calculated by:

$$R_e = \rho \frac{d}{A} \ (\Omega) \hspace{4cm} (7.5)$$

where ρ = the specific resistance of the solution (Ω m), d = the distance between reference electrode and membrane (m) and A = the membrane surface (m^2).
The conductivity, G, of the solution was measured with a conductivity cell with known cell constant (95 m^{-1}). It was found that G = 0.240 (Ω^{-1}) at 296 K, and as ρ was calculated with:

$$\frac{1}{G} = \rho \times 95 \hspace{4cm} (7.6)$$

$$\rho = 4387 \times 10^{-5} \ \Omega \ \text{m}$$

The membrane resistance $R_M = R_d - 2R_e$ (Ω), where R_d = the measured resistance at distance d.

The membrane resistances obtained from the extrapolation and substracting method are tabulated in Table 7.1 and 7.2, respectively.

The results of both methods agree with each other.

About the same membrane resistance was reported for Nafion 901 by the manufacturer (Du Pont), viz. $32 \times 10^{-5} \ \Omega \ \text{m}^2$ in a solution of 24 wt% NaCl plus 1 wt% NaOH, at 296 K.

7.4.3 Membrane resistance of Nafion 901 under industrial conditions, measured by DC technique

Chlor-alkali membrane cells in industry principally consists of an expanded mesh anode (RuO_2/Ti), a perforated plate cathode (mild steel) and a bimembrane (such as, Nafion 901).

The anolyte and catholyte are 180 g/l NaCl ($H^+ \leq 10^{-2}$ M) and 23 wt% NaOH, respectively.

The anode-membrane distance is zero and the cathode-membrane distance is 2 mm. The operating temperature is about 358 K and the solution flow velocity is 0.03 m s^{-1}.

The cell used (cf. Fig. 7.7) in this experiment is almost the same as
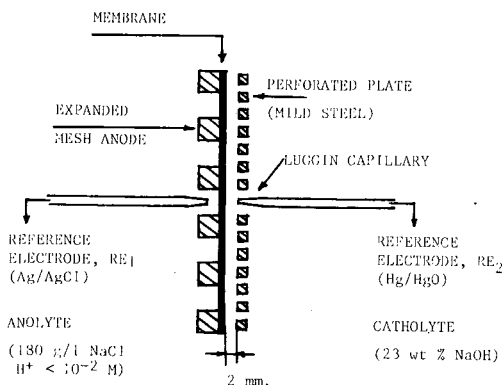
Fig. 7.7 Schematic set-up of an industrial cell.

Distance between reference electrode and membrane, d, in cm	R_{AC} (I = 0.00A) in (Ω)	$R_{AC/DC}$ (I = 0.500A) in Ω
0.8	1.04	1.04
0.7	0.94	0.94
0.6	0.85	0.85
0.5	0.76	0.76
0.4	0.68	0.67
0.3	0.59	0.58
0.2	0.51	0.50
0.1	0.41˙	0.44

Extrapolate d to zero gives.

a) membrane impedance, $R_{AC,M}$ = 0.33 Ω or
   surface impedance, $R'_{AC,M}$ = 33 x 10^{-5} Ω m^2
b) membrane impedance, $R_{AC/DC,M}$ = 0.32 Ω or
   surface impedance, $R'_{AC/DC,M}$ = 32 x 10^{-5} Ω m^2

Table 7.1 Calculation of the membrane impedance by means of extrapolation. R_{AC} (I = 0.000A) and $R_{AC/DC}$ (I = 0.500A) in dependence of d for Nafion 901.

Operating conditions:

Anode and cathode = 10 cm^2 Pt, Reference electrodes R_{E1} and R_{E2} = Pt wire (diameter = 0.5 mm and tip diameter = 1.0 mm), anolyte and catholyte = 24 wt% NaCl plus 1 wt% NaOH, $v_{s,o}$ = 10 cm s^{-1}, T = 296 K and alternating current frequency = 8192 c s^{-1}.

Distance between reference electrode and membrane, d, in cm	R_{AC} (I = 0.000A) in Ω	$R_{AC,M}$ R_{AC} - 2 R_e in Ω	$R_{AC/DC}$ (I = 0.500 A) in Ω	$R_{AC/DC,M}$ = $R_{AC/DC}$ - 2R_e in Ω
0.8	1.04	0.338	1.04	0.338
0.7	0.94	0.326	0.94	0.326
0.6	0.85	0.324	0.85	0.324
0.5	0.76	0,322	0.76	0.322
0.4	0.68	0.330	0.67	0.320
0.3	0.59	0.326	0.58	0.316
0.2	0.51	0.334	.0.50	0.324
0.1	0.41	0.322	0.44	0.352

Average membrane impedance, $R_{AC,M,av}$ = 0.33 Ω or
average surface membrane impedance, $R'_{AC,M,av}$ = 33 10^{-5} Ω m^2
Average membrane impedance, $R_{AC/DC,av}$ = 0.33 Ω or
average surface membrane impedance, $R'_{AC/DC,av}$ = 33 10^{-5} Ω m^2

Table 7.2 Calculation of the membrane impedance by means of electrolyte resistance correction. (The results in Table 7.1 have been used here for the calculation).

described in Fig. 7.6. Only the width of this cell is larger (2.3 cm).
Experimentally, it was found that the ohmic drop of the catholyte, Ca, at
$i = 4 \times 10^{-3}$ A m^{-2} was 40 V m^{-1} and 70 V m^{-1} for the anolyte, An.
In case Nafion 901 was used, the voltage drop across the reference
electrodes, ΔV_{RE}, was 0.90 V, at $i = 4 \times 10^{-3}$ A m^{-2} and the distance
between reference electrode Re$_1$ and membrane = the distance between
reference electrode Re$_2$ and membrane, d, = 2×10^{-3} m.
The membrane resistance is given by:

$$\frac{\Delta V_{RE} - d \ (Ca + An)}{i} \qquad (\Omega \ m^2) \qquad\qquad (7.7)$$

Thus the membrane resistance for Nafion 901 is:

$$\frac{0.90 - 2 \times 10^{-3} \ (40 + 70)}{4 \times 10^3} = 17 \times 10^{-5} \ \Omega \ m^2$$

Under the same industrial conditions, 14×10^{-5} Ω m^2 was found for Nafion
954 and 12×10^{-5} Ω m^2 for Nafion 961.

7.5 Discussion

Measuring errors due to the electric contacts were eliminated by using a
four-electrodes system.
The resistance or impedance measured concerns only the area between both
capillary tips. Reason, why the results obtained are so reliable. It
turned out that the simplest and best way to determine the energy losses
of a membrane under industrial conditions is the DC measuring technique.
The energy losses in and on a membrane can easily be calculated by
measuring the voltage drop across the reference electrodes during
electrolysis.
The voltage drop across the membrane, ΔU_M, can be obtained by
substracting the anolyte and catholyte voltage drop from the voltage drop
across the reference electrodes.
This ΔU_M consists of the membrane potential (including concentration
polarization), $\Delta\phi$, and the membrane ohmic drop, IR$_M$.
The membrane potential can be calculated with Eq. 7.4.
Substituting the bulk activity of Na$^+$ in the catholyte (about 7 M) and
the anolyte (about 3 M) gives:

$$\Delta\phi = 0.059 \log \frac{7}{3} = 0.022 \text{ V}$$

When the surface concentrations are inserted in the equation, an increase
of $\Delta\phi$ is obtained, viz. 0.060 V.

In this calculation, the following assumptions have been made:

- current density is uniform over the entire membrane surface;
- equipotential surfaces in the electrolyte are parallel to the membrane
  surface.

7.6 References

1   Maomi Seko, Akira Yomiyama, Shinsaku Ogawa and Hiroshi Ono in : C.
    Jackson, Modern Chlor-Alkali Technology, Chapter 7, Ellis Horwood
    Limited, Chichester, England 2 (1982)

2   Masao Nagamura, Horishi Ukihashi and Osamu Shiragami in: C. Jackson,
    Modern Chlor-alkali Technology, Chapter 5, Ellis Horwood Limited,
    Chichester, England 2 (1982)

3   Maomi Seko, Hirotsugu Miyauchi, Jukichi Ohmura and Kyoji Komito in:
    C. Jackson, Modern Chlor-alkali Technology, Chapter 6, Ellis Horwood
    Limited, Chichester, England 2 (1982)

4   D.L. Caldwell in : A Comprehensive Treatise on Electrochemistry, Vol.
    2, J.O'M. Bockris, B.E. Conway, E. Yeager and R.E. White, Edo.,
    Plenum Press, New York (1981) 105

5   K.A. Poush, D.L. Caldwell, J.W. van Zee and R.E. White in: C.
    Jackson, Modern Chlor-alkali Technology, Ellis Horwood Limited,
    Chichester, England 2 (1982) 21

6   B.V. Tikal, P.W.T. Lu, J.E. Colman and S. Srinivasan in: A
    Comprehensive Treatise on Electrochemistry, Vol. 2, J.O'M. Bockris,
    B.E. Conway, E. Yeager and R.E. White, Eds., Plenum Press, New York
    (1981) 74

7   T.D. Gierke in: J.O'M. Bockris, B.E. Conway and R.E. White, Modern
    Aspects of Electrochemistry No. 14, Plenum Press, New York and London
    (1982) 425

8   Maomi Seko, Akira Yomiyama, Shin Saku Ogawa and Horishi Ono in: C.
    Jackson, Modern Chlor-alkali Technology, Ellis Horwood Limited,
    Chichester, England 2 (1982) 97

Chapter 8

<div align="center">

Cell voltage during chlor-alkali

membrane cell electrolysis

</div>

8.1 Introduction

The total energy required to produce one metric ton of 50 wt% NaOH, by
membrane electrolysis of NaCl, is approximately 2800 kWh/MT NaOH [1].
About 70% of the total energy is consumed by the electrolysis process
itself and the rest by evaporation and auxiliary processes.
The energy consumption for the electrolysis is given by:

$$\text{Energy consumption} = \frac{n \; F \; U}{3.6 \times 10^4 \times \eta_i \times M} \qquad (\text{kWh kg}^{-1}) \qquad (8.1)$$

where U = the operating cell voltage (V), M = the molecular weight in
kilogram per kmol and η_i = the current efficiency.
At present, high quality membranes with a current efficiency of about
95.5% are commercially available. Further improvement in current
efficiency will be hard to achieve. Reducing membrane resistance is a
more realistic approach for energy reduction. Moreover, the major savings
in energy consumption can be achieved by reducing the cell voltage.
The operating cell voltage consists of the following components:
decomposition voltage (reversible cell voltage, U_r); membrane potential
drop, $\Delta\phi$, (including concentration polarization); membrane ohmic drop,
IR_m; cathode overpotential, η_c; bubble- electrolyte mixture ohmic drop,
IR_e; anode overpotential, η_a, and the so-called structural ohmic drop,
IR_{st} with R_{st} = the resistance of the current feeders and the electric
circuit. Hence, the operating cell voltage is given by:

$$U = U_r + \Delta\phi + IR_m + \eta_c + IR_e + \eta_a + IR_{st} \qquad (8.2)$$

The operating cell voltage is highly dependent on operating conditions
(electrode properties, electrolyte properties, membrane properties,
current density, temperature and pressure) and cell design (structural
drop, gap between the electrodes with membrane position, electrolyte

solution flow velocity and electrode configuration).

A typical voltage breakdown for a membrane cell is shown in Fig. 8.1.
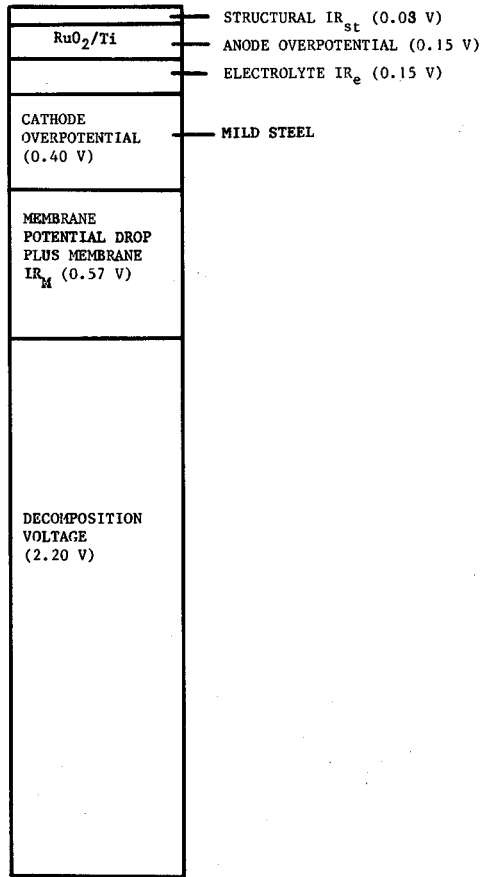
Fig. 8.1 Typical voltage breakdown for a membrane cell (membrane-cathode gap 3 mm). Cell voltage = 3.55 V, at 4 kA m^{-2} and T = 363 K.

For energy reduction purposes, each of these components can be tackled individually. The major component of the cell voltage is the decomposition voltage. It is a thermodynamic quantity and not a kinetic quantity and therefore only sensible for temperature and pressure (can be reduced by increasing the operating temperature and/or pressure). Its value is about 2.20 V, at 363 K and atmospheric pressure. This minimum voltage is required to decompose NaCl and H_2O into Cl_2, H_2 and NaOH. The pressurized operation has the following benefits:

● less and smaller gas bubbles are evolved at the electrodes; hence, bubble–electrolyte mixture resistance decreases;

- reduced membrane vibration and hence reduction of membrane damage;
- reduced water content in chlorine gas, resulting in easier drying of the gas with less heat loss;
- possibility of increasing the operating temperature, resulting in decreasing cell voltage.

Too highly pressurized electrolyzers may cause leakage and other troubles. So, industrial cells are commonly operated at 363 K and 2 ata.
A slightly higher hydrostatic pressure on the catholyte side is recommended because the pressure differential across the membrane immobilizes the membrane and minimizes flutter and vibration which can cause abrasion or flex-fatigue.

The oxygen consuming electrode

The reduction of O_2 instead of H_2O can theoretically reduce the decomposition voltage significantly [2].
The main electrode reaction, at the cathode, is then:

$$O_2 + 2\ H_2O + 4e^- \rightarrow 4\ OH^-\ (E^o = +0.40\ V)$$
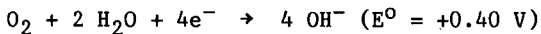
The main electrode reaction, at the anode remains:

$$4\ Cl^- \rightarrow 2\ Cl_2 + 4e^-\ (E^o = +1.36\ V)$$
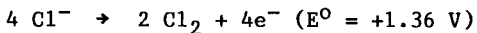
Because the reduction of O_2 occurs at a significantly lower potential than the decomposition of water:

$$4\ H_2O + 4e^- \rightarrow 2\ H_2 + 4\ OH^-\ (E^o = -0.84\ V)$$
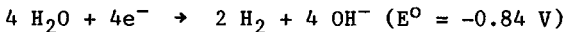
a savings of 1.24 V can be obtained in the electrolysis of brine to produce Cl_2 and NaOH. The oxygen cathode membrane cell is not yet commercially available. Several problems associated with the use of a polymer-bonded catalytic electrode have to be solved. Of course, in this case no H_2 is produced.
It is clear that energy savings can be achieved by reducing the membrane voltage, the cathode overpotential, the bubble-electrolyte ohmic losses, the anode overpotential and structural losses.
After ample considerations, we decided to focus our attention on:

- commercially available Nafion membranes (finite and zero gap membrane);
- the electrode gap;
- the electrode configuration.

The first two items will be treated in this Chapter and the last one in Chapter 9.

In Section 8.2, the experimental set-up for the determination of the behaviour of finite and zero gap membranes under industrial conditions is described. The results obtained are presented in Section 8.3. The results are discussed and explained in Section 8.4.

8.2 Experimental

8.2.1 Determination of characteristics of Nafion 901 (finite gap membrane) and Nafion 961 (zero gap membrane)

Finite gap membranes have a surface with hydrophobic properties which favours the adhesion of gas bubbles. Due to this properties the electrode gap cannot be reduced to a minimum ("zero gap"). This undesirable effect can be eliminated by enhancing the hydrophilicity of the membrane surface. The so obtained membrane is called "zero gap" membrane.

The same electrolytic cell as described in Section 7.4.3 and Fig. 7.7 was used (two equal compartments, each 2.3 cm wide, 1 cm deep and 10 cm high). The solution flow circuit used was the same as shown in Fig. 7.6.

For cell voltage measurements, the DC current was adjusted galvanostatically (Delta Electronika DO50-10) and the cell voltage was measured by an automatic multimeter (PM 2519 Philips).

All experiments were performed under conditions as also current in industry, i.e.:

- expanded-unrolled mesh anode (Ti/RuO_2) (cf. Fig. 9.2.A);
- perforated plate cathode (mild steel) (cf. Fig. 9.3.A);
- anolyte 180 g/l $NaCl([H^+] < 10^{-2}$ M, to prevent membrane damage and to ensure optimum performance and long lifetime of membranes); the impurities in the anolyte may not exceed recommended limits (for example: Ca^{2+} plus $Mg^{2+} < 50$ ppb, $Sr^{2+} < 0.5$ ppm, $Ba^{2+} < 1.0$ ppm, $Na_2SO_4 < 7$ g/l, $J_2 < 0.4$ ppm, aluminum/silica < 0.1 ppm, $NaClO_3 < 20$ g/l, etc. [3]);
- double-layer membrane (Nafion 901 or 961);

- catholyte 23 wt% NaOH;
- current density 4 kA m^{-2};
- temperature 358 K;
- pressure 101 kPa;
- solution flow velocity 0.03 m s^{-1};
- membrane–anode distance 0 mm;
- membrane–cathode distance 2 mm.

8.3 Results

The effect of the electrode gap on the cell voltage for Nafion 901 (finite gap membrane) and Nafion 961 (zero gap membrane) is shown in Fig. 8.2.
The curves show that the cell voltage for a finite gap membrane (Nafion 901) has a minimum between 1 and 2 mm, while the cell voltage for a zero gap membrane (Nafion 961) increases with gap distance.
Fig. 8.3 shows the cell voltage as a function of current density for both Nafion membranes.
The results obtained indicate that the cell voltage for both membranes decreases with decreasing current density from 5 to 2 kA m^{-2}.

8.4 Discussion

If the electrode gap is narrowed, the cell voltage decreases because of reduced electrolyte ohmic drop.
When, for a finite gap membrane, the electrode gap becomes smaller than 1.5 mm, the evolved gas bubbles attached to the membrane surface cannot be easily removed from the membrane surface due to the hydrophobic properties of the membrane surface which favour the adhesion of gas bubbles.
Consequently, the cell voltage increases with decreasing electrode gap (cf. Fig. 8.2, Nafion 901).
The zero gap membrane, Nafion 961, is designed to avoid bubble adhesion of H_2 gas bubbles at the membrane surface by increasing the hydrophilicity of the surface. So, with this membrane gas bubbles are removed more easily from the membrane surface.
Consequently, the cell voltage decreases with decreasing electrode gap distance, even below 1.5 mm (cf. Fig. 8.2, Nafion 961).
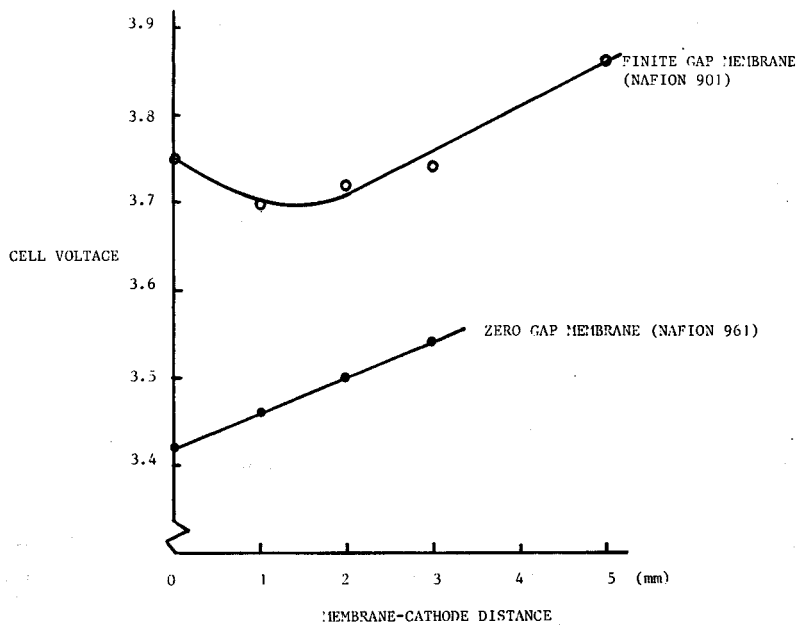
Fig. 8.2 The effect of gap on the cell voltage for Nafion 901 and 961.
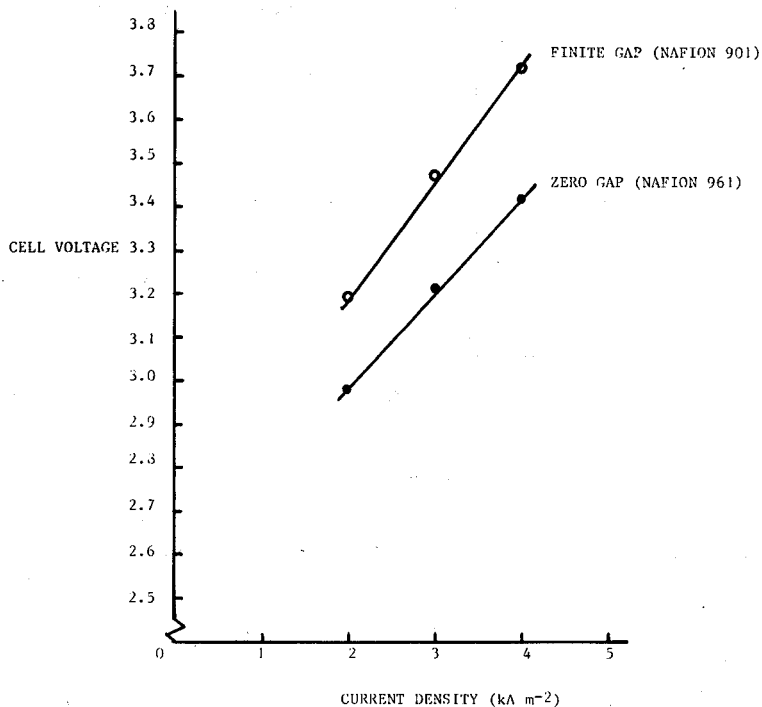
Fig. 8.3 The cell voltage as a function of current density for Nafion 901 and 961.

From the results obtained, it can be concluded that the optimum cell voltage for a finite gap membrane occurs at an electrode gap of approximately 1.5 mm and for a zero gap membrane at an electrode gap of 0 mm.

The zero gap membrane has two advantages compaired with a finite gap membrane:

● the electrolyte resistance is practically eliminated;
● the cell voltage increases slower with increasing current density (cf. Fig. 8.3), probably caused by the high hydrophilicity of the membrane surface.

8.5 References

1   Bulletin of E.I. du Pont de Nemours & Co (Inc.) Polymer Products Department, Wilmington, DE 19898, U.S.A. (E-47765, 8/83)
2   E. Yeager and P. Bindra, Chem. Ing. Techn. 52 (1980) 384
3   Users Guide of E.I. de Pont de Nemours & Co (Inc.) Polymer Products Deparment, Wilmington, DE 19898, U.S.A. (E-63122 6/85)

Chapter 9

Electrode shapes of the electrolysis cell

9.1 Introduction

The electrode shape is very important for gas-evolving electrodes; it is one of the factors determining the cell voltage, because of its influences, in a direct or indirect way:
- the membrane potential and membrane ohmic resistance;
- the cathode overpotential;
- the bubble-electrolyte mixture ohmic resistance;
- the anode overpotential.

An electrode shape is optimal, if it satisfies the following basic features:
- imposes a uniform current density on the membrane, resulting in a minimum membrane ohmic resistance;
- has a large active surface area, which decreases the current density, and, consequently, decreases the electrode overpotential;
- rapidly releases the gas bubbles generated on the electrodes to the rear of electrodes, so that the effect of gas bubbles on the bubble-electrolyte mixture resistance can be minimized;
- masks a minimum amount of membrane area (the masked membrane surface is inactive, due to the lack of electrolyte supply), or has a maximum per cent open area, i.e. for a perforated plate electrode is given by $n \pi r^2/wh \times 100\%$ where n = the number of holes, r = the radius of the perforation, w = the width of the electrode and h = the height of the electrode (cf.9.3.A);
- introduces high turbulence at the surface of the membrane and the electrode; hence, reduces the Nernst diffusion layer at the membrane surface, thereby increasing the limiting current density and also avoiding gas bubble blinding effects on the electrode surface;
- avoids membrane damage by abrasion.

So, by using the optimal electrode design, it is possible to reduce cell voltage and so power consumption of the membrane chlor-alkali cell (cf. Fig. 9.1) with a minimum of investment. Till now, no explicit theory exists to describe the effects of an electrode shape on the cell voltage.

For the time being, the most economical way to achieve our goal is to determine experimentally the effects of different cathode and anode shapes of the same material on the cell voltage.

The cell studied is a finite gap cell (cf. Fig. 9.1.A). It consists of an expanded-unrolled mesh (RuO_2/Ti) anode (cf. Fig. 9.2.A), a perforated plate mild steel cathode (cf. Fig. 9.3.A) and a bimembrane (such as, Nafion 901 or 961).

A selection was made from commercially available electrode shapes, which appeared to meet the above mentioned basic requirements. The selection was also screened on the basis of costs (the existing electrode materials were used, only the electrode shapes were different).

In Section 9.2, the experimental set-up for the determination of the cell voltage is described. In Section 9.3, the results obtained are presented. The results are discussed and explained in Section 9.4.

9.2 Experimental

The cell used (cf. Fig. 9.1 A and B) in this test is almost the same as that shown in Fig. 7.6 (two equal compartments, each 2.3 cm wide, 1 cm deep and 10 cm high).

The solution flow circuit used was the same as depicted in Fig. 7.6.

For cell voltage measurements, the dc current was adjusted galvanostatically (Delta Electronika D050-10) and the cell voltage was measured by an automatic multimeter (PM 2519 Philips).

All experiments were carried out under the conditions summarized in Section 8.2.1.

9.3 Results

To determine the optimum electrode pair configuration, four anodes (cf. Fig. 9.2) and three cathodes (cf. Fig. 9.3) of different shapes were selected on the basis of costs and availability criteria.

The results in Table 9.1 indicate that the lowest cell voltage for finite gap membrane cells is obtained by using a lamellar with rounded flat profile DSA anode (cf. Fig. 9.2.D) and a coarse perforated plate mild steel cathode (cf. Fig. 9.3.B).

The same electrode combination gives also a very low cell voltage for zero gap membrane cell. But the lowest cell voltage is obtained by both
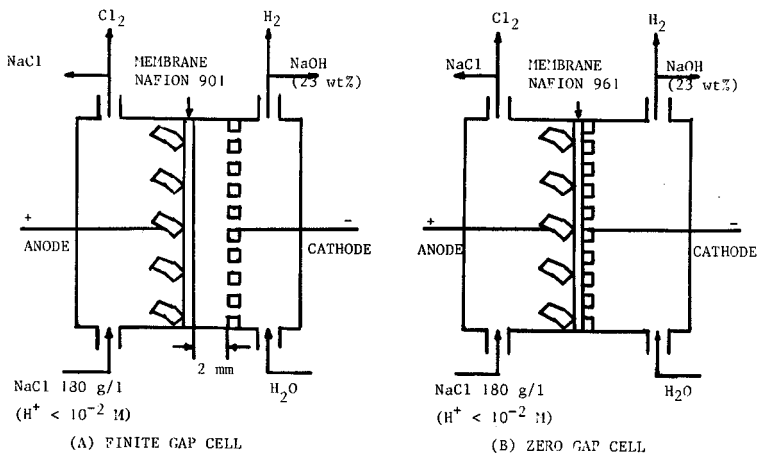
Fig. 9.1 Schematic set-up of (A) the finite gap cell with nafion 901 and (B) the zero gap cell with nafion 961.

Anode: expanded-unrolled mesh (RuO_2/Ti).

Cathode: perforated plate (mild steel).

$T = 358$ K, $P = 1$ kPa, $v_s = 0.03$ m s^{-1} and $i = 4$ kA m^{-2}.

electrodes consisting of a lamellar rounded flat profile (cf. Table 9.2).

9.4 Discussion

Experimentally, it was found that the cell voltage of the membrane cell with i = 4 kA m^{-2} and T = 358 K, increases linearly with increasing distance between electrode and membrane in the distance range from 0 to 3 mm. For both anode and cathode shifting, the cell voltage increases with 0.07 V/mm and 0.04 V/mm, respectively.

To determine the impact of the gas bubbles on the electrolyte resistance, the conductivities of both the anolyte and catholyte were measured with a conductivity cell (Philips PW 9517) with a known cell constant (28.2 cm^{-1}) and an impedance meter (Solartron 1250).

It was found that the specific resistance of the anolyte (without bubbles) was ρ_a = 2.00 Ω cm, and the specific resistance of the catholyte, ρ_c = 1.00 Ω cm, both at T = 358 K.

Hence, the ohmic drop for 1 mm anolyte and catholyte is 0.08 V and 0.04 V, respectively.

From the results obtained, it can be concluded that the contribution of the gas bubbles to the electrolyte ohmic resistance under chosen

EXPANDED-UNROLLED MESH DSA ANODE

DIMENSION IN MM

	A	B
w	23.0	23.0
h	100.0	100.0
a	4.2	2.1
b	3.0	1.1
c	8.9	4.0
t	2.9	1.2

EXPANDED-FLATTENED MESH DSA ANODE

DIMENSION IN MM

	C
w	23.0
h	100.0
a	2.8
b	3.2
c	7.2
t	1.0

LAMELLAR WITH ROUNDED FLAT PROFILE DSA ANODE

DIMENSION IN MM

	D
w	23.0
h	100.0
a	2.5
b	2.5
t	6.5

PER CENT OPEN AREA >43%
INTERIOR SURFACE AREA 7900
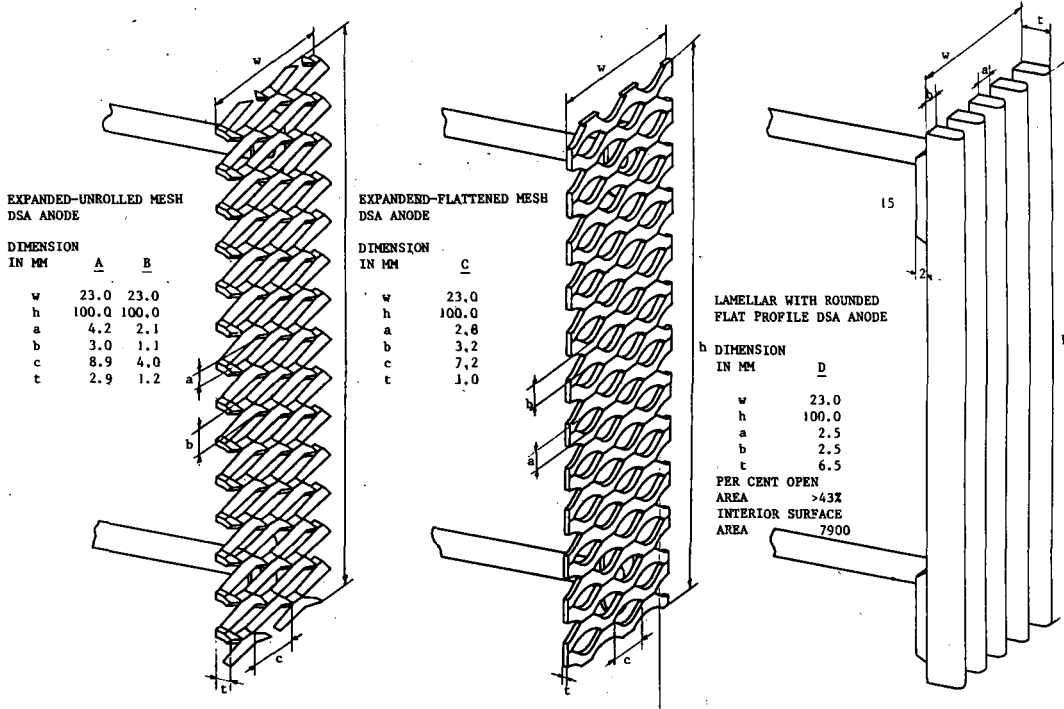
Fig. 9.2 Four different anode shapes.

PERFORATED PLATE MILD STEEL CATHODE

DIMENSION IN MM

	A	B
w	23.0	23.0
h	100.0	100.0
a	1.1	2.9
b	1.2	2.0
t	1.0	1.0
q	2.0	4.2

NUMBER HOLES 502 100

PER CENT OPEN AREA 21% 29%

INTERIOR SURFACE AREA (mm^2) 1735 911

EQUILATERAL TRIANGLE

LAMELLAR WITH ROUNDED FLAT PROFILE MILD STEEL CATHODE

DIMENSION IN MM

	C
w	23.0
h	100.0
a	2.5
b	2.5
t	6.5

PER CENT OPEN AREA > 43%

INTERIOR SURFACE AREA (mm^2) 7900
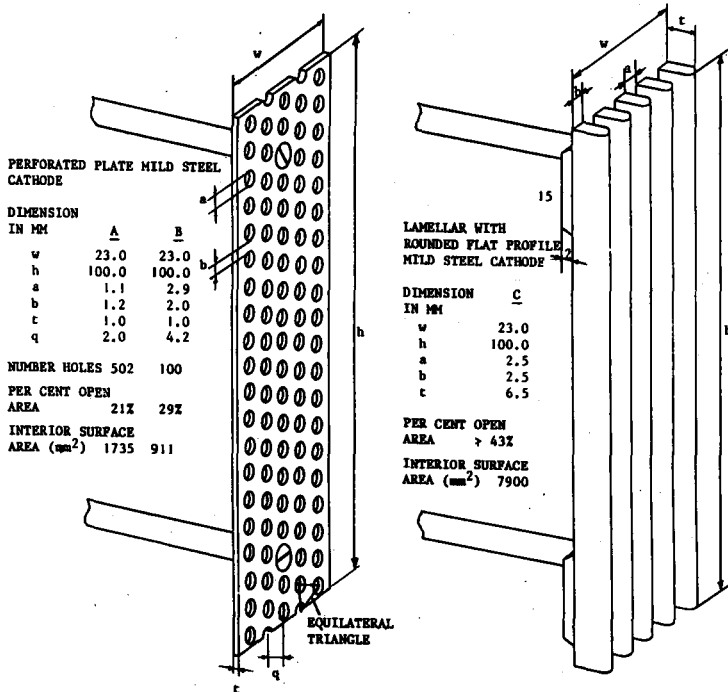
Fig. 9.3 Three different cathode shapes.

	CATHODE	
	Fine perforated plate (mildsteel). Diameter perforation = 1.1 mm. Number holes = 502 Plate thickness = 1.0mm (cf. Fig. 9.3.A)	Coarse perforated plate (mildsteel). Diameter Perforation = 2.9 mm. Number holes = 100 Plate thickness = 1.0mm (cf. Fig. 9.3.B)
Coarse expanded-unrolled mesh (RuO_2/Ti) (cf. Fig. 9.2.A)	(3.71 - 3.71) = 0.00 V	(3.71 - 3.60) = -0.11 V
Fine expanded unrolled mesh (RuO_2/Ti) (cf. Fig. 9.2.B)	(3.71 - 3.60) = -0.11 V	
Coarse expanded flattened mesh (RuO_2/Ti) (cf. Fig. 9.2.C)	(3.71 - 3.65) = -0.06 V	
Lamellar with rounded plate profile (RuO_2/Ti) (cf. Fig. 9.2.D)	(3.71 - 3.53) = -0.18 V	(3.71 - 3.48) = -0.23 V

(ANODE label on left side of table)

Table 9.1 Increase (+) or decrease (-) of finite gap cell voltage (cf. Fig. 9.1.A) obtained from different electrode shapes in comparison with the existing industrial cell, which has an expanded-unrolled mesh RuO_2/Ti anode (cf. Fig. 9.2.A) and a perforated plate mild steel cathode (cf. Fig. 9.3.A). The membrane used was a finite gap membrane Nafion 901.

	CATHODE		
	Fine perforated plate (mildsteel) Diameter perforation=1.1 mm. Number holes =502 Plate thickness = 1.0 mm (cf. Fig. 9.3.A)	Coarse perforated plate (mildsteel) Diameter perforation = 2.9 mm. Number holes =100 Thickness = 1.0 mm (cf. Fig. 9.3.B)	Lamellar with rounded flat profile (mildsteel) (cf. Fig.9.3.C)
Coarse expanded-unrolled mesh (RuO_2/Ti) (cf. Fig. 9.2.A)	(3.42 - 3.42) = 0.00 V	(3.42 - 3.32) = -0.10 V	(3.42 - 3.27) = -0.15 V
Lamellar with rounded flat profile (RuO_2/Ti) (cf. Fig. 9.2.D)	(3.42 - 3.29) = -0.13 V	(3.42 - 3.21) = -0.21 V	(3.42 - 3.19) = -0.23 V

(ANODE label on left side of table)

Table 9.2 Increase (+) or decrease (-) of zero gap cell voltage (cf. Fig. 9.1.B) obtained from different electrode shapes in comparison with the existing industrial cell. The membrane used was a zero gap membrane Nafion 961.

conditions is neglible. In other words, the chosen electrodes are able to release the gas bubbles generated on the electrode very rapidly to the rear of the electrodes.

The results in Table 9.2 show that the cell voltage decreases further with 0.15 V, if the existing fine perforated plate mild steel cathode is replaced by a lamellar rounded flat profile mild steel cathode.

This extra reduction could be achieved, due to the following benefits of the lamellar cathode:

- the per cent open area is quite high, viz. $>$ 43% (cf. Fig. 9.3.C), consequently, the generated gas bubbles at the cathode can be easily removed to the rear of the electrode; additionally, a high per cent open area means that only a small amount of membrane surface area is masked by the electrode; so, the membrane ohmic resistance, R_m, decreases according to $R_m = \rho_m \times 1/A$ where ρ_m = the specific membrane resistance (Ω cm), 1 = the thickness of the membrane (cm) and A = the unmasked membrane surface area (cm^2);

- it generates high turbulence at the surface of the membrane and electrode; hence, reduces the membrane potential, the cathode diffusion overpotential and the gas bubble masking effects on the electrode surface;

- has a large active surface area of about 7900 mm^2 (1735 mm^2 for fine perforated plate electrode); consequently, the cathode overpotential decreases.

Replacing the used coarse expanded-unrolled mesh (RuO_2/Ti) anode by a lamellar with rounded flat profile (RuO_2/Ti) anode, the cell voltage decreases with 0.13 V (cf. Table 9.2). The already mentioned arguments can also be used to explain this decrease.

The results in Table 9.2 indicate that the coarse, perforated plate mild steel cathode gives a lower cell voltage than the fine, perforated plate cathode of approximately 0.10 V.

Comparing the data for both electrodes, it can be concluded that (cf. Fig. 9.3 A and B) that the coarse perforated plate has a higher per cent open area than the fine perforated plate, viz. 29% and 21%, respectively. This higher per cent open area has the benefit of masking less the membrane surface. The masked membrane surface is inactive, due to the lack of electrolyte supply to this area. Hence, a higher per cent open area reduces the membrane ohmic resistance. It can be calculated that the interior surface area of this coarse perforated plate is lower than that

of the fine perforated plate, viz. 911 mm^2 and 1735 mm^2, respectively. A low interior surface area is a disadvantage for the cell voltage, because the electrolysis occurs mainly at the interior surface area of electrode holes. Nevertheless, the coarse perforated plate cathode gives a lower cell voltage of about 0.10 V. So, it appears that the per cent open area is a predominant factor for cell voltage. So, the perforated plate mild steel cathode used in the common industrial cells is not an ideal one (cf. Fig. 9.3.A).

Based on physical arguments (cf. Section 9.1) and experimental results (cf. Table 9.2), it can be stated that a perforated plate cathode for a zero gap cell is optimal, when it has a optimum per cent open area and interior surface area.

To determine the optimum shape of a perforated plate, we suppose a perforated plate with width, w, height, h, thickness, t, number of perforations, n, and radius perforation, r.

The total surface area, A, is given by:

$$A = w\ h - n\ \pi\ r^2 + n\ 2\pi\ r\ t \qquad\qquad (1)$$

The second term on the righthand side represents the open area and the third term represents the interior surface area of the perforations.

The minimum increase of A is obtained by differentiating Eq. (1) to n with dA/dn = 0, and r and t constant. Then r = 2t.

The maximum increase of A is obtained by differentiating Eq. (1) to r with dA/dr = 0, and n and t constant.

Then r = t.

Inserting r = 2t and r = t, respectively into Eq. (1) gives:

$$A(r = 2t) = w\ h \qquad\qquad (2)$$
$$A(r = t) = w\ h + n\ \pi\ t^2 \qquad\qquad (3)$$

Hence, the optimum criteria for a perforated plate are satisfied, if r = t.

The present perforated plate cathode used in the industry has a thickness of 1.0 mm and the distance between two adjacent perforations is kept on a minimum of 1.2 mm for mechanical strength purpose. This means that the number of holes is limited by the mechanical strength of the plate.

It can be shown that a perforated plate of w = 23.0 mm, h = 100.0 mm and

t = 1.0 mm has an optimum shape if:

- r = 1.0 mm;
- per cent open area = 39.3%;
- interior surface area = 1809 mm^2;
- number of holes = 288.

This ideal perforated plate (cf. Fig. 9.4) is expected to have an outstanding performance.
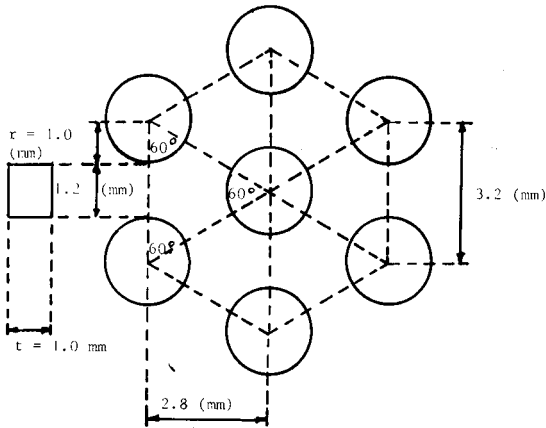
Fig. 9.4 Optimum perforated plate mild steel cathode thickness plate, t, = 1.0 mm.
        Radius perforation, r, = 1.0 mm.
        Distance between two adjacent circles = 1.2 mm.
        Number of holes per 2300 mm^2 = 283.

Chapter 10

Final conclusions for cell voltage reduction;
suggestions for further research

10.1 Final conclusions

From this study, it can be concluded that the power consumption of the
existing chlor-alkali membrane cell process can be reduced significantly.
The results obtained (cf. Chapter 8 and 9) enable us to make the
following recommendations for power savings to be achieved with a minimum
of investment costs.
The recommendations below are listed in sequence of increasing investment:

1. Replace membrane Nafion 901 by 961.
2. Replace the existing fine perforated plate mild steel cathode by a
   coarse perforated plate mild steel cathode (cf. Fig. 9.3.B) or by a
   lamellar with rounded flat profile mild steel cathode (cf. Fig.
   9.3.C).
3. Replace the existing coarse expanded-unrolled mesh DSA (dimensionally
   stable anode) anode by a lamellar with rounded flat profile DSA anode
   (cf. Fig. 9.2.D).
4. Replace both existing electrodes by lamellar rounded flat profile
   electrodes.
5. Change from finite gap cell operation into zero gap cell operation.

The results in Tables 9.1 and 9.2 show that cell voltage reductions
obtained range from about 100 to even 230 mV. It follows that this
voltage reduction, at a production level of 200,000 ton Cl_2 per year and
a energy price of ƒ 0.10 per kWh, results in cost savings ranging from ƒ
1000,000 to ƒ 3000,000 per year.

10.2 Suggestions for further research

Chapter 3, 4 and 5 have tried to explain the observed behaviour of the
electrolysis bubbles with the slow bubble growth models. The main
tendencies observed appear consistent with the mechanics of cavity

bubbles but there are still a number of observations which cannot be explained with the present models.

For a better understanding of the electrolysis bubbles behaviour further research is required concerning the electrolysis bubble growth and its consequences for the mass transfer.

In conclusion, the lowest cell voltage obtained for the chlor-alkali process is about 3.19 V (cf. Table 9.2).

The theoretical cell voltage is approximately 2.20 V. This means that there are still possibilities for further improvement.

In this study an effort has been made to develop a theory for the determination of the optimum shape of a perforated plate electrode. Additional experiments are required for the development of a more quantitative theory. In this context, the determination of the effect of the thickness of the perforated plate electrode on the cell voltage may help to improve the proposed model.

So, the following investigations are suggested for further improvement of the cell voltage:

1. Check the validity of the proposed theory concerning the optimum shape of a perforated plate (cf. Section 9.4); extend of the theory to more complex electrode shapes.
2. Determine the effects of the thickness of the electrode on the cell voltage.

Acknowledgement

List of symbols and SI-units

a_i	constants ($i = 1-7$) in the relationships:	$(-)$

$$(1) \quad y = a_i \cdot i_b^{\,n_i}$$

$$(2) \quad y = a_i \cdot 10^{\,\frac{n_i}{T}}$$

A_c	cross-section of the cell	(m^2)
$A_{d,av}$	average cross-section of detached-bubbles	(m^2)
A_e	surface are of the electrode	(m^2)
$c_g^{\,\sigma}$	concentration of dissolved gas at the electrode surface	(kg/m^3)
$c_i^{\,\sigma}$	concentration of ion i at membrane surface	(kg/m^3)
$c_g^{\,s}$	saturated concentration of dissolved gas in the bulk solution at atmospheric pressure 101kPa	(kg/m^3)
$\bar{c}_g$	average concentration of dissolved gas in the vicinity of gas bubble adhering to the electrode	(kg/m^3)
$c_g^{\,\sigma}/c_g^{\,s}$	degree of supersaturation of dissolved gas	$(-)$
Δc_x	supersaturation concentration of dissolved gas, at a distance x perpendicular to the electrode surface	(kg/m^3)
Δc^{σ}	supersaturation concentration of dissolved gas, at the electrode surface; $\Delta c^{\sigma} = c_g^{\,\sigma} - c_g^{\,s}$	(kg/m^3)
C_{bu}	a function of the volumetric gas production rate in Eq. 6.8	$(-)$
d	(1) bubble population density	(m^{-2})
	(2) distance between anode and cathode	(m)
d_i	bubble population density for picture i	(m^{-2})
d_{wm}	distance between working electrode and membrane	(m)
D	diffusion coefficient	(m^2/s)
D_g	diffusion coefficient of dissolved gas	(m^2/s)
D_i	diffusion coefficient of species i	(m^2/s)
E	electrode potential	(V)
E_{eq}	electrode equilibrium potential	(V)
E^O	standard electrode potential	(V)
$E_{eq}^{\,A}$	anode equilibrium potential	(V)

E_{eq}^C	cathode equilibrium potential	(V)
f	gas void fraction	(–)
f_b	gas void fraction in the bulk electrolyte	(–)
f_o	gas void fraction at the electrode surface	(–)
F	Faraday constant (96487×10^3)	(C/keq)
g	gravitational acceleration	(m/s^2)
ΔG	Gibbs' free enthalpy change	(J/kmol)
ΔG^o	standard Gibbs' free enthalpy change	(J/kmol)
h	electrode height from the bottom of the electrode	(m)
H	total electrode height	(m)
ΔH	enthalpy change	(J/kmol)
ΔH^o	standard enthalpy change	(J/kmol)
i	current density	(A/m^2)
i_b	current density used for gas in bubbles	(A/m^2)
i_g	current density used for total gas evolution	(A/m^2)
i_h	current density at electrode height, h	(A/m^2)
i_o	exchange current density	(A/m^2)
i_{av}	average current density	(A/m^2)
I	current	(A)
Ja	Jacob number; $Ja = (\overline{c}_g - c_g^s)/\rho_g$	(–)
k_g	mass transfer coefficient of the dissolved gas	(m/s)
k_i	mass transfer coefficient of the indicator ion i at forced convection	(m/s)
$k_{f,i}$	mass transfer coefficient of the indicator ion i at forced convection in absence of gas bubble evolution	(m/s)
K	(1) gas effect parameter	(–)
	(2) Henry's constant	(m^2/s^2)
K_i	empirical constant	(–)
M	molecular weight	(kg/kmol)
n	(1) number of electrons, involved in the electrode reaction to form one molecule of a species	(keq/kmol)
	(2) number of bubbles on a part of a moving film	(–)
n_i	exponential constants (i = 1–7) in the relationships	(–)

$$(1) \quad y = a_i \, i_b^{n_i}$$

$$(2) \ y = a_i \ 10^{\frac{n_i}{T}}$$

p(H$_2$O)	partial water vapour pressure	(N/m^2)
p(g+H$_2$O)	sum of the partial pressure of gas plus water vapour	(N/m^2)
ΔP	equilibrium gas pressure in a cavity corresponding to the degree of supersaturation at the wall	(N/m^2)
R	(1) universal gas constant	(J/kmolK)
	(2) resistance	(Ω)
R'	surface resistance	(Ωm^2)
R$_a$	average attached–bubble radius for n frames	(m)
R$_c$	average active cavity mouth radius	(m)
Re	Reynolds number	(–)
R$_e$	resistance of the bubble–electrolyte mixture	(Ω)
R$_f$	bubble foot radius	(m)
R$_m$	membrane ohmic resistance	(Ω)
R$_p$	resistance of the pure electrolyte	(Ω)
R$_S$	average Sauter radius of attached–bubbles for n frames	(m)
R$_{a,i}$	average attached–bubble radius for picture i	(m)
R$_{d,i}$	radius of detached–bubble i	(m)
R$_{m,i}$	radius of the biggest attached–bubble on picture i	(m)
R$_{S,d,av}$	average Sauter bubble radius	(m)
R$_{st}$	resistance of the current feeders and electric circuit	(Ω)
(R$_d{}^2$)$_{av}$	average of the square of the of the bubble radii	(m^2)
(R$_d{}^3$)$_{av}$	average of the third power of the bubble radii	(m^3)
s	(1) average degree of screening by attached–bubbles	(–)
	(2) slip ratio; s = v_g/v_s	(–)
s$_i$	degree of screening of the electrode by attached–bubbles for frame i; i.e. the fraction of the electrode surface covered by projection of the bubbles	(–)
s(x)	average degree of screening of the electrode at a distance x from the electrode by attached–bubbles	(–)
s$_i$(x)	degree of screening of the electrode at a distance x from the electrode by attached–bubbles for frame	(–)

	i at o < x < $2R_{m,i}$, i.e. the fraction of the electrode surface, covered by the projection at a distance x from the electrode by attached-bubbles	
ΔS	entropy change	(J/kmolK)
ΔS^o	standard entropy change	(J/kmolK)
t	(1) time	(s)
	(2) electrode thickness	(m)
t_i	transport number of ion i in the electrolyte	(-)
$t_{i,m}$	transport number of ion i in the membrane	(-)
T	temperature	(K)
U	operating cell voltage	(V)
U_r	reversible cell voltage (decomposition voltage)	(V)
U^o	(1) standard emf of the cell reaction; $U^o = -\Delta G^o/nF$	(V)
	(2) reversible cell voltage	(V)
v_i	rate of oxidation or reduction of indicator ion i	(kmol/s)
v_g	actual bubble velocity	(m/s)
v_s	actual solution flow velocity	(m/s)
$v_{g,b}$	practical gas bubble production rate	(m/s)
$v_{g,o}$	superficial gas velocity (theoretical production rate of gas bubble when all the gas is evolved as bubbles)	(m/s)
$v_{s,o}$	superficial solution flow velocity	(m/s)
V_m	molar gas volume	(m^3/kmol)
$V_{g,o}$	volumetric gas production rate	(m^3/s)
$V_{s,o}$	volumetric solution flow rate	(m^3/s)
w	electrode width	(m)
x	distance from the electrode surface	(m)
y	arbitrary physical quantity; unit depending on specific quantity	(-)

Greek symbols

α	charge transfer coefficient	(-)
β	a growth parameter	(-)
δ	(1) thickness of the bubble layer near the electrode	(m)

	(2) thickness of Nernst diffusion layer	(m)
δ_a	thickness of the stagnant bubble layer at the anode	(m)
δ_c	thickness of the stagnant bubble layer at the cathode	(m)
δ_g	diffusion layer of the gas evolved	(m)
δ_i	diffusion layer of the indicator ion	(m)
$\delta_{v,bu}$	modified thickness of the velocity boundary layer	(m)
η	(1) electrode overpotential; $\eta = E - E_{eq}$	(V)
	(2) viscosity of the solution	(kg/m s)
η_b	efficiency of gas bubble evolution; $\eta_b = v_{g,b}/v_{g,o}$	(–)
η_i	current efficiency	(–)
λ_s	specific conductivity of the solution	$(\Omega^{-1}m^{-1})$
ν	kinematic viscosity	(m^2/s)
ρ	specific ohmic resistance	(Ωm)
ρ_g	gas density	(kg/m^3)
ρ_p	specific ohmic resistance of the pure bulk solution	(Ωm)
ρ_s	solution density	(kg/m^3)
σ	surface tension	(N/m)
ϕ	(1) potential	(V)
	(2) contact angle between the bubble and the wall	(degree)
ϕ_o	natural contact angle between the bubble an the wall	(degree)
$\Delta\phi$	membrane potential	(V)
ω	detached–bubble frequency	$(m^{-2}s^{-1})$

Summary

Subject of this study are the energy aspects of the chlor-alkali membrane cell electrolysis, i.e. to reduce power consumption of the existing electrolysis system with a minimum of investment. To achieve this goal, the impact of gas bubbles involved and other process parameters on the cell voltage have been investigated.

Special attention was given to minimize the negative and to maximize the positive effects of gas bubbles on the cell voltage by using appropriate electrode shapes and membrane.

The bubble behaviour was studied by means of a high-speed camera and the gas void fraction was determined by a new technique.

A technique was developed to measure the membrane energy losses.

The relations obtained between the cell voltage and the different process parameters enable us to predict the best settings of the process parameters, to obtain the minimum energy consumption at a given chlorine production.

Chapter 2 presents some historical and recent background information of the electrolysis process, including a pertinent literature review.

The effects of different cell components on the operating cell voltage is discussed.

In Chapter 3, the experimental set-up to determine the attached-bubble behaviour for a chlorine-evolving transparent platinum electrode is described.

The bubbles on the transparent electrode were filmed with a high-speed camera and the bubble parameters assigned after analysis with a motion analyzer.

It has been found that the bubble population density and the attached-bubble radius increases, respectively decreases with increasing current density. These results were explained with the slow bubble growth theory.

Chapter 4 describes the technique for measuring the supersaturation of dissolved gas in the solution near the electrode surface at forced convection.

The method is based on the determination of the efficiency of gas bubble evolution via the mass transfer coefficient of an indicator ion moving towards the gas-evolving electrode.

The degree of supersaturation of hydrogen and oxygen, respectively, increases with increasing current density. At $i_o > 1$ kA m^{-2}, the degree

of oxygen supersaturation tends to level out, perhaps because of coalescence. The degree of supersaturation of chlorine shows independency in the current density range investigated.

Supersaturation concentration values of chlorine are not available in literature and are presented here for the first time.

The method used to measure the bubble departure parameters and the efficiency of gas bubble evolution for a chlorine-, a hydrogen-, and an oxygen-evolving wire electrode under semi-industrial conditions is described in Chapter 5.

Experimentally, it was found that:

- the bubble departure radius increases with increasing current density (the opposite trend to that noted in Table 3.1);
- at the same rate of volumetric gas bubble evolution the bubble size increases in sequence of H_2, O_2 and Cl_2.

These two results cannot be explained with the existing theory. It was also found that the efficiency of bubble evolution decreases in sequence of H_2, O_2 and Cl_2. This phenomenon could be explained in term of the three-phase boundary theory.

A new experimental technique for the determination of the gas void fraction and its distribution in a semi-industrial cell (50 cm high), consisting of two vertical flat-plate electrodes, is described in Chapter 6. The gas void fraction behaviour for electrogenerated chlorine, hydrogen and oxygen shows practically the same trend. These trends confirm earlier reports. The results obtained here are valid for vertical flat-plate gas-evolving electrodes and not for electrodes commonly used in industrial chlor-alkali membrane electrolyzers, because industrial electrodes permit rapid bubble release to the rear of electrodes so that no bubbles accumulation can take place between the inter-electrode gap. Hence, the negative bubble effects are minimized.

In Chapter 7, the newly developed impedance and resistance measuring techniques for membranes are described.

The simplest and best way to determine the total energy losses of a membrane under industrial conditions is the DC measuring technique, also because during electrolysis a DC current is applied.

The effects of various operating conditions and cell designs on the cell voltage are discussed in Chapter 8. It has been found that the optimum cell voltage for a finite gap membrane and a zero gap membrane cell occurs at an electrode gap of about 1.5 mm and 0.0 mm, respectively.

This difference is mainly caused by the hydrophilicity of the membrane surface.

In Chapter 9, the cell voltages are measured at the commercially available electrodes with different shapes under industrial operating conditions. Moreover, a method is proposed to determined the optimum shape of a perforated plate.

From the results obtained, it can be concluded that the contribution of gas bubbles to the electrolyte ohmic resistance under industrial conditions is negligible. The results obtained show that the cell voltage of the existing cell can be reduced significantly with the proper choice of electrode shape and membrane.

Finally, in Chapter 10 some recommendations and suggestions for further research, concerning power savings in chlor-alkali industry are given.

It can be shown that cell voltage reduction measures as proposed in this study can result in savings of approximately f 3000,000 annually at a production level of 200,000 ton Cl_2 per year.

Samenvatting

Dit proefschrift beschrijft de energie-aspecten van de chloor-alkali membraanelectrolyse met als doelstelling het energieverbruik van de bestaande elektrolysecel zonder grote investeringen te optimaliseren c.q. minimaliseren. Daartoe werden de invloeden van gasbellen en andere procesgrootheden op de celspanning onderzocht.

Bijzondere aandacht is besteed aan enerzijds het minimaliseren van de negatieve effecten en anderzijds het maximaliseren van de positieve effecten van de gasbellen op de celspanning, door gebruik te maken van een geschikt membraan en de juiste elektrodenconfiguratie.

Het gasbelgedrag werd bestudeerd m.b.v. de "high-speed" camera en de gasvolumefraktie werd met een nieuwe techniek bepaald.

Een methode werd ontwikkeld om de membraanenergieverliezen te meten. De verkregen relatie tussen de celspanning en de verschillende proces-grootheden stelde ons in staat, de juiste procesparameters te kiezen, nodig om voor een gegeven chloorproduktie het energieverbruik zo laag mogelijk te houden.

Hoofdstuk 2 geeft de geschiedenis en enkele achtergrondinformatie van het elektrolyseproces, inclusief een relevant literatuuroverzicht. De effecten van verschillende celcomponenten op de celspanning worden bediscussieerd.

In hoofdstuk 3 is de experimentele opstelling beschreven voor het bepalen van het gedrag van bellen op het elektrode-oppervlak van een chloor-ontwikkelende, transparante platina-elektrode. De geadsorbeerde bellen op deze transparante elektrode werden met een "high-speed" filmcamera opgenomen, waarna de belparameters via analyse met een "motion analyser" werden toegekend. Het is gebleken dat de belpopulatiedichtheid en de gemiddelde belstraal van de geadsorbeerde bellen toeneemt, respectieve-lijk afneemt, met toenemende stroomdichtheid. Deze resultaten konden worden verklaard met de "slow bubble growth" theorie.

Hoofdstuk 4 beschrijft de techniek voor het meten van de oververzadi-gingsconcentratie van een opgelost gas aan het oppervlak van een gas-ontwikkelende elektrode bij geforceerde convectie. Deze methode is geba-seerd op de bepaling van de "efficiency of gas bubble evolution" via de stoftransportcoëfficiënt van indicatorionen naar een gasontwikkelende elektrode. De "degree of supersaturation" van waterstof en zuurstof neemt toe met toenemende stroomdichtheid.

Bij i_o >1 kA/m^2 neemt de superverzadigingsconcentratie van zuurstof asymptotisch toe. De "degree of supersaturation" van chloorgas is onafhankelijk van de stroomdichtheid in het gemeten gebied. De superverzadigingsconcentraties van chloorgas zijn in de literatuur niet bekend en worden hier voor het eerst gepresenteerd.

De toegepaste methode ter bepaling van de belloslaatparameter en de "efficiency of gas bubble evolution" voor een chloor-, een waterstof- en een zuurstofontwikkelende micro-elektrode onder semi-industriele omstandigheden is beschreven in hoofdstuk 5. Experimenteel is gebleken dat:

- de belloslaatstraal toeneemt met toenemende stroomdichtheid (het tegengestelde is waargenomen aan een vlakke transparante platina-elektrode (zie table 3.1));
- bij gelijke, volumetrische gasbelproduktie de belloslaatstraal toeneemt in de volgorde waterstof, zuurstof en chloor.

Deze beide resultaten kunnen niet met de bestaande theorie worden verklaard. Ook is gevonden dat de "efficiency of bubble evolution" afneemt in de volgorde van waterstof, zuurstof en chloor. Dit verschijnsel is m.b.v. de driefasengrenstheorie verklaard.

Een nieuwe techniek voor de bepaling van de gasvolumefraktie en de distributie in een semi-industriële cel (50 cm hoog), bestaande uit twee vertikale, vlakke plaatelektroden, is beschreven in hoofdstuk 6. De gasvolumefrakties van chloor, waterstof en zuurstof vertonen praktisch dezelfde trend. Deze resultaten bevestigen de eerder gevonden resultaten. De hier gevonden relaties zijn alleen geldig voor vertikale, vlakke, gasontwikkelende plaatelektroden en niet voor industriële elektroden. De reden hiervan is dat industriële elektroden de gevormde gasbellen gemakkelijk naar de achterkant van de elektroden kunnen afvoeren, zodat er geen accumulatie van gasbellen tussen de elektroden ontstaat. Op deze wijze worden de negatieve effecten van de gasbellen gereduceerd.

In hoofdstuk 7 zijn de nieuwe impedantie- en weerstandsmetingen voor membranen beschreven. De eenvoudigste en beste manier om de totale energieverliezen van deze membranen onder industriele omstandigheden te bepalen is de DC techniek, mede omdat tijdens de elektrolyse een gelijkstroom wordt gebruikt.

De effecten van verschillende procesgroatheden en celconstrukties op de celspanning worden besproken in hoofdstuk 8. Het is gebleken dat de optimale celspanning voor een "finite gap" membraancel ligt bij een

elektrodenafstand van 1.5 mm en voor een "zerogap" bij 0.0 mm. Het verschil wordt veroorzaakt door het hydrofiele karakter van het membraanoppervlak.

In hoofdstuk 9 zijn de celspanningen van de elektrolysecellen met verschillende elektrodenconfiguraties onder industriele omstandigheden gemeten. Bovendien wordt een methode voorgesteld ter bepaling van de optimale geometrie van een "perforated plate" elektrode. Uit de resultaten blijkt dat de bijdrage van de gasbellen aan de ohmse weerstand van een elektrolyt onder industriële condities te verwaarlozen is. Het is gebleken dat de celspanning van een bestaande cel drastisch kan worden verlaagd als de juiste elektrodevormen en een geschikt membraan worden toegepast.

In hoofdstuk 10 worden de eindconclusies en suggesties t.b.v. het verdere onderzoek gegeven. De celspanningsreductie, die bij dit onderzoek is bereikt, komt overeen met een kostenbesparing van ongeveer Fl. 3.000.000 per jaar bij een jaarlijkse chloorproductie van 200.000 ton.

Curriculum vitae

De schrijver van dit proefschrift is geboren op 30 mei 1937 te Paramaribo. Na zijn schoolopleiding begon hij met de scheikundestudie aan de Rijksuniversiteit van Groningen. Na het afronden van de M.O.(A)- en M.O.(B)- opleiding, zette hij de studie voort aan dezelfde universiteit, waar hij in 1968 onder leiding van Prof. dr. J. Kommandeur de doctoraalstitel in de fysische chemie behaalde.

Hetzelfde jaar keerde hij terug naar Suriname, waar hij tot 1971 bij de Geologische Mijnbouwkundige Dienst als geochemicus werkzaam is geweest. In dezelfde periode was hij, als part-time docent, belast met het geven van scheikunde aan de middelbare school.

In 1971 trad hij in dienst van de Surinam Aluminum Company.

Vanaf 1976 t/m 1984 was hij hoofd van het laboratorium van Suralco en gaf hij leiding aan 81 medewerkers.

In 1984 vertrok hij opnieuw naar Nederland.

In 1985 trad hij in dienst van de Nederlandse organisatie voor wetenschappelijk onderzoek als wetenschappelijk onderzoekmedewerker, verbonden aan de Technische Universiteit Eindhoven, op de afdeling Elektrochemie, onder leiding van Prof. E. Barendrecht.

In hetzelfde jaar begon hij met het promotie-onderzoek, dat tenslotte tot dit proefschrift heeft geleid.

In 1988 behaalde hij het diploma Post HBO milieukunde.

De schrijver is getrouwd met Petra Schaminée. Uit dit huwelijk zijn vier kinderen geboren t.w.: Marco (arts), André (Ir. in de werktuigbouwkunde), Carmen (Ir. in de tropische landbouw en veeteelt) en als laatste David (VWO-er, atheneum 5B).

Stellingen

1　De bewering, dat de anodepotentiaal bij een chloor-alkali elektrolyse dezelfde blijft, ongeacht de vorm van de anode, is onjuist.

　　M. Seko, A. Yomiyama, S. Ogawa and H. One, Development of Asahi Chemical Chlor-alkali Technology, Society of Chemical Industry, Electrochemistry Technology Group, International Chlorine Symposium, London, 2-4. 6. (1982) 25.

2　De aanname dat in elektrolysecellen met gasontwikkelende elektroden de celspanning toeneemt met toenemende hoogte van de elektroden is aanvechtbaar.

　　G. Kreysa and M. Kuhn, J. Appl. Electrochem. $\underline{15}$ (1985) 517.
　　Hoofdstuk 6 van dit proefschrift.

3　Bij waterelektrolyse is een slipratio, van van boven naderend tot één, hoogst onwaarschijnlijk.

　　J.E. Funk and J.F. Thorpe. J. Electrochem. Soc. $\underline{116}$ (1969) 48.

4　Bij het vervangen van vlakke plaatelektroden van een elektrolysecel door lamelelektroden kunnen praktisch alle negatieve en positieve effecten van gasbellen worden geelimineerd, respectievelijk worden benut t.b.v. de optimalisatie van het energieverbruik.

　　Hoofdstuk 8 en 9 van dit proefschrift.

5　Het rendement van de bestaande chloor-alkali membraancellen kan op een economische wijze worden opgevoerd door de bestaande elektroden te vervangen door lamelelektroden.

　　Hoofdstuk 10 van dit proefschrift.

6　De superverzadigingsconcentratie van een opgelost gas aan het oppervlak van een gasontwikkelende elektrode kan niet uit de belgroeiparameters berekend worden.

H. Vogt, Fortschr. Verfahrungstechnik 20 (1982) 369.

7   De klassieke economische theorie is niet geschikt om milieuproblemen
     op te lossen.

     Allen V. Kneese and Ralph C. d'Arge, Pervasive external costs and
     the response of society.
     In: The analysis and evaluation of public expenditure: the PPB –
     system. A compendum of papers submitted to the Subcommittee on
     Economy in Government of the Joint Economic Committee, 91 Cong. 1
     session 1969.

     A. Heertje – Voor niets gaat de zon op – ESB (1989) 428

8   Het storten van chemisch afval in de derde wereldlanden wordt door
     de regeringen van de rijke landen oogluikend toegelaten. Deze
     houding moet als immoreel worden gekwalificeerd.

     Meerjarig   intensiveringsprogramma   (MIP)   handhaving   wetgeving
     chemisch afval. Publicatiereeks milieubeheer nr. 85, Ministerie
     V.R.O.M., december 1984.

9   Het aantrekken en opleiden van wetenschappelijk, technisch en
     management kader vormen de sleutel voor de toekomstige positieve
     ontwikkeling van Suriname.

10   De toekomst van Suriname zal in sterke mate worden bepaald door
     verhoging van het wetenschappelijk en technologisch peil van de
     Technische Universiteit in Paramaribo.

11   De relatieve hoge levensstandaard in de geindustrialiseerde landen
     kan alleen worden gehandhaafd, als de derde wereldlanden het hun
     toekomende aandeel in fossiele brandstoffen niet opeisen.

     A. Weinberg; The maturity and future of nuclear energy. American
     Scientist 64 (1976) 16.

     Eindhoven, 27 oktober 1989   Joek Mien Chin Kwie Joe